Overview of Open-Loop Frequency Estimation Techniques for Grid Synchronization of Single-Phase Power Converters

Hachemi Rahmani, Boulouma Sabri, and Mourad Haddadi

Abstract−Open-loop synchronization techniques allow to overcome the stability issues to which closed-loop techniques are subject. Most open-loop techniques differ in their Quadratic Signal Generator and their frequency estimation method. In this paper, an overview of the main frequency estimation methods for single-phase power systems is presented. A description of each technique with their structure for numerical implementation is carried out. A comparative study of those frequency estimation methods is performed according to three test scenarios in order to evaluate the robustness of each method. Recommendations for the selection of the technique is given according to the simulation results.

***Keywords*− Open-loop grid synchronization, Frequency estimation, grid-connected power inverter.**

I. INTRODUCTION

The current concept of centralized and unidirectional energy flow utility grids is unsustainable for economic, security, reliability, and ecological reasons [1]. The integration of decentralized energy resources addresses these issues, particularly with renewable energy sources like photovoltaic and wind. However, to ensure good energy quality, these resources must inject current according to established standards. Ideally, the grid voltage waveform is a pure sine wave with fixed amplitude and frequency at nominal values. In reality, they are subject to fluctuations due to grid conditions. For instance, voltage sags along with phase jumps can occur during the startup of powerful motors [2], while frequency shifts happen during load commutations [3]. The importance of fast, robust, and precise estimation of grid parameters cannot be overstated for several reasons. It includes ensuring the stability and reliability of the power grid, maintaining power quality, facilitating the grid integration of renewable energy resources, and reducing disturbances. Open loop (OL) synchronization techniques were the first ones to appear in literature with the introduction of the Zero Crossing Detection (ZCD) technique. Unfortunately, the poor performances of ZCD in case of weak grid with many power quality issues, open-loop techniques have been replaced by closed-loop (CL) ones [4]. However, with the constantly increasing integration of grid connected power converters, tighter restrictions concerning injected current have been imposed. Although CL techniques performances are somehow satisfying, they have a dynamic behavior limited by their stability conditions. OL techniques do not have this problem, as they are unconditionally stable. In recent years, modern OL synchronization techniques emerged, whose performance can compete those of closed-loop ones [5].

Manuscript received January 2, 2023; revised June 27, 2024.

H. Rahmani and B. Sabri are with UDES/EPST CDER, Tipaza, ALGERIA.
(e-mail: rahmani.hachemi@udes.dz, boulouma.sabri@udes.dz).

M. Haddadi is with Ecole Nationale Polytechnique, Algiers, ALGERIA. (e-mail: mourad.haddadi@g.enp.edu.dz).

Digital Object Identifier (DOI): 10.53907/enpesj.v4i1.179

For single-phase power systems, OL amplitude and phase estimations consist first on generating in-phase and quadratic signals from the grid voltage using a Quadratic Signal Generator (QSG). Considering the grid voltage v given by:

$$v(t) = V_m \cos(\theta(t)) = V_m \cos(2\pi f t + \phi) \tag{1}$$

Were Vm is the amplitude, θ is the phase angle, f is the frequency and ϕ is the initial phase angle.

In-phase signal v_α and quadratic signal v_β are expressed by:

$$\begin{cases} v_\alpha(t) = V_m \cos(\theta(t)) \\ v_\beta(t) = V_m \sin(\theta(t)) \end{cases} \tag{2}$$

Given this two signals, amplitude V_m and phase angle θ are obtained at instant t by:

$$V_m = \sqrt{v_\alpha^2 + v_\beta^2} \tag{3}$$

$$\theta = \tan^{-1}\left(\frac{v_\beta}{v_\alpha}\right) \tag{4}$$

Although OL amplitude and phase estimations in grid synchronization techniques are almost the same, there are various methods to estimate the grid frequency.

This paper presents an overview of open-loop frequency estimation techniques for grid-connected power converters proposed in the literature. A description of those techniques is explained and simulated according to three tests scenarios. A comparison of those techniques is performed to emphasize advantages and disadvantages of each technique.

II. SYNCHRONIZATION BY ZERO-CROSSING DETECTION.

A simple method to estimate grid frequency and phase angle is first, to detect instants where the AC grid voltage crosses zero, then evaluate the duration between two instants to measure the grid period. Phase angle is obtained by integrating frequency. In practice, ZCD can be realized by an electronics board, like a half-wave rectifier with a voltage comparator that gives a square signal with a 50% duty cycle, toward a microcontroller. The rising and falling edges of this signal call a microcontroller interrupt subroutine that measure half a period of the input signal and calculate its frequency [6]. ZCD can also be achieved numerically, by observing sign changes of the input signal samples [7].

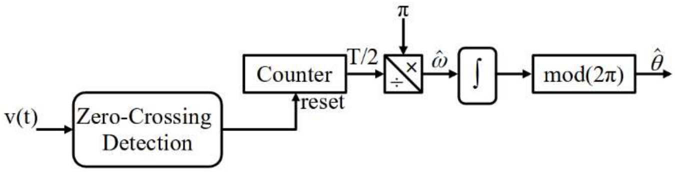

Fig. 1: Frequency and phase angle estimation using ZCD.

This method presents several disadvantages. When the ZCD is performed numerically, it requires a high sampling frequency in order to minimize estimated frequency errors. Moreover, this technique is too sensitive to grid disturbances. For example, multiple zero-crossing can be detected if the grid voltage is polluted by harmonics or frequency estimation can be incorrect if the signal input signal present a DC offset. To solve this issue, a sharp filter can be used to remove voltage distortions. The problem is that the sharper the filter, the slower is the dynamic response.

III. MODERN OPEN-LOOP FREQUENCY ESTIMATION TECHNIQUES

There are several OL frequency estimation techniques in the literature. Some of them require QSG, some do not. All those techniques can estimate input signal frequency using few samples. They can be classified by standard methods, consecutive samples methods, and Teager Energy Operator method.

A. Standard Methods

One of the most intuitive method to estimate the grid frequency is to differentiate its phase angle, using (4) [8]:

$$\hat{\omega} = \frac{d\hat{\theta}}{dt} = \frac{\dot{\hat{v}}_\beta \hat{v}_\alpha - \dot{\hat{v}}_\alpha \hat{v}_\beta}{\hat{v}_\alpha^2 + \hat{v}_\beta^2} \quad (5)$$

The hat over a variable mean its estimated value and the dot over a variable mean its derivative.

In discrete-time, this give the following differences equation:

$$\hat{\omega}_{std} = \frac{1}{T_s} \frac{\hat{v}_\alpha(n-1)\hat{v}_\beta(n) - \hat{v}_\beta(n-1)\hat{v}_\alpha(n)}{\hat{v}_\alpha^2(n) + \hat{v}_\beta^2(n)} \quad (6)$$

Where T_s is the sampling period. This method presents a steady-state error that increase when the switching frequency decrease [9]. To correct this error, an enhanced version that introduce inverse sinus function, was developed [10].

$$\hat{\omega}_{estd} = \frac{1}{T_s} \sin^{-1}\left(\frac{\hat{v}_\alpha(n-1)\hat{v}_\beta(n) - \hat{v}_\beta(n-1)\hat{v}_\alpha(n)}{\hat{v}_\alpha^2(n) + \hat{v}_\beta^2(n)} \right) \quad (7)$$

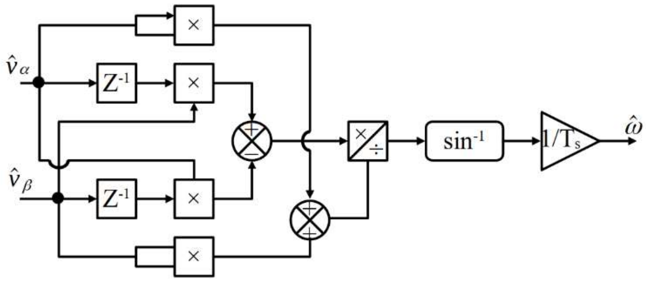

Fig. 2: Structure of the enhanced standard method.

B. Consecutive samples methods

Also called equidistant samples methods, they require 2, 3, or 4 input signal samples to estimate its frequency. They are noticed respectively by 2CS, 3CS and 4CS.

The 2CS method require a QSG to estimate the frequency using the following formula:

$$\hat{\omega}_{2CS} = \frac{1}{T_s} \cos^{-1}\left(\frac{\hat{v}_\alpha(n)\hat{v}_\alpha(n-1) + \hat{v}_\beta(n)\hat{v}_\beta(n-1)}{\hat{v}_\alpha^2(n) + \hat{v}_\beta^2(n)} \right) \quad (8)$$

One disadvantage of relying on a QSG is that the estimated frequency is subject to errors when v_α and v_β are not perfectly in quadrature, which can happen for example when the QSG is sensitive to frequency deviation or in case of unbalanced three-phase system.

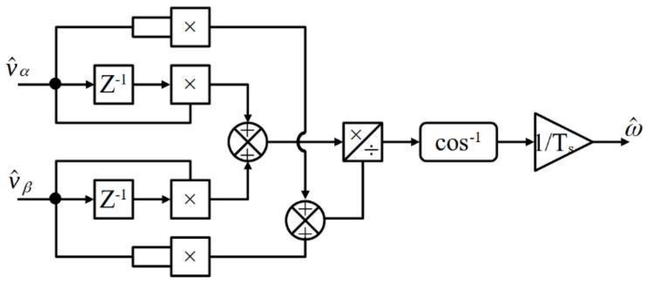

Fig. 3: Structure of the 2CS method

The standard versions of the 3CS [11] and the 4CS [12] methods do not require QSG. Frequency is respectively estimated using the following equations:

$$\hat{\omega}_{3CS} = \frac{1}{T_s} \cos^{-1}\left(\frac{v(n) + v(n-2)}{2v(n-1)} \right) \quad (9)$$

$$\hat{\omega}_{4CS} = \frac{1}{T_s} \cos^{-1}\left(\frac{(v(n) - v(n-1)) + (v(n-2) - v(n-3))}{2(v(n-1) - v(n-2))} \right) \quad (10)$$

The major disadvantage of the 3CS and 4CS methods is their ill-conditioning issues when the denominator is equal or very close to zero. To avoid this situation, it is more suitable to base on two signal with different phases, as can provide a QSG, but not necessarily orthogonal.

This lead to enhanced version of 3CS and 4CS (E3CS and E4CS), described by the following equations:

$$\hat{\omega}_{E3CS} = \frac{1}{T_s} \cos^{-1}\left(\frac{\hat{v}_\alpha(n-1)(\hat{v}_\alpha(n) + \hat{v}_\alpha(n-2)) + \hat{v}_\beta(n-1)(\hat{v}_\beta(n) + \hat{v}_\beta(n-2))}{2(\hat{v}_\alpha^2(n-1) + \hat{v}_\beta^2(n-1))} \right) \quad (11)$$

$$\hat{\omega}_{E4CS} = \frac{1}{T_s}\cos^{-1}\left(\frac{(M_{1\alpha}+M_{1\beta})+(M_{2\alpha}+M_{2\beta})}{2(M_{2\alpha}+M_{2\beta})}\right) \quad (12)$$

With

$$\begin{cases} M_{1x} = v_x(n)v_x(n-1) - v_x(n-1)v_x(n-3) \\ M_{2x} = v_x^2(n-1) - v_x(n-1)v_x(n-2) \end{cases} \quad (13)$$

Where x can be either α or β.

4CS and E4CS methods are the only ones to be immune to the presence of DC offset in the input signal [12], [13].

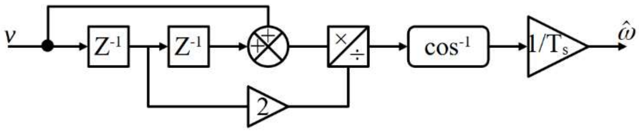

Fig. 4: Structure of the 3CS method

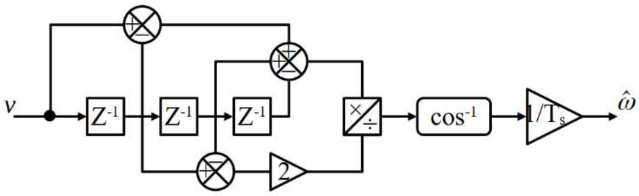

Fig. 5: Structure of the 4CS method

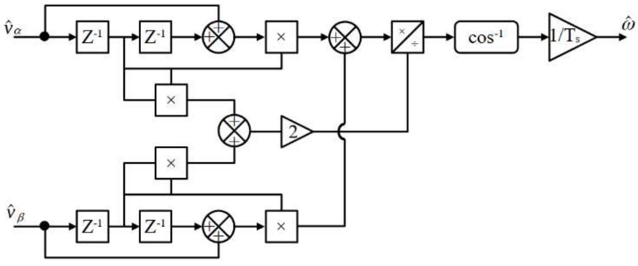

Fig. 6: Structure of the E3CS method

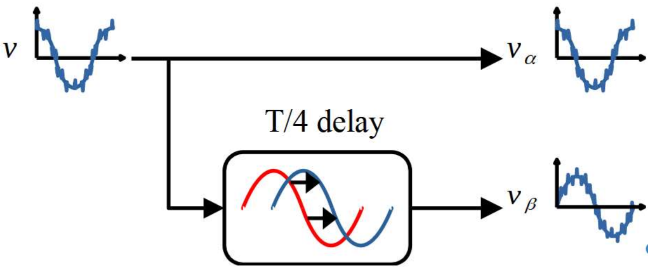

Fig. 7: Structure of the TD-QSG

C. Teager Energy Operator

The Teager Energy Operator (TEO) was first described in [14]. It can achieve amplitude and frequency estimation of an input signal using three samples without using QSG or causing ill-conditioning.

The Energy operator Ψ applied to a random signal $x(t)$ is given by the following equation[15]:

$$\psi[x(t)] = \dot{x}(t) - x(t)\ddot{x}(t) \quad (14)$$

Applied to grid voltage $v(t)$ described by (1) gives:

$$\psi[v(t)] = V_m^2\omega^2 \quad (15)$$

Moreover, if (14) is applied on the derivative of $v(t)$, it gives :

$$\psi[\dot{v}(t)] = V_m^2\omega^4 \quad (16)$$

Combining (15) with (16), amplitude V_m and angular frequency ω are obtained by the following formulas:

$$\begin{cases} V_m = \dfrac{\psi[v(t)]}{\sqrt{\psi[\dot{v}(t)]}} \\ \omega = \sqrt{\dfrac{\psi[\dot{v}(t)]}{\psi[v(t)]}} \end{cases} \quad (17)$$

In discrete time (14) becomes:

$$\psi[x(n)] = \frac{(x^2(n) - x(n+1)x(n-1))}{T_s^2} \quad (18)$$

The estimated amplitude and frequency are then obtained by:

$$\begin{cases} \hat{V}_m = \dfrac{2\psi[v(n)]}{\sqrt{\psi[v(n+1)-v(n-1)]}} \\ \hat{\omega} = \sqrt{\dfrac{\psi[v(n+1)-v(n-1)]}{4\psi[v(n)]}} \end{cases} \quad (19)$$

The major concern of the TEO is its high sensitivity to noises. Indeed, the use of derivative increases input signal noises and greatly corrupt the frequency estimation. For this reason, some works associate this method with a very sharp filter like the filter based on Recursive Discrete Fourier Transform (RDFT) and inverse RDFT (IRDFT) [16]–[19] . In practice, using a RDFT-IRDFT filter brings other issues like rounding errors and instability especially when using its frequency adaptive version [20]–[23].

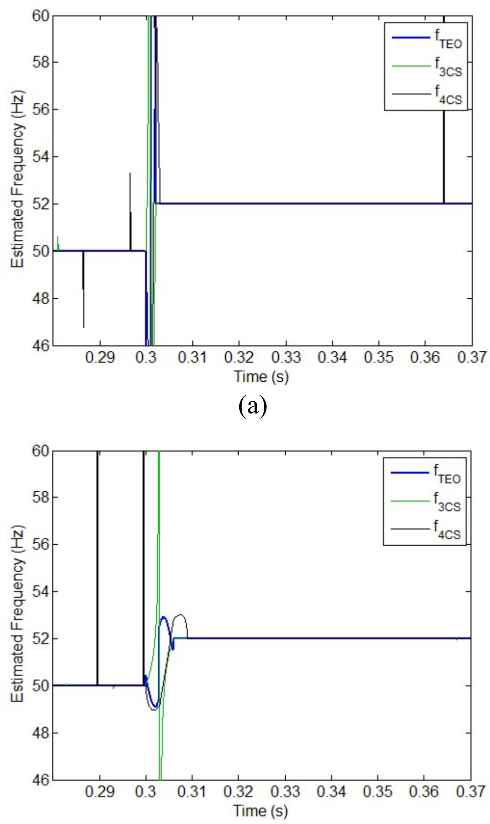

(a)

(b)

Fig. 8: Estimated Frequency of QSG-less methods for test 1.
(a) N=10, (b) N=30

D. *Adjusting noise immunity*

It can be noticed that the duration between two samples is not necessarily equal to one sampling period but it can also be a multiple of the sampling period to give to the method a better immunity against signal noises. For instance, giving N as the distance between two samples (such that the duration between two samples is NT_s), equation (9) can be generalized to the following formula:

$$\hat{\omega}_{3CS} = \frac{1}{NT_s}\cos^{-1}\left(\frac{v(n)+v(n-2N)}{2v(n-N)}\right) \qquad (20)$$

Increasing N provides a better noises immunity to the method, but slows its dynamic response down. Selecting N is a compromise between speed and robustness of the used method.

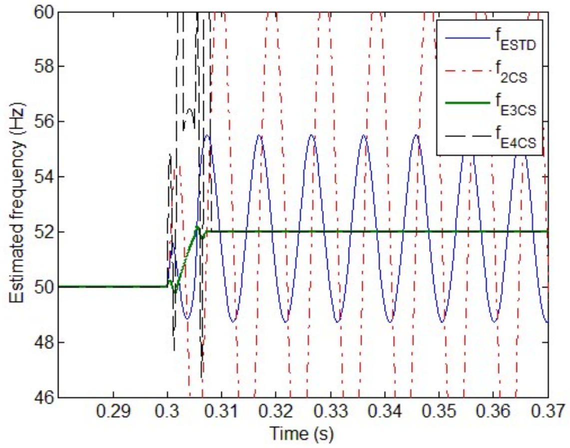

(a)

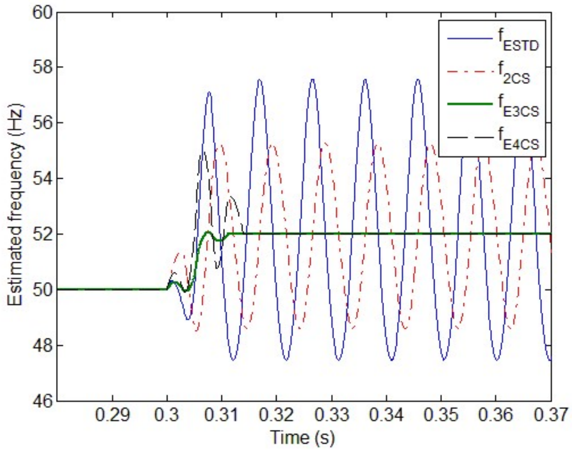

(b)

Fig. 9: Estimated Frequency of QSG-based methods for test 1.
(a) N=10, (b) N=30

E. *Comparison of the frequency estimation techniques*

Modern frequency estimation techniques mentioned above can be separated into two groups: those who do not require a QSG (3CS, 4CS and TEO) and those who are based on QSG (ESTD, 2CS, E3CS and E4CS).

To compare the performances of those methods, a series of three tests is applied in simulation on each group. For all the three tests, the grid voltage is a unitary sine wave signal which shows a frequency jump from 50 Hz to 52 Hz at instant $t = 0.3$ s. For test 1, the input signal does not present any distortion. For test 2, the input signal is corrupted by a very light white noise, such that the signal-to-noise ratio reach 57 dB. For test 3, a third order harmonic of magnitude equal to 0.5% of the fundamental is added to the input signal. The sampling frequency is equal to 10 kHz.

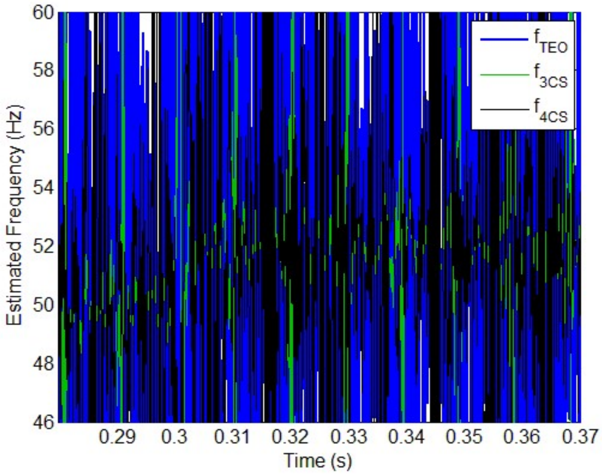

(a)

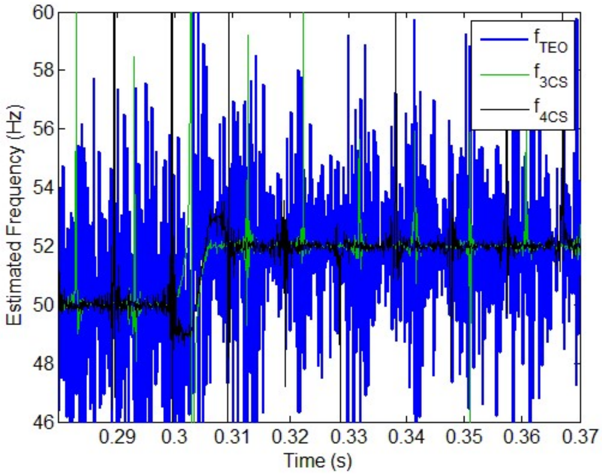

(b)

Fig. 10: Estimated Frequency of QSG-less methods for test 2.
(a) N=10, (b) N=30

The QSG used in this simulation is a frequency non-adaptive, transfer delay-based QSG (TD-QSG). This QSG relies on time-delaying the input signal using a buffer to create a quadrature component [4]. This way, neither the input signal nor the quadrature signal is filtered. Tests are performed with two distances N between samples. First, N equal 10, then N equal 30.

Fig. 7 shows simulation results of 3CS, 4CS, and TEO methods for test 1. It can be seen that the TEO method stands out of the other methods by the absence of notches due to ill-conditioning.

Fig. 8 shows simulation results of ESTD, 2CS, E3CS and E4CS methods for test 1. It appears that ESTD and 2CS methods present an oscillatory behavior after the frequency jump. This is due to the non-orthogonality between v_α and v_β because the used TD-QSG is not frequency adaptive. Results of E3CS and E4CS methods are the same in steady-state, but E4CS method shows greater disturbances in transient operations. Those two methods are not sensitive to non-orthogonality between v_α and v_β.

Results of test 2 show that increasing the sample distance enhances significantly the robustness of the frequency estimation techniques against noises. For the QSG-less techniques, the TEO exhibits the weakest robustness against noises (Fig. 10). For the QSG-based techniques, results show that the E4CS is the most sensitive technique against noises, and the E3CS is the most robust one (Fig. 11).

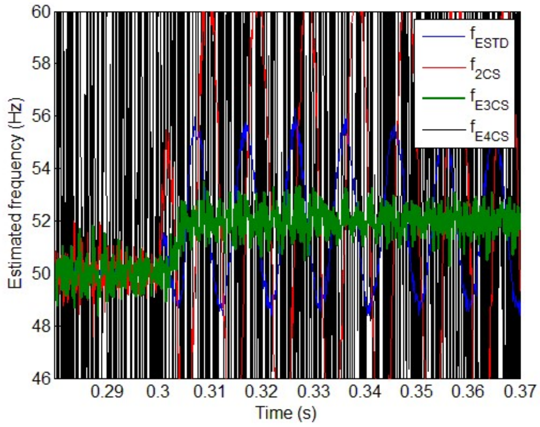

(a)

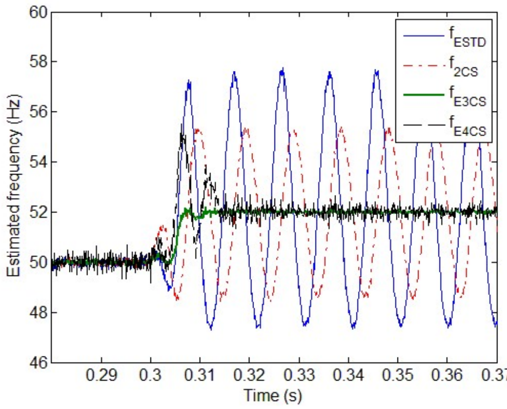

(b)

Fig. 11: Estimated Frequency of QSG-based methods for test 2. (a) N=10, (b) N=30

Results of test 3 (Fig. 12 and 13) shows that the TEO requires that the input signal has to be considerably filtered in order to reduce the estimated frequency distortions properly. Among all those techniques, the E3CS proves to be the most robust against low-order harmonics.

Tables 1 and 2 summarize features of the tested techniques. One can conclude that, according to its superior robustness, the E3CS method is the most suitable open-loop frequency estimation technique for grid synchronization.

Table. II
COMPARISON OF QSG-BASED FREQUENCY ESTIMATION TECHNIQUES

Technique	Sensitivity to QSG unbalances	Robustness against noises	Robustness against low-order harmonics
ESTD	Yes	Moderate	Good
2CS	Yes	Moderate	Moderate
E3CS	No	Good	Good
E4CS	No	Moderate	Weak

Table. I
COMPARISON OF QSG-LESS FREQUENCY ESTIMATION TECHNIQUES

Technique	Ill-conditioning issue	Robustness against noises	Robustness against low-order harmonics
TEO	No	Very weak	Moderate
3CS	Yes	Good	Good
4CS	Yes	Moderate	Moderate

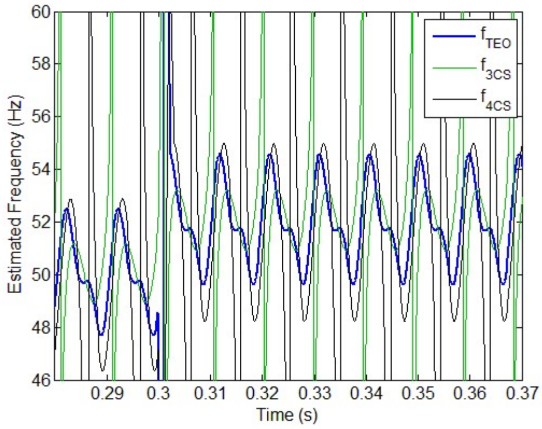

(a)

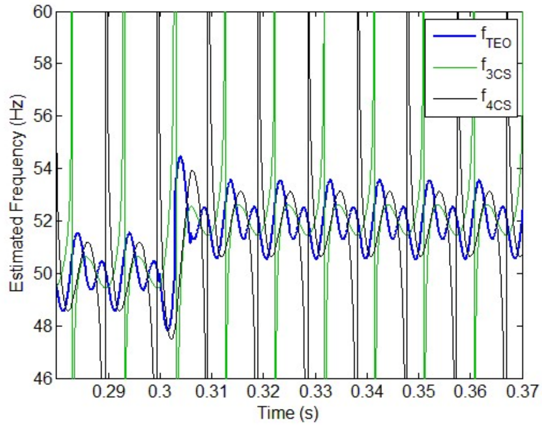

(b)

Fig. 12: Estimated Frequency of QSG-less methods for test 3. (a) N=10, (b) N=30

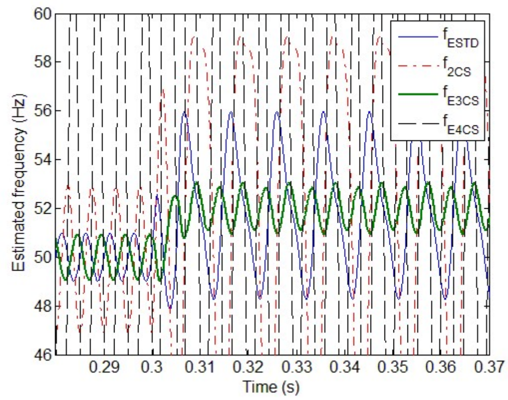

(a)

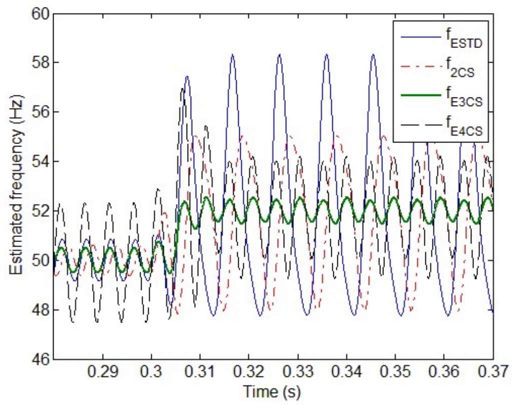

(b)

Fig. 13: Estimated Frequency of QSG-based methods for test 3. (a) N=10, (b) N=30

IV. CONCLUSION

Open-loop synchronization techniques allow to overcome the Open-loop synchronization techniques overcome the stability issues inherent in closed-loop techniques. For single-phase power systems, all modern open-loop synchronization techniques, except the TEO, require a QSG to estimate the grid voltage amplitude and phase angle. However, this is not always the case for frequency estimation.

Most open-loop techniques differ in their QSG and frequency estimation methods. In this paper, an overview of the main frequency estimation methods was presented, along with a description of each technique and its structure for numerical implementation. A comparative study of these frequency estimation methods was conducted to test the robustness of each method. The results show that the E3CS method offers the best performance in terms of robustness against noise and low-order harmonics. Therefore, this method is recommended for single-phase power system applications.

REFERENCES

[1] J. Martin, "An_introduction_to_distributed_generation," 2009, [Online]. Available:http://vernimmen.com/ftp/An_introduction_to_distributed_generation.pdf

[2] A. K. Goswami, C. P. Gupta, and G. K. Singh, "An analytical approach for stochastic assessment of voltage sags in distribution systems," IEEE Reg. 10 Annu. Int. Conf. Proceedings/TENCON, no. December, 2008, doi: 10.1109/TENCON.2008.4766390.

[3] IEEE Std, "IEEE Recommended Practice for Monitoring Electric Power Quality," 2019. [Online]. Available: http://ieeexplore.ieee.org/xpl/freeabs_all.jsp?arnumber=5154067

[4] M. Ciobotaru, "Reliable Grid Condition Detection and Control of Single-Phase Distributed Power Generation Systems," Aalborg Universitet, 2009.

[5] S. Golestan, J. M. Guerrero, and J. C. Vasquez, "An Open-Loop Grid Synchronization Approach for Single-Phase Applications," IEEE Trans. Power Electron., vol. 33, no. 7, pp. 5548–5555, Jul. 2018, doi: 10.1109/TPEL.2017.2782622.

[6] H. Rahmani, "Utilisation du dsPIC dans la mesure de paramètres électriques," École Nationale Polytechnique d'Alger, 2011.

[7] F. Mur, V. Cárdenas, J. Vaquero, and S. Martínez, "Phase synchronization and measurement digital systems of AC mains for power converters," Int. Power Electron. Congr. - CIEP, vol. 1998, pp. 188–194, 1998, doi: 10.1109/ciep.1998.750682.

[8] F. D. Freijedo, J. Doval-Gandoy, O. López, E. Acha, and S. Member, "A Generic Open-Loop Algorithm for Three-Phase Grid Voltage/Current Synchronization With Particular Reference to Phase, Frequency, and Amplitude Estimation," IEEE Trans. POWER Electron., vol. 24, no. 1, 2009, doi: 10.1109/TPEL.2008.2005580.

[9] S. Golestan, A. Vidal, A. G. Yepes, J. M. Guerrero, J. C. Vasquez, and J. Doval-Gandoy, "A True Open-Loop Synchronization Technique," IEEE Trans. Ind. Informatics, vol. 12, no. 3, pp. 1093–1103, 2016, doi: 10.1109/TII.2016.2550017.

[10] S. Golestan, J. M. Guerrero, Y. Al-Turki, A. M. Abusorrah, and J. C. Vasquez, "Open-Loop Synchronization Systems for Grid-Tied Power Converters: Literature Overview, Design Considerations, Advantages, and Disadvantages," IEEE Ind. Electron. Mag., 2021, doi: 10.1109/MIE.2021.3126255.

[11] A. López, J. C. Montaño, M. Castilla, J. Gutiérrez, M. D. Borrás, and J. C. Bravo, "Power system frequency measurement under nonstationary situations," IEEE Trans. Power Deliv., vol. 23, no. 2, pp. 562–567, Apr. 2008, doi: 10.1109/TPWRD.2007.916018.

[12] D. N. Vizireanu, "A simple and precise real-time four point single sinusoid signals instantaneous frequency estimation method for portable DSP based instrumentation," Measurement, vol. 44, no. 2, pp. 500–502, Feb. 2011, doi: 10.1016/J.MEASUREMENT.2010.11.001.

[13] A. K. Verma, R. K. Jarial, P. Roncero-Sanchez, and M. R. Ungarala, "Improved Fundamental Frequency Estimator for Three-Phase Application," IEEE Trans. Ind. Electron., vol. 68, no. 9, pp. 8992–8998, Sep. 2021, doi: 10.1109/TIE.2020.3018063.

[14] J. F. Kaiser, "On a simple algorithm to calculate the 'energy' of a signal," ICASSP, IEEE Int. Conf. Acoust. Speech Signal Process. - Proc., vol. 1, no. 10, pp. 381–384, 1990, doi: 10.1109/icassp.1990.115702.

[15] D. A. Kaiser and J. F. Kaiser, "Estimation of power systems amplitudes, frequencies, and phase characteristics using Energy Operators," 2012 IEEE Energy Convers. Congr. Expo. ECCE 2012, pp. 930–937, 2012, doi: 10.1109/ECCE.2012.6342719.

[16] C. J. Nwobu, A. M. Nakiganda, and L. Zhang, "Grid Voltage Synchronization for Unbalanced Voltages Using the Energy Operator," IEEE J. Emerg. Sel. Top. Power Electron., vol. 5, no. 3, pp. 1415–1424, 2017, doi: 10.1109/JESTPE.2017.2704022.

[17] S. Reza, S. Member, M. Ciobotaru, V. G. Agelidis, and S. Member, "A Recursive DFT Based Technique for Accurate Estimation of Grid Voltage Frequency," IECON 2013 - 39th Annu. Conf. IEEE Ind. Electron. Soc., pp. 6420–6425, 2013, doi: 10.1109/IECON.2013.6700193.

[18] S. Reza et al., "Single-Phase Grid Voltage Frequency Estimation Using Teager Energy Operator-Based Technique," IEEE J. Emerg. Sel. Top. Power Electron., vol. 3, no. 4, pp. 1218–1227, 2015, doi: 10.1109/JESTPE.2015.2405094.

[19] A. Sahoo, J. Ravishankar, and C. Jones, "Phase-Locked Loop Independent Second-Order Generalized Integrator for Single-Phase Grid Synchronization," IEEE Trans. Instrum. Meas., vol. 70, 2021, doi: 10.1109/TIM.2021.3104406.

[20] P. Gawhade and A. Ojha, "Recent advances in synchronization techniques for grid-tied PV system: A review," Energy Reports, vol. 7, pp. 6581–6599, Nov. 2021, doi: 10.1016/j.egyr.2021.09.006.

[21] H. A. Darwish and M. Fikri, "Practical considerations for recursive DFT implementation in numerical relays," Proc. IEEE Power Eng. Soc. Transm. Distrib. Conf., vol. 22, no. 1, pp. 880–887, 2006, doi: 10.1109/TDC.2006.1668614.

[22] F. A. S. Neves, H. E. P. De Souza, F. Bradaschia, M. C. Cavalcanti, M. Rizo, and F. J. Rodríguez, "A space-vector discrete fourier transform for unbalanced and distorted three-phase signals," IEEE Trans. Ind. Electron., vol. 57, no. 8, pp. 2858–2867, 2010, doi: 10.1109/TIE.2009.2036646.

[23] S. Golestan et al., "Single-Phase PLLs: A Review of Recent Advances," IEEE Trans. Power Electron., vol. 32, no. 12, pp. 9013–9030, Dec. 2017, doi: 10.1109/TPEL.2017.2653861.

Hachemi Rahmani received his engineering degree in electronics from the University of Saad Dahlab in Blida in 2006, and then obtained his Magister degree from the Ecole Nationale Polytechnique in 2011. He joined the Solar Equipment Development Unit in 2012 as a Research Associate. His research area includes the control of grid-connected photovoltaic systems as well as data acquisition and graphical interfacing in distributed systems.

Boulouma Sabri was born in 1984 in Skikda, Algeria. He obtained the first cycle university degree from the National Preparatory School for Engineering Studies in Rouiba, Algeria in 2005, the state engineering degree in electrical engineering with a control option from the Institute of Electrical and Electronic Engineering of Boumerdes (formerly INELEC) in 2009. He obtained a Magister in electronics with a control option from the University of Jijel in 2012, a Magister in Infotronics from the University of Boumerdes in 2015, and a Ph.D. in electronics from the University of Jijel in 2017. He is a permanent researcher at the Solar Equipment Development Unit in Bou-Ismail. His areas of expertise include nonlinear and intelligent control, diagnosis and supervision of hybrid systems, signal processing, and data analysis.

Mourad Haddadi received a Ph.D. in electronics from the Ecole Nationale Polytechnique in Algiers, Algeria. He is currently a Senior Researcher and Head of the Electronics Department at the Ecole Nationale Polytechnique. He was engaged in renewable energies and solar electricity for more than 30 years. His research and development tasks mainly relate to photovoltaic applications, solar energy, photovoltaic systems and devices, and the most promising applications in renewable energies. Heist an expert and reviewer in many journals. He is the author or co-author of more than 60 publications.

Human Visual System applied to Facial Recognition

Fatima Zohra Allam, Latifa Hamami-Mitiche, and Hicham Bousbia-Salah

Abstract − Research in the field of biometrics is constantly expanding. Numerous studies have been carried out to develop different techniques with the aim of ensuring reliable and efficient recognition systems. Of our five senses, vision takes up the most of the neurons in our brain. This makes the visual approach challenging. This paper proposes to develop a new facial recognition technique based on the concept of Human Visual System in order to simulate or imitate human perception. Our approach exploits the behavior of the Human Visual System in biometric systems to improve individual recognition. It focuses on Perceptual Channel Decomposition in order to generate images, confined around a certain frequency range, perfectly uncorrelated. For the extraction of characteristic vectors, our technique uses the Principal Component Analysis. The principle of the visual approach consists of exploiting one or more characteristics of the peripheral parts of the Human Visual System. These characteristics can integrate the sensitivity of the Human Visual System to spatial frequencies, its sensitivity to local contrast. The Principal Component Analysis uses a set of seventeen channels, each adjusted to a band of given radial frequencies and orientation. The seventeen output images contain the same spatial information but are perfectly uncorrelated from a spectral point of view. In the implementation phase, we limited ourselves to explore this technique by using only four frequency rings. The results obtained are conclusive and satisfactory.

***Keywords* − Human Visual System, Perceptual Channel Decomposition, Principal Component Analysis.**

I. Introduction

With the multiplication of applications in the biometric field, person recognition has attracted great attention in the scientific community, to the point that it is difficult to draw up an exhaustive assessment of all the work in this field. This is explained, on the one hand, by the enormous application interest, among others, in the field of security, video surveillance and general public multimedia applications, on the other hand, by the challenge that this represents for artificial vision algorithms. Biometrics brings together all computer techniques aimed at irrefutably determining the identity of a person based on their physical and/or behavioral characteristics, without having to use a card or password. Over the past decades, researchers have focused on developing automatic authentication systems capable of combating fraud to ensure security in different areas ranging from the most emblematic, such as crossing international borders, to the less burdensome, such as access to personal information. To meet these needs, biometrics, which is experiencing rapid development, appears to be a practical and effective solution. It makes it possible to measure the characteristics of people in order to characterize and authenticate them. It has established itself as a preferred technology in the field of recognition. This enthusiasm leads to the development of very varied biometric methods: from the most classic, such as facial recognition, the study of fingerprints, to the most exotic, such as gait recognition or recognition of the shape of the ears. Today, biometrics is establishing itself in the eyes of States as a security solution par excellence. Facial recognition is one of the most used biometric techniques. We notice that in daily life each of us identifies, throughout the day, different faces. So, when we meet a person, our brain will search our memory and check whether that person is listed or not. The facial modality is non-intrusive because it does not affect the privacy of the individual. It constitutes one of the most natural ways to recognize a person, unlike the iris which is certainly more intrusive. In this article, we propose an innovative alternative to create a biometric recognition system, different from those already developed in the literature. Traditional methods are based on the use of algorithms dedicated to the extraction of relevant characteristics such as the Gabor Filter, the Local Binary Pattern, and Zernike Moments. Our approach exploits the behavior of the Human Visual System. We are interested in processing spectral information rather than using the gray levels of the acquired image. This is a more elaborate model on image perception exploiting the behavior of the Human Visual System (HVS). The SVH coherently models key functions of perception such as Perceptual Channel Decomposition (PCD), Contrast Sensitivity Functions (CSF), etc. In our work, we favor approaches that seek to "simulate" human perception. Instead of using the gray levels of the facial image, these approaches exploit, through a decomposition into visual frequency sub-bands, characteristics similar to those used by the Human Visual System, such as Local Band-Limited Contrast (LBLC). Our article is structured as follows: In the second section, we introduce some common concepts about biometrics and biometric systems. We also present a state of the art on facial recognition. In the third section, we present another alternative to realize the biometric system for person recognition based on the processing of spectral information. This is a more elaborate model on image perception exploiting the behavior of the Human Visual System (HVS). The SVH coherently models key functions of perception such as Perceptual Channel Decomposition (PCD), Contrast Sensitivity Functions (CSF), etc. In this chapter, we favor approaches that seek to "simulate" human perception.

Manuscript received October 25, 2023; revised June 27, 2024.

F. Z. Allam, L. Hamami-Mitiche, and H. Bousbia-Salah are with Electronics Department, Ecole Nationale Polytechnique, Algiers, ALGERIA. (e-mail: mourad.haddadi@g.enp.edu.dz).

Digital Object Identifier (DOI): 10.53907/enpesj.v4i1.247

Instead of using the gray levels of the facial image, these approaches exploit, through a decomposition into visual frequency sub-bands, characteristics similar to those used by the Human Visual System, such as Local Band-Limited Contrast (LBLC). In the fourth section, we explain the steps we followed for the implementation of the facial recognition system. The fifth section indicates the results obtained.

II. Biometric Concepts

In this section, we present some common notions about biometrics:

1. Biometric Processes

Any biometric system operates in enrollment, verification and identification mode [1][2].

A. Enrollment Mode

The enrollment mode is a learning phase which aims to collect biometric information on the people to be identified (Figure 1). During this phase, the biometric characteristics of individuals are captured by a biometric sensor, then represented in digital form (signatures), and finally stored in the database [2].

Fig.1: Block diagram of a Biometric System in Enrollment Mode

B. Verification Mode

The verification or authentication mode is a one-to-one (1:1) comparison, in which the system validates the identity of a person by comparing the biometric data entered with the biometric template of that person stored in the system database [2]. Figure 2 illustrates the block diagram of a biometric system in Verification Mode.

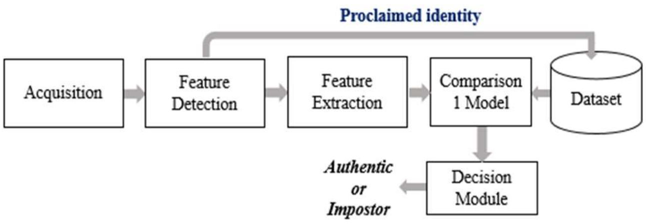

Fig.2: Block diagram of a Biometric System in Verification Mode

C. Identification Mode

In this mode, the biometric characteristics of the person to be identified are acquired and compared to those of all customers known to the system and stored in a database (Figure 3). This is a one-to-many (1:N) comparison. Identity identification is typically used to prevent a person from using multiple identities [2].

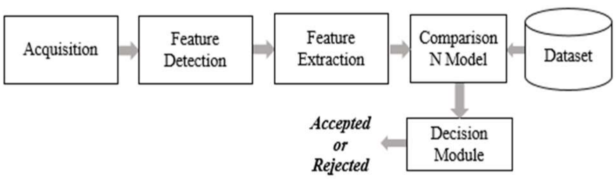

Fig.3: Block diagram of a Biometric System in Verification Mode

2. Architecture of Biometric Systems

The architecture of a biometric system varies depending on the biometric characteristics used, application constraints and security requirements. However, these basic components are, generally, present in most biometric systems [3]. Figure 4 illustrates the Architecture of biometric systems.

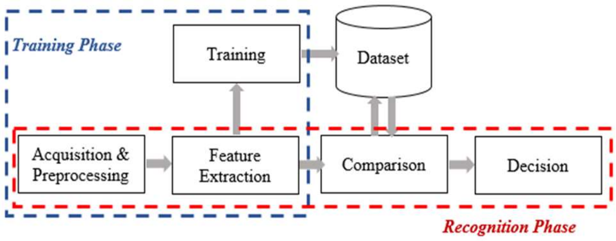

Fig.4: Architecture of biometric systems

A biometric system is essentially a pattern recognition system that acquires biometric data from an individual, then compares a set of characteristics extracted from this data to a set of previously stored data to finally be able to execute an action or take a decision based on the result of this comparison [3][4].

A. Acquisition Phase

This step is done using various devices like cameras, fingerprint scanners, retina readers, etc. These devices capture the specific biometric characteristics of the individual. The quality of captured data is essential to ensure the accuracy and reliability of the biometric identification process.

B. Feature extraction Phase

This phase takes as input the data acquired by the capture module and extracts only the information in order to form a new representation of the data. Ideally, this new representation is supposed to be unique for each person and invariant to intra-class variations.

C. Matching Phase

The extracted biometric features are compared with the templates stored in the database as vectors, assessing their degree of similarity to that vector, measured in terms of difference or distance.

D. Decision Phase

The decision strategy plays a crucial role in the authentication of individuals. To do this, the user's biometric characteristics are extracted and compared with the vectors stored in the database. This comparison is made by measuring the degree of similarity between the extracted biometric characteristics and the stored vector, generally, in the form of difference or distance. In this phase, it is possible to verify the identity declared by a user or to determine the identity of an unknown person based on the degree of similarity between their biometric characteristics and those stored in the database.

3. State of the Art on Facial Recognition

Human beings generally find it easy to identify a person from their face. However, for machines, automatic face recognition poses a significant challenge. This problem has generated considerable research in recent years. Facial recognition is an image processing technology used to identify or verify the identity of an individual based on unique facial characteristics.

It uses algorithms to analyze facial characteristics, such as distance between eyes, nose shape, eye contours, and lip and mouth size, to create a unique digital signature for each individual.

Facial recognition is used in a variety of applications, including security, marketing, surveillance, human resource management, criminal research, etc. It can enable rapid and efficient identification of individuals, as well as real-time monitoring of activities.

4. Steps of Facial Recognition

In this section, we will explain the main steps of facial recognition [5]:

A. Acquisition

The image of the face is acquired using a camera or other imaging device.

B. Processing

The image is processed and normalized to remove unwanted distortions and noise.

C. Face Detection

The system uses face detection algorithms to detect the position and contours of the face in the image.

D. Feature Extraction

Facial features such as distance between eyes, size and shape of eyes, nose and mouth are extracted from the image.

E. Comparison

Extracted facial features are compared to those stored in a database of known faces to find a match.

F. Decision Making

Based on the match found, the system makes a decision on the identity of the person. In some applications, there may be additional steps, such as machine learning to improve recognition performance and verification of the person's identity using biometric methods.

5. Principal Component Analysis (PCA)

PCA is a very popular method of finding the principal components of faces from a set of example images. Each face can then be described by a linear combination of these eigenvectors. Although PCA is fast, simple and popular in pattern identification, it is not optimized for class separability (discrimination). This multivariate analysis technique can be used for facial recognition. The most used algorithms in the PCA method are summarized as follows [6]:

- Center the data: The facial Images are first centered by subtracting the average of all the images.

- Calculate the covariance matrix using the centered data. It represents the relationship between different facial features.

- Calculate the principal components by diagonalizing the covariance matrix. These are vectors that represent the directions in which the data has the most variance.

- Reduce dimensionality: The principal components that have the highest eigenvalues are selected because they contain the most information about the data. These components are used to reduce the dimensionality of the data space.

- Project the data onto the new dimensions defined by the selected principal components. This step helps reduce data complexity and improve facial recognition performance.

- Classify the images by comparing their projection on the new dimensions with the projections of all other images in the database. Images that have similar projections are considered the same and can be used to identify a person.

III. State of the Art on the Human Visual System

Research on the human body has always aroused great interest, in particular, to understand its architecture and its interactions. The HVS has been studied in depth to discover the cells and neurons that compose it, in order to better understand the system as a whole and to better treat certain pathologies [7].

The HVS is a complex and sophisticated system that allows us to perceive and interpret visual information. Advances in imaging technology have made it possible to better understand how HVS works and to apply it in image processing. The latter uses computer techniques to enhance images and extract information from them [8][9]. These techniques often take inspiration from human visual perception to improve their accuracy and efficiency. Image segmentation involves dividing an image into different regions or objects and segmentation algorithms often take inspiration from human visual perception to detect object boundaries and contours. The ability of our visual system to process visual information quickly and efficiently is incredibly powerful. Technological advances have made it possible to develop artificial vision systems that attempt to imitate this ability to solve complex problems in various fields, such as image recognition, video surveillance, autonomous navigation, robotics. HVS is able to detect subtle features in images, such as shapes, textures, colors and movements. This capability can be used for practical applications such as facial recognition in security systems. In summary, the motivation to apply HVS is mainly due to its power, ease of use, and ability to process complex visual information.

A. Modeling of the Human Visual System

HVS modeling is an interdisciplinary area of research that aims to understand how humans visually perceive and interpret their environment. Advances in computing and Artificial Intelligence technologies have made it possible to develop increasingly sophisticated models to describe visual processes and associated behaviors [7][8]. HVS models are generally based on insights from psychology, neuroscience and computer science. They use data obtained from psychophysical experiments, behavioral studies, brain images and other sources to create mathematical and computational models that replicate human visual perception [9][10].

An example of a well-known model is the Marr model, which describes the SVH in three levels of representation

- At the primary level, visual information is processed in the primary visual cortex from the retina, using algorithms such as spatial and temporal filtering, edge detection, orientation selectivity and luminance perception.

- At the 2.5D representation level, visual information is processed to create a two-dimensional representation of the visual scene, taking depth information into account. Algorithms used at this level include stereovision, motion disparity, textures and contours.

- At the 3D representation level, visual information is used to create a three-dimensional representation of the visual scene. The algorithms used at this level include depth perception, 3D scene reconstruction, scene segmentation into objects and object recognition.

Although this model is a simplification of the actual complexity of the HVS, these three levels are interconnected and work together to produce visual perception.

B. Luminance perception

The HVS is capable of perceiving a wide range of luminance, from a few thousandths of candelas per square meter (cd/m²) under night vision conditions (Scotopic) to several thousand candelas per square meter under bright light conditions (Photopic) [11][12].

Luminance perception involves the complex interaction between the physical properties of light, the properties of photoreceptor cells in the retina, and the visual information processing mechanisms in the brain that create a subjective perception of brightness. and contrast in the visual environment.

C. Definition of Contrast

Contrast is one of the most studied parameters in psychovisual experiments and also the most exploited in image quality measurements. Visual contrast is defined as the relative difference in luminance between two regions of the image, divided by the average luminance of these two regions [9][13].

Contrast is an important parameter in the study of visual perception and image quality. Contrast, generally used in HVS models, depends on several parameters such as shape, spatial frequency, orientation of the stimulus used and also the complexity of the neighborhood. Several definitions have been proposed since Michelson's but no universal definition is known to date (Figure 5).

Fig.5: Brightness contrast

1. Michelson Contrast

It is defined as the ratio of the difference in luminance between a light region and a dark region, divided by the average of the luminance of these two regions [9][14]. This definition was introduced by Michelson and is widely used in the fields of human vision, imaging and photography.

$$C_M = \frac{L_{max} - L_{min}}{2L_{moy}} \quad \textbf{(1)}$$

Where: L_{max} and L_{min} correspond to the maximum and minimum luminance values respectively.

2. Contrast by Weber Fechner

The response of the Human Visual System depends more on local variations of luminance ΔL in relation to the surrounding luminance L, than on absolute luminance values. This property is known under the Weber-Fechner law. It is one of the first quantitative models of luminance perception [9].

We perceive a minimum deviation ΔL for a target of luminance L+ΔL on a uniform background of luminance L, called adaptation. The $\Delta L/L$ ratio is practically constant over a wide range of brightness. Mathematically, the Weber contrast is modeled by the relation (2):

$$C_w = \frac{\Delta L}{L} \quad \textbf{(2)}$$

3. Peli Contrast

Decomposition into frequency channels makes it possible to take into account the properties of human vision, which is more sensitive to certain frequencies than others by decomposing the image into several frequency channels. Specific contrast treatments can be applied to each channel in order to optimize the contrast throughout the image [11][15].

Once the image has been decomposed into several frequency channels, the Peli contrast can be calculated for each channel individually using the formula given in (3). This contrast measurement can then be used to guide adaptive contrast treatments that take into account the properties of human vision.

$$C_i(m,n) = \frac{L_i(m,n)}{\sum_{k=0}^{i-1} L_k(m,n)} \quad (3)$$

Where : i represents the i^{th} canal radial

The denominator represents the local average luminance which corresponds to all channels of spectral support lower than that of the i^{th} channel.

D. Multi-Channel Organization

The sensitivity of different cells of the HVS to certain types of information, such as color, orientation or frequency, suggests that there is a prior organization of the information before its processing. The results of numerous psychophysical experiments support this idea and present the HVS as a multi-channel system [16].

This means that the visual system is organized into several channels, each specialized for processing a specific type of information. This organization allows faster and more precise perception of the visual environment, as well as more effective adaptation to complex and varied visual situations.

It is true that single-channel modeling is not sufficient to completely explain the behavior of the HVS in the face of these stimuli. Indeed, HVS uses a set of channels to analyze input signals, each sensitive to a specific orientation and spatial frequency.

These channels are separable in a polar representation, meaning they can be described by their amplitude and phase at different spatial orientations. The characteristics of these channels allow the HVS to process visual information selectively, responding only to stimuli that match the characteristics of the activated channels [9][11].

By combining information from different channels, the brain is able to reconstruct a complete image of the visual environment.

E. *Perceptual Channels Decomposition*

The decomposition into perceptual channels reflects the spatio-frequency selectivity of the HVS. It implements a division of the spatio-frequency plane as obtained by a Fourier transform.

This decomposition proposes a frequency tiling into seventeen channels. It is strongly inspired by Watson's Cortex transform. However, the number and characteristics of the channels are different by dynamic division into radial frequencies. The angular selectivity varies as a function of the radial frequencies unlike the Watson decomposition. The DCP is based on a set of psycho-physical experiments.

Under standardized viewing conditions, there are four radial spatial frequency domains (LF, II, III, IV) [9]:

- The LF (Low Frequency) domain corresponds to spatial frequencies between 0 and 1.5 cpd (cycles per degree).
- Domain II corresponds to frequencies between 1.5 and 5.7 cpd.
- Domain III corresponds to frequencies between 5.7 and 14.2 cpd.
- Domain IV corresponds to frequencies between 14.2 and 28.2 cpd.

The angular selectivity depends on the spatial frequency domain considered as follows (Figure 6):

- For the LF domain, there is no angular selectivity.
- For domain II, the angular selectivity is 45°, which defines four oriented channels.
- For domains III and IV, the angular selectivity is 30°. which defines six oriented channels for each domain.

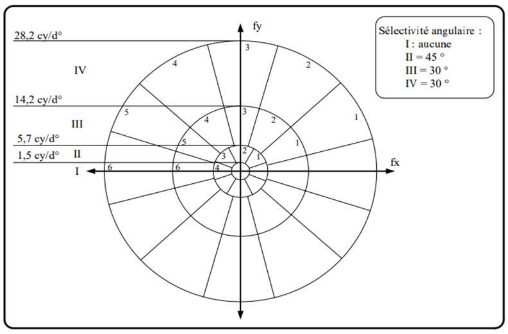

Fig.6: Frequency tiling of the Perceptual Channels Decomposition

IV. Implementation Of A Facial Recognition System Based On HVS

In this section, we will present a practical implementation of HVS based face recognition techniques using MATLAB. The HVS is the main inspiration for the development of this technique, as it is capable of recognizing and distinguishing faces effectively using features such as shape, color and texture.

We will use images of faces of different people for our facial recognition system. Next, we will test the performance of our method by verifying the identity of each individual. We will also discuss the limitations and advantages of this approach, as well as future directions for research in this area. Ultimately, our goal is to test the effectiveness of this method in contributing to the advancement of facial recognition research.

A. *Extended Yale Face Database B*

The "Extended Yale Face Database B" is a collection of facial images used for facial recognition research. This database contains images of 133 people, each with 20 images of their face. The images were taken from different angles and with varying lighting conditions, allowing the effectiveness of facial recognition algorithms to be tested in real-world situations.

The "Extended Yale Face Database B" is used in various facial recognition applications, including identity verification, surveillance, and emotion analysis. The images are of high quality and the subjects represented are of different ages, genders and ethnicities, thus allowing a more in-depth study of the performance of facial recognition algorithms in varied scenarios.

Using this database, we can test the algorithms' ability to identify people from images of faces taken under different lighting conditions. The results can be used to improve the efficiency and accuracy of facial recognition systems, which is crucial in many security and surveillance applications.

B. *Architecture of Face Recognition System based on SVH*

Figure 7 illustrates the architecture of the facial recognition system based on SVH [17]:

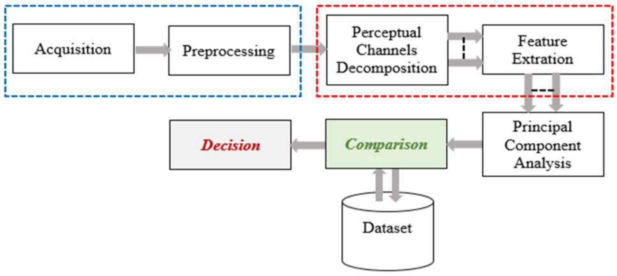

Fig.7: Face Recognition System overview

1. Acquisition System

The first step to loading an image into Matlab is to use the "*imread*" function. This function allows us to read an image from a file stored on our computer and store it in a Matlab variable. We can then use other Matlab functions to process or display this image, such as "*imshow*" to display it on the screen [17].

2. Facial Pretreatment

The image is Converted to grayscale using the "*rgb2gray*" function. Image noise is reduced by applying a Gaussian Filter. This helps improve the accuracy of face detection. A face detector is initialized using the Viola-Jones detection method, which is a popular technique for detecting faces in images. Bounding boxes of faces in the image are detected using the face detector.

Next, we initialize a "*for*" loop to extract each face from the image using the detected bounding boxes. In each iteration of the loop, the coordinates of the bounding box are stored in the variable "*bbox*". The Region Of Interest (*ROI*) corresponding to the bounding box is extracted using the "*imcrop*" function.

Finally, the *ROI* is displayed using the "*subplot*" function for each face detected in the image [17].

3. Decomposition into Perceptual Channels (PCD)

To perform the decomposition into channels, we use the wavelet transform which allows us to decompose the image into different frequency bands, each containing specific information about the image. The "*dwt2*" function is used to perform this wavelet decomposition of the "*img*" image using the 'db6' wavelet family (Daubechies 6) with four domains.

The four domains correspond to the wavelet decomposition coefficients of the image, each having a different angular selectivity. The decomposition coefficients are divided into four matrices [17]:

- **LL1:** Matrix of approximation coefficients (**Low-Low**) which contains the low frequency information of the image. This matrix represents the image at a lower scale with lower resolution.

- **HL1:** Horizontal detail coefficient matrix (**High-Low**) which contains high frequency information in the horizontal direction of the image.

- **LH1:** Vertical detail coefficient matrix (**Low-High**) which contains high frequency information in the vertical direction of the image.

- **HH1:** Matrix of diagonal detail coefficients (**High-High**) which contains the high frequency information in the diagonal direction of the image.

Figure 8 represents Perceptual Channels Decomposition of a Face Image [17]:

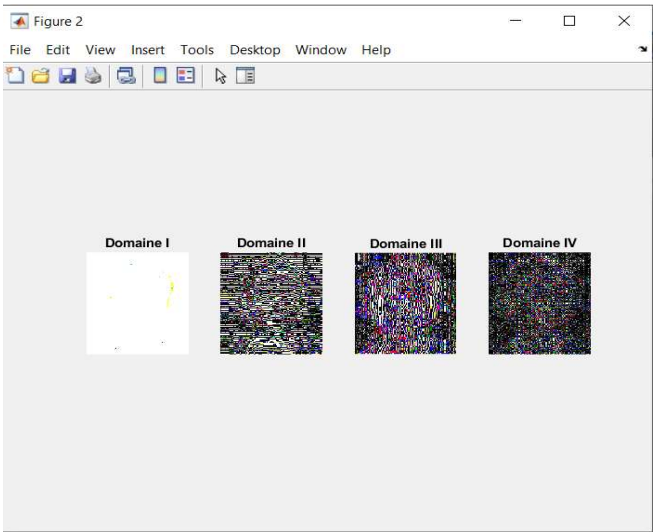

Fig.8: Decomposition into Perceptual Channels of a Face Image

4. Feature Extraction

After decomposing the image into four domains of different selectivity, we applied the HOG method to extract features using different sizes of feature extraction cells [17].

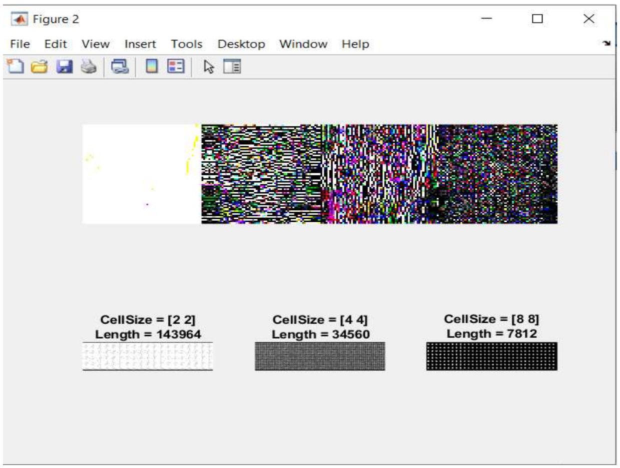

Fig.9: Feature extraction using different cell sizes HOG.

5. Feature Vector

After feature extraction using HOG method, we can apply Principal Component Analysis (PCA) method for feature selection and dimension reduction of feature vectors.

6. Classifier

The classifier is an essential element in learning. It is an algorithm or model that learns to classify or predict data based on input characteristics or variables. In our work, we use the SVM (Support Vector Machine) classifier to perform the classification of our data. The SVM is a linear or non-linear classifier which seeks to find the optimal hyperplane to separate the different classes in the feature space.

7. Database used

In our work, we use a database of 30 classes. The database is divided into two parts:

- a training database
- a test database.

The learning base is used to train the system; it uses the database. The test database uses the remaining 30 of the database to test the system [17].

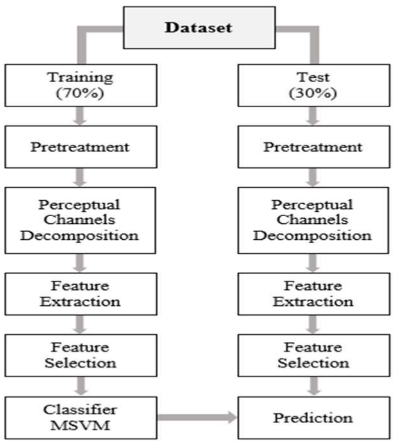

Fig.10: The breakdown of the database

Here are the predictions of our classifier

V. RESULTS AND EVALUATION

To evaluate and see the effect of our HVS based face recognition system, we first need to create a validation baseline for our system. We will then check if our system is able to identify the face images that have been provided to it and that have already been used to train the system through an SVM classifier [17].

Modifies the database structure as follows:

- 10% for validation
- 20% for testing
- 70% for training

To clearly visualize the Confusion Matrix, we use 15 classes with 20 images each (Figure 11).

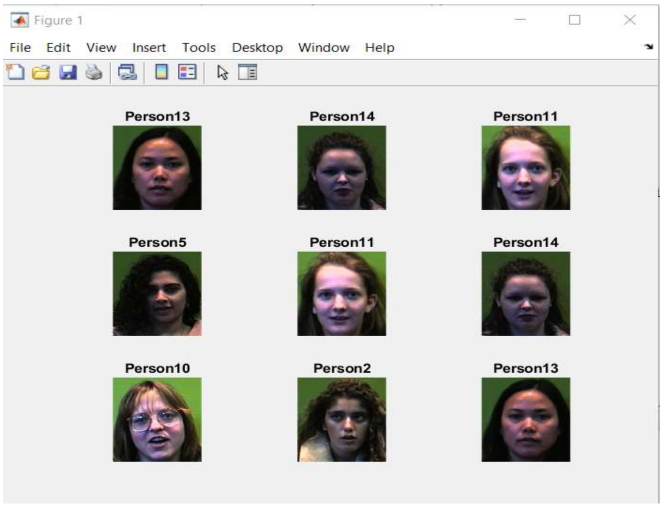

Fig.11: MSVM Classifier predictions (15 classes)

Figure 12 illustrates the confusion matrix for 4 classes.

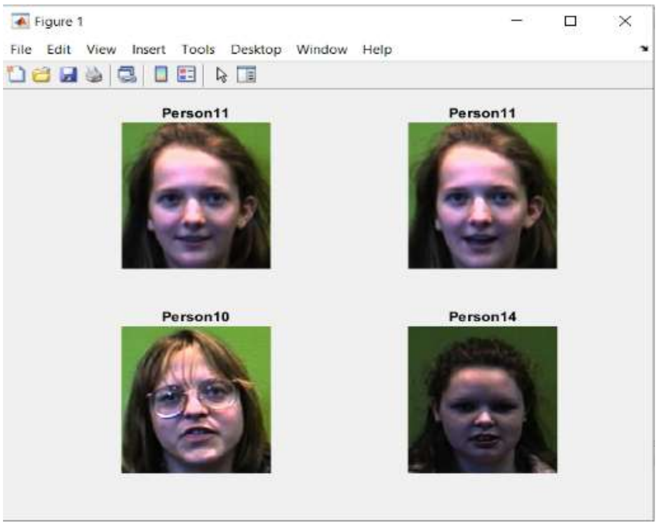

Fig.12: MSVM Classifier predictions (4 classes)

Figures 13 and 14 show the confusion matrices for 15 and 4 classes respectively [17].

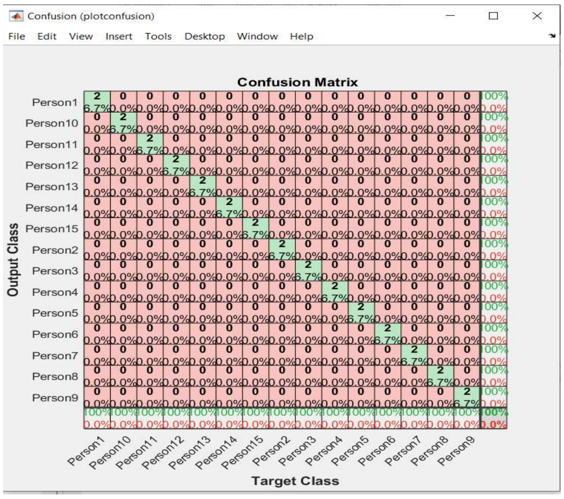

Fig.13: Confusion Matrix of 15 classes

Fig.14: Confusion Matrix of 4 classes

VI. CONCLUSION

Biometrics is a field that is both exciting and complex and the number of research is growing universally. Currently, the use of biometric systems such as facial or fingerprint recognition are essential in high security environments because they make it possible to recognize or verify the identity of people, with a significant degree of reliability. In this paper, we are interested in developing a robust and efficient face-based biometric system. Beforehand, we introduced some general concepts about biometrics. We have seen that a typical biometric system can be represented by four main modules, namely, the capture module, the feature extraction module, the matching module and the decision module. Subsequently, we presented a state of the art on facial recognition. We followed a well-defined structure by dividing the database into three distinct parts: training, testing and validation. In our approach, we applied SVH to decompose images into different frequency scales. Then, we extracted the features using the Histogram of Oriented Gradients (HOG) method. This step allowed us to represent each image by a vector of significant characteristics. To reduce the dimensionality of the data and improve the efficiency of the model, we applied principal component analysis (PCA). This technique allowed us to select the most discriminating components and use them to represent faces in a reduced-dimensional space. Finally, we used a classifier to perform face prediction. Different classification methods can be used; such as support vector machines (SVM). Our face recognition system based on the PCA method gave good results in terms of accuracy and performance. We obtained an accuracy of 100%.

These results are encouraging and very satisfactory and show the effectiveness of the algorithms developed for the extraction of discriminating characteristics. This implementation brightens the horizon for carrying out other work exploiting other biometric modalities by combining them. It is worth noting that this project opens so many doors to explore. In this sense, we can consider as future perspectives to make possible improvements which are mainly summarized as follows:

- Test the capacity and performance of the approach developed on other databases.

- Apply other techniques to facial recognition, other than global approaches.

- Create a biometric system on FPGA type electronic components to respect space constraints and real-time processing.

- Make the biometric system portable thanks to improving the performance of FPGA programmable circuits.

References

[1] N. Morizet, “Biometric recognition by multimodal fusion of Face and Iris”. PhD Thesis, Specialty: Signal and Images. National School of Telecommunications. Paris, France, March 2009.

[2] J.L.Wayman, “Fundamentals of Biometric Authentication Technologies”, In- ternational Journal of Image and Graphics, Vol. 1, No. 1, pp. 93-113, 2001. DOI:10.1142/S0219467801000086

[3] F.Z. Allam, L. Hamami-Mitiche & H. Bousbia-Salah. « Evaluation and Comparison of the Performance of Biometric Recognition ». International Journal of Industrial Engineering & Production Research. Volume 33, No.1, pp. 1-12, March 2022. DOI: 10. 22068/ijiepr.33.1. 6.

[4] Anil K. Jain, P. Flynn, A. Ross, "Handbook of biometrics", Springer, 2007. ISBN-13 978-0-387-71040-2

[5] Henriette Ruhrmann, "Protecting Human Rights in Policy Strategies for Facial Recognition Technology in Law Enforcement", Goldman School of Public Policy, University of California Berkeley, Citris Banatao Institute, May 2019.

[6] Peng P, Portugal I, Alencar P, Cowan D. “Un cadre logiciel de reconnaissance faciale basé sur l'analyse des composantes principales”. PLoS ONE, Vol. 16, No. 7: e0254965, 2021. DOI: 10.1371/journal.pone.0254965

[7] F.Z. Allam, H. Bousbia-Salah, & L. Hamami. “Modeling of Biometric Recognition Based on Human Visual System”, International Journal of Advanced Trends in Computer Science and Engineering, vol. 9, no.1.2, pp. 198-204, 2020. DOI : 10.30534/ijatcse/2020/2991.22020

[8] F.Z. Allam, H. Bousbia-Salah & L. Hamami-Mitiche. « State of the Art on Human Visual System Modeling ». advanced Studies: Euro-Tbilist Mathematical Journal 16, Tbilisi Centre for Mathematical Sciences, supplement issue 2, pp. 119-133, 2023. International Journal of Industrial Engineering & Production Research. Volume 33, No.1, pp. 1-12, March 2022. DOI: 10.32513/asetmj/1932200823210.

[9] A. Ninassi, “From the local perception of coding distortions to the global appreciation of the visual quality of images and videos. Contribution of the visual attention in the judgment of quality”. PhD Thesis, specialty: Signal Processing and Applied Informatics. Polytechnic School of the University of Nantes, France, March 2009.

[10] N. Bekkat, “Objective criterion of subjective quality of monochrome images. Model design and experimental validation”. PhD Thesis, Specialty: Signal Processing and Applied Informatics. Polytechnic School of the University of Nantes, France, 2001.

[11] F. Autrusseau, “Image tattoo based on the modeling of the human visual system and the mojette transformation”. PhD Thesis, Specialty : Image Processing. Polytechnic School of the University of Nantes, France, November 2002.

[12] Lagadic-Gossmann D “The Human Visual System”. University of Rennes I, 2017. Available from: http://people.rennes.inria.fr/Eric.Marchand/ESIR/ESIR2/BINP/svh.pdf

[13] D. Cherifi “Amélioration et Évaluation de la qualité des images”, Doctorat en Sciences en Physique, Faculté de Physique, Université des Sciences et de la Technologie d’Oran Mohamed Boudiaf, 2015.

[14] A.A. Michelson, Studies in Optics. Department of Physic. The University of Chicago. USA 1927.

[15] E. Peli, « Contrast in complex images ». Journal of the Optical Society of America, Vol. 7, No. 10, pp. 2032-2040, 1990. DOI: 10.1364/JOSAA.7.002032.

[16] P. Le Callet, & D. Barba, “Color perception model. Application to image quality assessment”. Signal Processing, Color Digital Image, Vol. 21, Special issue: Color Digital Image, pp. 61-77, 2004.

[17] F.Z. Allam, “Fusion of Biometric Techniques for improved person recognition”, Thesis, Specialty: Signal and Communication,. National Polytechnic School, June 2023.

Fatima Zohra Allam-Chergui (M. Sc 2006, Doctorate 2023). is a Assistant Professor at the Ecole Nationale Supérieure des ICT et de la Poste. She is the author of several International Publications. His research focus is based on Image Processing, more precisely, Biometric Images. Its objectives are multiple, among others, the implementation of Biometric Systems on embedded circuits of the FPGA type, representation and projection of signals from the time domain to the frequency domain with the aim of exploiting the contribution of spectral information rather than spatial.

Latifa Hamami-Mitiche (M.Sc. 1988, Ph.D. 2002) is a full Professor in the Department of Electronics at Ecole Nationale Polytechnique of Algiers, Algeria. She is author more than 150 scientific papers. Her research interests include Medical Image Processing, ISAR Image Processing, Optical Character Recognition, Biometrics and Embedded System, FPGA and ASIC Design, System on Chip.

Hicham Bousbia-Salah is currently Associate Professor, Researcher in Signal Processing at Ecole Nationale Polytechnique, Algiers. He earned his Engineering degree in Electronics at Ecole Nationale Polytechnique, Algiers in 1981, his Master degree in Computer Engineering at Wayne State University in USA in 1984 and his PhD in Electronics in Signal Processing from the Ecole Nationale Polytechnique, Algiers in 2006. Currently, he is interested in the field of blind separation of multiple sources from convolutive mixtures and its implementation in signal processing.

Quantifying Electric Charge on Cap-Pin Glass Insulator: Investigating the Impact of Pollution through Simulation and Experimental Approaches

Rabie Salhi, Abdelouahab Mekhaldi, Madjid Teguar, and Omar Kherif

Abstract—The objective of this paper is to investigate the behavior of electric charges on cap-pin glass insulator under 50 Hz AC voltage. The study is conducted using COMSOL Multiphysics to understand the charge location, polarity, and parameters affecting their behavior. A 2D-axisymmetric insulator design is used to visualize the overall charges on the insulating system (space charge) and along the insulating surface (surface charge density) under uniform and non-uniform pollution conditions. The research shows that the total charge accumulates over the surface area of the glass material. To quantify the amount of this charge, a simulation method based on using the surface integral of the electric displacement field over this area is introduced, which is supported by experimental tests. Comparing both simulation and experimental results provides insights into the simulation reliability and the parameters' affinity used to those of the real model. Moreover, the simulation helps to identify the critical area where a high amount of charges is accumulated. The findings of this study are presented and examined.

***Keywords*—electric charge, glass insulator, COMSOL, space charge, surface charge density, simulation, charge accumulation.**

NOMENCLATURE

AC	Alternating Current.
2D	Two Dimensional.
HVDC	High Voltage Direct Current.
HVAC	High Voltage Alternating Current.
HV	High Voltage.
ENP	Ecole Nationale Polytechnique.
LRE	Laboratoire de Recherche en Electrotechnique.
SPS	Site Pollution Severity.
IEC	International Electrotechnical Commission.
FEM	Finite Element Method.

I. INTRODUCTION

Electric power consumption has been increasing at a rapid pace worldwide in recent years. In order to meet the growing demand, new power generators must be built, and bulk energy must be transferred. This requires the construction of new overhead transmission lines. Insulators are crucial components of high voltage transmission lines as they provide the dielectric function between live conductors and the structure support, as well as mechanical strength [1]. However, their performance is significantly affected by factors such as material degradation, pollution severity, and different weather conditions (heat, ice, humid air, dust) [2]. Insulator failures can have a severe impact on the electrical power system, so studying and understanding insulator surface behavior is essential, and it requires high attention to ensure their optimal functioning [3].

The premature aging of materials and the occurrence of flashovers in insulators can be related to the accumulation of charge on their outermost surface [4]. These charges play a critical role in determining how the insulator surface interacts with external atmospheric conditions, such as contamination, water droplets, humidity, and others. For this reason, various techniques have been employed to diagnose insulator issues [5]. In recent years, charge distribution analysis techniques have garnered significant interest among researchers [4]. Additionally, several studies have utilized surface charge as a tool to analyze insulators in both HVDC and HVAC systems [6]. The study of charge distribution in insulators has been conducted through both experimental and simulation approaches [4]-[6].

Surface charge is of great interest because it significantly affects the electric field [7]. When the amount of charges flowing to the most contaminated particles located on the insulator surface increases, it can create a high electric field intensity in that location [8]. If this electric field intensity surpasses the breakdown voltage, it can result in a breakdown [7].

Thermal aging diagnosis of polymeric insulators was investigated in [9] using features extracted from space charge accumulation, which is measured in the laboratory using the Pulsed Electro Acoustic system. In [4], a steel mesh was placed around the glass insulator to capture charge accumulation at a distance of 2cm from the insulator edge, which could be useful for monitoring insulators under AC voltages. Laboratory observations have shown that the behavior of electric charge under electric field intensity creates considerable motion activity on water droplets [10]. Understanding these charges can be an effective way to predict insulator aging in the presence of water droplets.

Manuscript received December 24, 2023; revised June 27, 2024.

R. Salhi, A. Mekhaldi and M. Teguar are with the Laboratoire de Recherche en Electrotechnique (LRE), Ecole Nationale Polytechnique (ENP), B.P. 182 El Harrach, Algiers 16200, Algeria. e-mail: (rabie.salhi@g.enp.edu.dz).

O. Kherif is with the Advanced High Voltage Engineering Research Centre, School of Engineering, Cardiff University, Cardiff CF24 3AA, UK. e-mail: (kherifo@cardiff.ac.uk).

Digital Object Identifier (DOI): 10.53907/enpesj.v4xi1. 255

Electrolyte corrosion can significantly affect HV lines during operation. In [11], the authors developed a sophisticated system for in-situ insulator monitoring based on charge to classify corrosion severity.

Simulation-based analysis regarding the electric charge study is one of the most powerful tools to understand and clarify some of the characteristics of insulators found by experimental tests [12]. The results of simulation studies [4],[6] have demonstrated a good correlation with laboratory tests. Furthermore, modeling enables us to illustrate the impact of the amount of charge on the electric field and potential changes [13].

As mentioned earlier, electric charge is closely related to factors like corrosion, temperature, and insulator aging. In this work, we aimed to understand the volumetric and surface charge density, as well as the overall charge on glass insulators, which can significantly impact their behavior. By comparing simulations with experimental data for specific electrical characteristics, such as electric charge, we not only verify the results but also enhance their interpretation and understanding. This approach can also open new research avenues, such as optimization applications, potentially improving the performance of these insulators.

There is a lack of understanding about the distribution of charges on insulating surfaces, particularly for insulators under AC voltages [4]. Therefore, in this paper, we aim to present features that describe the charge characteristics of HVAC insulators. The 1512L cap-pin insulator was used in an experimental investigation conducted at ENP's High Voltage Laboratory under uniform and non-uniform pollution conditions. For both scenarios, we designed and studied a 2D-axisymmetric insulator model using COMSOL software. We investigated space charge accumulation on the glass insulating material, as well as surface charge along the leakage path, and we explained the approach to measuring the waveforms of the charge accumulated on the insulator. This simulation technique for quantifying the global charge has not been done before. We conducted experimental tests to provide a comparative study to validate the simulation results. As a result, we found good agreement between the experimental and simulation tests in terms of the charge waveform, where pollution evaporation was not included

II. Laboratory Test Setup

A. Instruments and Equipment Used

The 1512L cap-pin glass insulator was the main element investigated in this paper. The experiment was conducted at ENP's High Voltage Laboratory (LRE), and the experimental setup diagram is presented in Fig. 1. The system used to perform the tests included the following equipment:

- Contacter and Filter.
- Regulating transformer (380/ 0 to 380 V, 50 kVA, 50 Hz).
- HV Test Transformer (300 kV, 50 kVA, 50 Hz).
- AC capacitive voltage divider with a ratio of 1:1000 ($C_1 = 500$ pF and $C_2 = 0.5\,\mu$ F).
- Measuring capacitor ($C_{\mathrm{m}} = 0.5\,\mu$ F) placed in serie with the insulator.
- Digital oscilloscope to visualize and recorde the charge and the applied voltage waveforms (INSTEK GDS-3504, with 500 MHz of bandwidth).

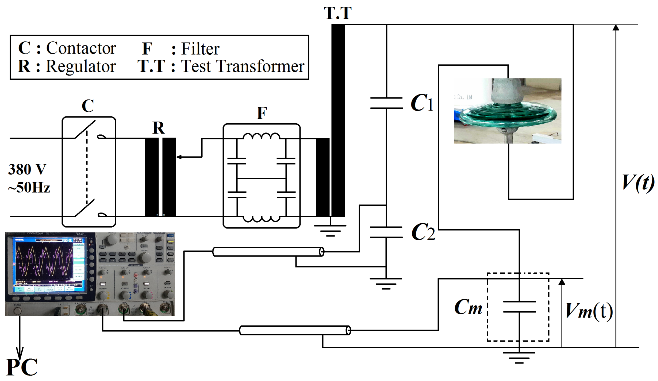

Fig. 1: Laboratory setup diagram

The voltage measured at the capacitor C_{m} terminals, $V_{\mathrm{m}}(t)$, provides information about the charge flow throughout the insulator [14]. The capacitor Cm should be connected in series with the insulator under examination. Based on a previous study [15], it can be noted that the consumption of the oscilloscope can be neglected for the same circuit diagram. The charge over the capacitor has a value so close to the charge over the insulator, with a small error. Therefore, the charge waveform ($Q(t)$) at each instant is measured through the voltage obtained from the oscilloscope as expressed below, where $V(t)$ » $V_{\mathrm{m}}(t)$, and C_{in} is the insulator capacitor.

$$Q(t) = C_{\mathrm{m}} V_{\mathrm{m}}(t) = C_{\mathrm{in}}(V(t) - V_{\mathrm{m}}(t)) \approx C_{\mathrm{in}} V(t) \qquad (1)$$

B. Pollution Preparation and Application Procedures

The pollution has been prepared at the ENP's laboratory (LRE). In order to replicate the site pollution severity (SPS) classes, we have adopted in this study the following amounts of NaCl mixed with one liter of distilled water (0, 100, 250, 500 and 750 mg) corresponding to conductivity values respectively 5, 150, 340, 720, 1050 (μS/cm). Those values match to: very light, light, medium, heavy and very heavy as reported on the IEC 60815 standard [16]. Applying the pollution layer on the insulator surface involves using a sprayer, to ensure a uniform layer over the entire surface, The IEC 60507 [17] standard recommends maintaining a distance of 20-40 cm between the sprayer and the insulator surface.

Surface insulators require careful cleanliness before testing. The insulator surface is washed with water and dried with paper, and then cleaned using alcohol (99.8 %) to remove any remaining impurities. After leaving the insulator to dry for a while, the surface is covered with the appropriate pollution solution. Two types of pollution were used in this study: uniform and non-uniform. For the uniform case, the pollutant solution is evenly distributed over the surface using a sprayer fixed at 40 cm distance from the insulator. Six positions on both the upper and lower sides are targeted, and the surface is sprayed three times at each position to ensure full coverage. For the non-uniform case, pollution widths of 5, 10, 15, 20, and 25 cm were applied to the insulator surface starting from the HV side. The electrical conductivity adopted for this case was 1050 μS/cm, corresponding to very heavy pollution.

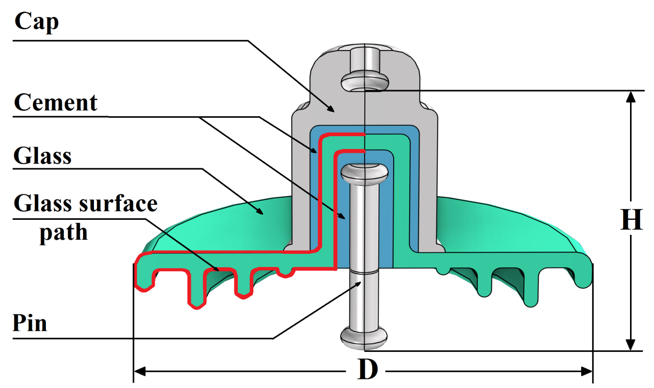

Fig. 2: Insulator model design and parameters

Table. I
MATERIAL PROPERTIES OF THE INSULATOR MODEL [18]

	glass	cap and pin	cement	air
Relative Permittivity ε_r	6	1	15	1.0005
Electric Conductivity σ **(S/m)**	10^{-14}	10^{4}	10^{-6}	10^{-18}

III. Simulation Arrangement

Our study employs the AC/DC electric current module within the FEM-based COMSOL software to model the 1512L cap-pin insulator. This insulator is composed of several materials, with their main electrical parameters listed in Table. I the value taking of the relative permittivity for the pollution layer is 80. The insulator's design is depicted in Fig. 2, with principal dimensions of Diametre D = 254 mm, Height H = 145 mm. The surrounding air is included in the simulation, with a radius of 2 m, and an extremely fine tetrahedral mesh was used in the simulation geometry to achieve high accuracy .

A time-dependent voltage was conducted in the simulation to simulate real operating conditions. The voltage was applied to the pin while the cap was grounded. To compare the simulation results with those obtained in the laboratory, charge waveform were extracted using the surface integral of the electric displacement field over the glass surface (S) as follows:

$$Q(t) = \iint_S \vec{D}.\mathrm{d}\vec{S} \tag{2}$$

The selection of the integration surface S is of utmost importance as it should encompass the highest accumulation of charge. Visualizing the space and surface charge densities aids in identifying and quantifying these accumulation zones. The detailed steps for determining the targeted surface have been previously outlined in our earlier study [19], where the charge accumulation tracking is presented as flowchart in the fig. 3.

In all simulation operations, the thickness of the pollution layer was determined as follows: for non-uniform pollution, the pollution layer thickness can be selected between 1 and 2 mm [20]. For uniform pollution, the thickness (th_p) was calculated by

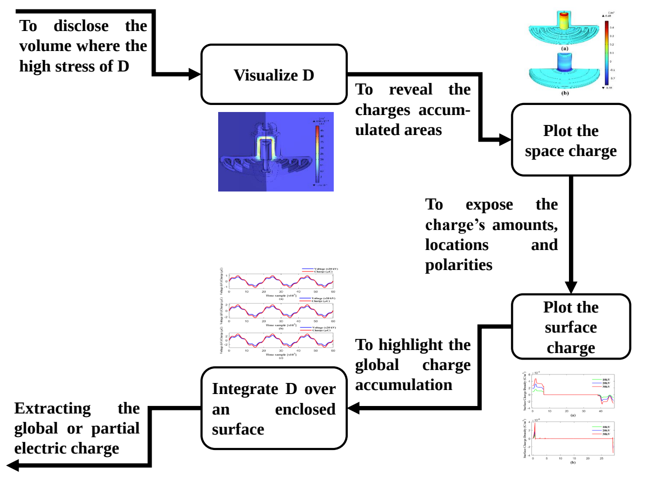

Fig. 3: Flowchart illustrating the quantification of the charge accumulation process [19]

dividing the volume of the pollution (V_p) by the insulator area (S_p) [21]. The surface area of the insulator was obtained using the "geometry surface measurement" feature in COMSOL, which yielded (S_p) = 0.147 m^2. The volume sprayed on the insulator surface was measured to be 15 ml or 1.5$\times$ 10^{-5} m^3, taking into account the volume of runoff that was subtracted from the total volume sprayed.

$$th_\mathrm{p} = \frac{V_\mathrm{p}}{S_\mathrm{p}} = \frac{1.5 \times 10^{-5}}{0.147} \approx 10^{-4} m \tag{3}$$

After several attempts, we found that the simulated charge was a hundred times greater than the experimental charge. This discrepancy is attributed to the fact that the electric current does not flow uniformly through the entire thickness of the insulator. Instead, an effective thickness that contributes to the electrical conduction phenomena was identified. This effective thickness represents only a portion of the total thickness [22], and in our study, it is estimated to be one percent according to the results obtained.

IV. Space and Surface Charge Densities

The results of space and surface charge densities obtained from the simulation are presented in this section. The glass surface path is divided into two zones: the first is where the glass is bonded to the electrodes by the cement (dielectric-electrode), and the second is along the leakage path where it is in direct contact with the air or covered with pollution (dielectric-air). All results are presented under an applied voltage of 30 kV. Indeed, to present the simulation results, we have focused on the maximum value of the sinusoidal signal rather than the entire waveform. This maximum value, which is 30 kV, represents the peak voltage. At this peak voltage, we observe the maximum charge that can accumulate on the surface of the insulator.

A. Uniform Pollution Case

Fig. 4 presents the space charge distribution on the glass material for the upper and lower surfaces, from very light to very high pollution severity. As we can see, positive charges accumulate on the surface area surrounding the HV end. Space charge

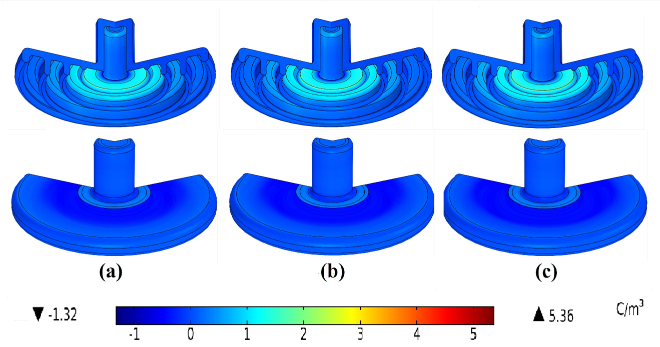

Fig. 4: Space charge distributions for different electrical conductivities, (a) 20 μS/cm, (b) 150 μS/cm, (c) 340 μS/cm.

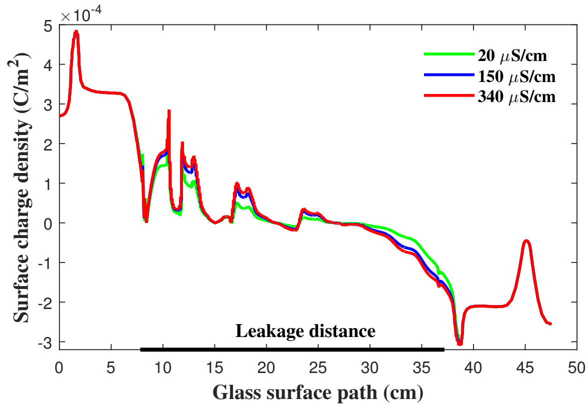

Fig. 5: Surface charge density along the glass surface path for different electrical conductivities.

intensity slightly increases with the increase of the pollution conductivity. For the area belonging to the second zone, high intensity of charge density is observed near the first shed. In fact, this area demonstrates the highest level of temperatures as mentioned in [18]-[23].

Fig. 5 presents the surface charge density along the glass surface path for different electrical conductivities. The charge density distribution along the surface is uneven. In the first zone, we observe that the charge densities are stable and not affected by pollution conductivities, while in the second zone, they are clearly affected by the electrical conductivities of the pollution. The results suggest that increasing the electrical conductivity leads to increased surface charges in the second zone. Along the leakage path, we observed that positive charges accumulate over a distance of 17 cm from the HV end, while negative charges accumulate over the rest of the length. An exceptional peak of positive charge is developed where the smallest distance throughout the glass material is reached between positive charges and the ground (cap).

B. Non-Uniform Pollution Case

Fig. 6 presents the space charge distribution on the upper and lower surfaces of the glass material for different widths of pollution layers. As we can see, positive charges accumulate on the lower surface area of the first zone as well as the area surrounding the HV-end in the second zone for all cases, except for the clean surface case, where charges are confined to the first zone. Negative charges accumulate close to the ground-end on the upper surface.

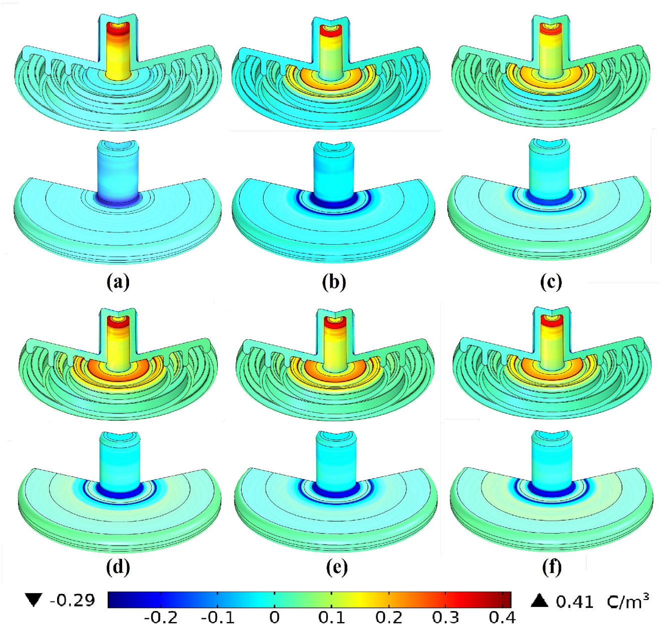

Fig. 6: Space charge distributions for different pollution layer width, (a) clean, (b) 5cm, (c) 10cm, (d) 15cm, (e) 20cm, (f) 25cm

The fig. 7 presents the surface charge density along the glass surface for different pollution layer widths. The distribution of the surface charge density along the surface is non-uniform. It remains stable in the first zone, while an insignificant change is observed in the second zone, except for the clean surface where it exhibits a different distribution compared to the others, near the high voltage (HV) and ground ends.

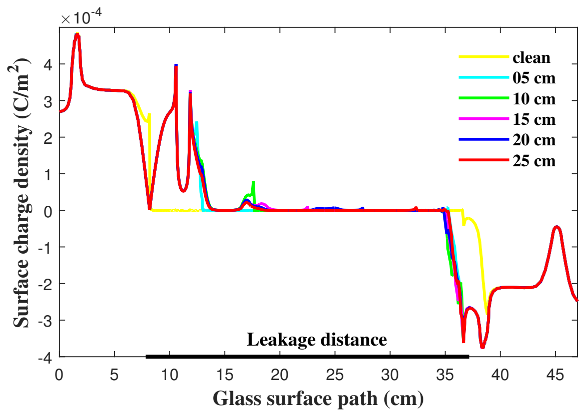

Fig. 7: Surface charge density along the glass surface path for different pollution layer width.

However, it reaches high values in the first 5 cm due to the fact that the charges are strongly influenced by both the distance between the two electrodes (HV and ground) and the electrical parameters of the material. The smallest distance between the two electrodes in the insulator is filled with glass material, while the largest distance is filled with air along the leakage distance. Moreover, the electrical conductivity and relative permittivity of the glass are higher than those of air. These parameters, which impact the charge distribution, are also discussed in [12].

The positive charges accumulate along the 10 cm length starting from the HV-end (5 cm in the case of the pollution width of 5 cm). As for the negative charge, they are trapped in the first 2 cm near the ground end at the dry band surface, where they create an important amount of charges.

V. Charge Waveforms Results

This section presents the global charges in all insulating systems. Tables II and III show the experimental results for flashover voltages under uniform and non-uniform pollution conditions, respectively. We observed that the flashover voltage decreases as either the pollution conductivity or the pollution width increases, leading to a corresponding reduction in the dielectric strength of the insulating system.

To prevent flashover occurrences that could damage the measuring devices, flashover voltages were determined before installing the charge recording setup. Consequently, voltages below the flashover thresholds were used to record the charge waveforms, ensuring that the applied voltages did not exceed 30 kV. However, for a non-uniform pollution width of 25 cm, the voltage had to be reduced to 15 kV due to a flashover event at 25 kV.

Table. II

Flashover voltages for uniform pollution conductivities

Conductivity (μS/cm)	20	150	340
Flashover voltage (kV)	71.5	69	61

Table. III

Flashover voltages for non-uniform pollution widths

Pollution width (cm)	0	5	10	15	20	25
Flashover voltage (kV)	72	70	65	55	35	25

A. Uniform Pollution case

The simulation and experimental results of the charge waveforms under a 30 kV applied voltage for various pollution conductivities are presented in Fig. 8. As depicted in the figure, the charge waveforms obtained from both the simulation and experimental tests exhibit a high degree of similarity. Furthermore, the maximum charge value increases as the conductivity value increases. The charge and voltage waveforms are nearly in phase, suggesting that the predominant behavior observed is capacitive.

The charge magnitudes as a function of electrical conductivities of the pollution under different applied voltages are depicted in Fig. 9. As evident from the figure, increasing conductivity values correspond to higher charge magnitudes. Additionally, it is noteworthy that, for the considered voltages and conductivities, the charge magnitude increases with the applied voltages. Furthermore, upon comparing the simulation and laboratory results for the pollution severity levels of very light, light, and medium, the average relative errors between simulation and laboratory are approximately 7.90 %, 5.94 %, and 7.25 %, respectively (as shown in Figure 10). These findings underscore a close agreement between the obtained charge magnitudes in the simulation and laboratory studies.

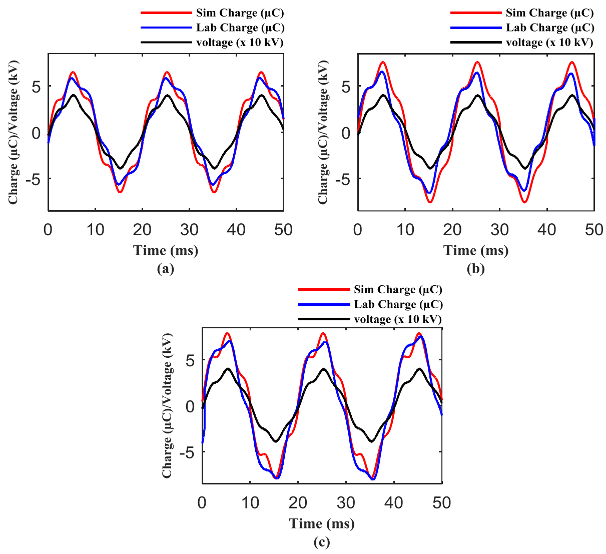

Fig. 8: Charge waveforms for different pollution conductivities: (a) 20 μS/cm, (b) 150 μS/cm, (c) 340 μS/cm.

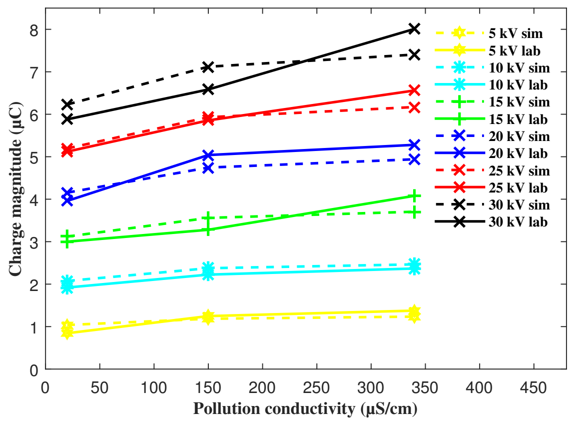

Fig. 9: Charge magnitude versus pollution conductivity for different applied voltages.

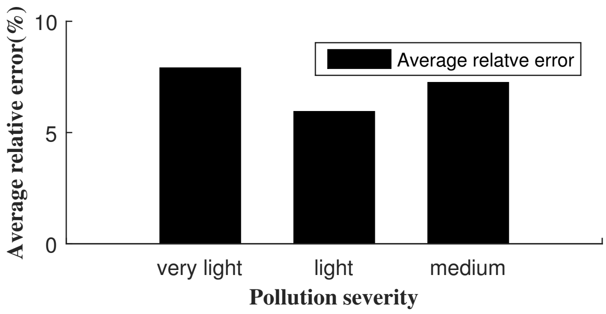

Fig. 10: Average relative error versus pollution severity.

B. Non-Uniform Pollution Case

Fig. 11 presents the simulation and experimental results of charge waveforms under a 30 kV applied voltage for the clean surface and various pollution layer widths (5, 10, 15, and 20 cm). Notably, a significant similarity is observed in terms of the charge waveforms between the simulation and experimental

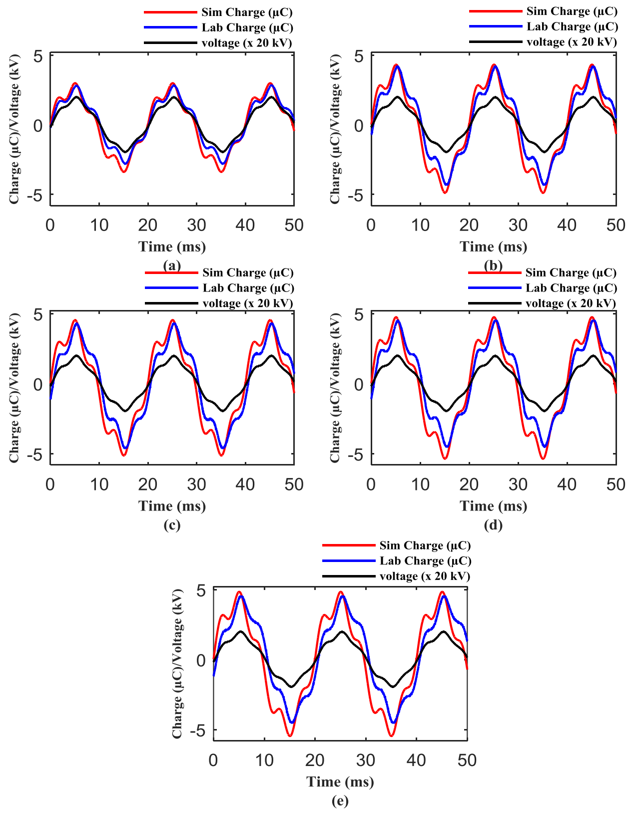

Fig. 11: Charge waveforms for different pollution layer widths (a) clean, (b) 05 cm, (c) 10 cm, (d) 15 cm, (e) 20 cm.

results. The presence of the dry band effect leads to the charge and voltage waveforms being almost in phase, indicating the dominant capacitive behavior within the insulating system for all considered pollution widths.

Fig. 12 illustrates the results of charge magnitudes versus pollution layer widths under different applied voltages. From this figure, the results demonstrate a notable increase in charge magnitudes as the pollution layer widths expand, slightly for small voltages and in a significant way for higher voltages. It is possible that this increase is attributed to the initial occurrence of arcing discharges, wherein it contributes, in some way, to the overall charge quantity. The increase in pollution layer width leads to a decrease in arcing voltages, as shown in Table IV, which presents the values of arcing voltages for the pollution layer widths adopted in this study.

It is evident that the charge magnitudes obtained through simulations closely align with those derived from laboratory experiments, with average relative errors of 8.11 %, 6.87 %, 6.41 %, 4.75 %, 3.57 %, and 5.01 % for the clean insulator and pollution widths of 5 cm, 10 cm, 15 cm, 20 cm, and 25 cm, respectively (Figure 13).

To explain why variations in the pollution layer width do not significantly influence the charge variation, it is essential to understand the leakage current circulation between HV and ground ends. This can be illustrated and well explained by current density streamlines, as the leakage current is closely related to the current density. Fig. 14 illustrates the current density as a function of pollution layer width. For a clean insulator, the current density streamlines are concentrated in the

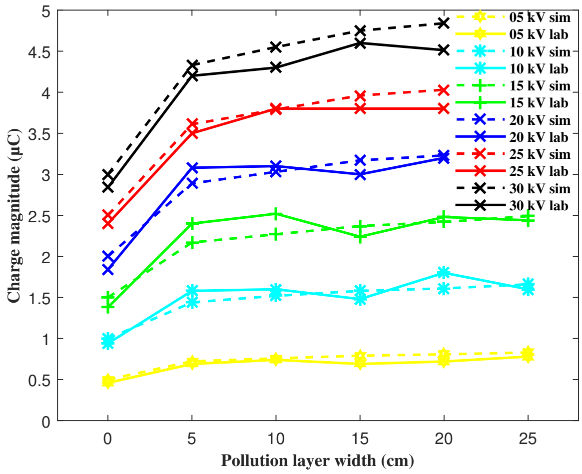

Fig. 12: Charge magnitude versus pollution layer width for different applied voltages.

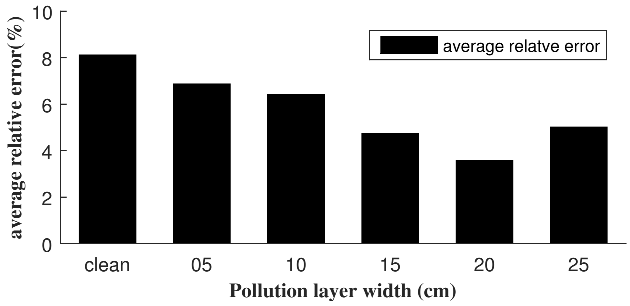

Fig. 13: Average relative error versus pollution layer widths.

radial zone defined by the cap and pin, composed of cement and glass materials (highlighted in red in Fig. 14(a)). However, for all pollution layer widths, a high concentration of current density streamlines is observed through the glass near the end of the cap (black circles in Fig. 14(b) to (f)). Under polluted conditions, the glass thickness has a significantly greater impact on the current density than the surrounding air. This is due to the higher relative permittivity of glass compared to air.

Simulations enable comprehensive analysis of various electrical characteristics, including leakage current. For example, in [24], we investigated the electrical performance of cap-pin and composite insulators used in 400 kV transmission lines. Utilizing the simulation's flexibility, we independently evaluated leakage current through air and insulator materials. Studying the distribution of electric charge takes us a step ahead in understanding additional electrical behaviors. Understanding aspects such as the electric field has assisted us in optimizing the corona ring design [25], thereby enhancing the performance of the cap and pin insulator.

Table. IV

ARCING VOLTAGES VERSUS NON-UNIFORM POLLUTION WIDTH

Pollution width (cm)	0	5	10	15	20	25
Arcing voltage (kV)	48	26	22	18	17	14

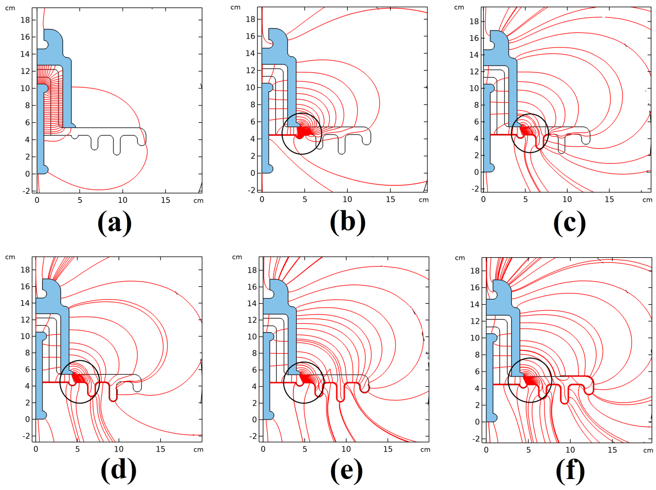

Fig. 14: Current density in function of pollution layer width: (a) clean, (b) 05 cm, (c) 10 cm, (d) 15 cm, (e) 20 cm, and (f) 25 cm.

VI. Conclusion

This research paper focuses on investigating the behavior of electric charges in cap-pin insulator under both uniform and non-uniform pollution conditions. In the case of uniform pollution, different conductivities are selected to represent various pollution severities, including very light (20 μS/cm), light (150 μS/cm), and medium (340 μS/cm). For non-uniform pollution, the study considers different widths of the pollution layer with high conductivity set at 1050 μS/cm. The research employs a combination of simulation and experimental methods to explore these scenarios and gain insights into the location and polarities of the electric charges.

The main findings reveal that the surface charge density in the first zone remains stable, while in the second zone, it varies based on the severity and widths of pollution. Specifically, positive charges accumulate within a distance of 17 cm from the HV electrode in the case of uniform pollution over the second zone. Negative charges, on the other hand, accumulate along the remaining length. For non-uniform pollution over the second zone, positive charges accumulate along a 10 cm length starting from the HV electrode (or 5 cm in the case of a pollution width of 5 cm), while negative charges are confined within the first 2 cm near the ground end.

For both pollution conditions, experimental charge waveforms were recorded with applied voltage level of 30 kV. The results indicate that the magnitudes of the charges increase with the increase in pollution conductivity and also with the increase in pollution layer width. The simulation and laboratory results of the charge waveforms demonstrate good agreement for all the cases considered.

The charge magnitudes obtained from the simulation closely match the experimental results. In the case of uniform pollution, the average relative error is approximately 7.90 % for very light, 5.94 % for light, and 7.25 % for medium pollution severities. Regarding the non-uniform pollution case, the errors are approximately 8.11 % for a clean insulator, and 6.87 %, 6.41 %, 4.75 %, 3.57 %, and 5.01 % for pollution layer widths of 5 cm, 10 cm, 15 cm, 20 cm, and 25 cm, respectively.

Our work focused on understanding the volumetric and surface charge density, as well as the overall charge on glass insulators, which are influenced by factors like corrosion, temperature, and aging. Comparing simulations with experimental data verified our results and enhanced their interpretation. This methodology also opens new research avenues, such as optimization applications, potentially improving insulator performance.

References

[1] R. Salhi, A. Mekhaldi, M. Teguar and O. Kherif, "Corona Ring Improvement to Surface Electric Field Stress Mitigation of 400 kV Composite Insulator," in IEEE Transactions on Dielectrics and Electrical Insulation, vol. 31, no. 3, pp. 1509-1516, June 2024, DOI: 10.1109/TDEI.2023.3342772.

[2] C. Zhang, L. Wang, Z. Guan, and F. Zhang, "Pollution flashover performance of full-scale +- 800 kV converter station post insulators at high altitude area," *IEEE Trans. Dielectr. Electr. Insul.*, vol. 20, no. 3, pp. 717–726, Jun. 2013. DOI: 10.1109/TDEI.2013.6518940.

[3] D. Mussina, A. Irmanova, P. K. Jamwal and M. Bagheri, "Multi-Modal Data Fusion Using Deep Neural Network for Condition Monitoring of High Voltage Insulator," *in IEEE Access.*, vol. 8, pp. 184486-184496, Sept. 2020. DOI: 10.1109/ACCESS.2020.3027825.

[4] N. A. Othman, M. A. M. Piah, Z. Adzis, H. Ahmad, N. A. Ahmad, H. Kamarden, A. A. Suleiman, "Characterization of charge distribution on the high voltage glass insulator string," *Journal of Electrostatics.*, vol. 72, no. 4, pp. 315-321, Aug. 2014. DOI: 10.1016/j.elstat.2014.05.003.

[5] O. E. Gouda, M. M. F. Darwish, K. Mahmoud, M. Lehtonen and T. M. Elkhodragy, "Pollution Severity Monitoring of High Voltage Transmission Line Insulators Using Wireless Device Based on Leakage Current Bursts," *in IEEE Access.*, vol. 10, pp. 53713-53723, May. 2022. DOI: 10.1109/ACCESS.2022.3175515.

[6] J. Mahmoodi, M. Mirzaie and A. A. Shayegani-Akmal, "Surface charge distribution analysis of polymeric insulator under AC and DC voltage based on numerical and experimental tests," *International Journal of Electrical Power & Energy Systems.*, vol. 105, pp 283-296, Feb. 2019. DOI: 10.1016/j.ijepes.2018.08.006.

[7] N. A. Othman, M. A. M. Piah and Z. Adzis, "Charge distribution measurement of solid insulator materials: A review and new approach," *Renewable and Sustainable Energy Reviews.*, vol. 70, pp. 413-426, Apr. 2017. DOI: 10.1016/j.rser.2016.11.237.

[8] L. Yifan, L. Mingzhe, C. Bin, M. Hongwei and W. Liming, "Research on Influence of Charge Quantity of Particles on Contamination Accumulation Characteristics," *2018 IEEE Conference on Electrical Insulation and Dielectric Phenomena (CEIDP)*, Cancun, Mexico, 2018, pp. 211-214, DOI: 10.1109/CEIDP.2018.8544798.

[9] S. Das, J. C. Pandey and N. Gupta, "Space charge diagnostics in aged polymeric insulation," *2013 IEEE 1st International Conference on Condition Assessment Techniques in Electrical Systems (CATCON)*, Kolkata, India, 2013, pp. 395-398, DOI: 10.1109/CATCON.2013.6737535.

[10] J. -M. Löwe and V. Hinrichsen, "Experimental Investigation of the Influence of Electric Charge on the Behavior of Water Droplets in Electric Fields," *2019 IEEE 20th International Conference on Dielectric Liquids (ICDL)*, Roma, Italy, 2019, pp. 1-6, DOI: 10.1109/ICDL.2019.8796707.

[11] D. Yang, F. Yin, H. Mei, L. Wang and C. Guo, "In-Situ Monitoring of Electrolytic Corrosion on the Caps of HVDC Insulators," *in IEEE Sensors Journal.*, vol. 18, no. 20, pp. 8569-8577, Oct. 2018, DOI: 10.1109/JSEN.2018.2865521.

[12] M. Teguar, D. Namane and A. Mekhaldi, “Influence of the thickness and the nature of HVAC insulator model on the flashover voltage and the leakage current," *2013 IEEE International Conference on Solid Dielectrics (ICSD)*, Bologna, Italy, 2013, pp. 186-189, doi: 10.1109/ICSD.2013.6619796.

[13] J. Mahmoodi, M. Mirzaie and A. A. Shayegani-Akmal, “Surface charges on silicon rubber (SiR) insulator and their effect on potential and electric field distribution," *Electr Eng.*, vol. 100, pp. 2695–2705. 2018. DOI: 10.1007/s00202-018-0740-6.

[14] D. D. Dimitriadou, G. K. Soulinaris, P. T. Tsarabaris, C. G. Karagiannopoulos, and P. D. Bourkas, “External Partial Discharges of Pertinax in Air," *Proceedings of the Eighth IASTED International Conference POWER AND ENERGY SYSTEMS (EuroPES 2008)* Corfu, Greece June 23-25, 2008, pp. 313-317.

[15] D. Namane (Ph.D. Dissertation), “Modélisations expérimentale et numérique d’isolateurs HT sous tension alternative 50Hz," Electrical Engineering Department, Electrotechnical Research Laboratory. Alger, Ecole Nationale Polytechnique. Algeria, 2011. D002311

[16] IEC, TS. “60815-1. Selection and Dimensioning of High-voltage Insulators Intended for Use in Polluted Conditions-Part 1: Definitions, Information and General Principles." International Electrotechnical Commission: Worcester, MA, USA (2008). IEC TS 60815-1:2008

[17] IEC Standard 60507,“Artificial pollution tests on high-voltage ceramic and glass insulators to be used on a.c. systems." 2013. IEC 60507:2013.

[18] R. Salhi, A. Mekhaldi, M. Teguar, O. Kherif and M. El Amine Slama, “Cap-Pin glass insulator simulation and leakage current waveform extraction," *2022 2nd International Conference on Advanced Electrical Engineering (ICAEE)*, Constantine, Algeria, 2022, pp. 1-4, DOI: 10.1109/ICAEE53772.2022.9961979.

[19] R. Salhi, A. Mekhaldi, M. Teguar and O. Kherif, “Quantitative Analysis of Electric Charge Distribution on Cap-Pin Insulator Using COMSOL Multiphysics," *Fourth International Conference on Technological Advances in Electrical Engineering (ICTAEE’23)*, Skikda, Algeria, May 2023, pp. 576-579.

[20] A. A. Salem *et al.*, “Pollution Flashover Under Different Contamination Profiles on High Voltage Insulator: Numerical and Experiment Investigation," *IEEE Access*, vol. 9, pp. 37800-37812, Mar. 2021. DOI: 10.1109/ACCESS.2021.3063201.

[21] J. Araya, J. Montaña, and R. Schurch, “Electric Field Distribution and Leakage Currents in Glass Insulator Under Different Altitudes and Pollutions Conditions using FEM Simulations," *in IEEE Latin America Transactions*, vol. 19, no. 8, pp. 1278-1285, Aug. 2021. DOI: 10.1109/TLA.2021.9475858.

[22] M. E. -A. Slama, A. Beroual and H. Hadi, “Influence of the linear non-uniformity of pollution layer on the insulator flashover under impulse voltage - estimation of the effective pollution thickness," *in IEEE Transactions on Dielectrics and Electrical Insulation*, vol. 18, no. 2, pp. 384-392, Apr 2011. DOI: 10.1109/TDEI.2011.5739441.

[23] M. Imran Mousa, Z. Abdul-Malek, Z. Imran Mousa, “Aging Detection of Glass Disc Insulator by Using Infrared Camera," *Indonesian Journal of Electrical Engineering and Computer Science.*, vol. 6, pp. 520-527. 2017. DOI: 10.11591/ijeecs.v6.i3.pp520-527.

[24] R. Salhi, O. Kherif, A. Mekhaldi and M. Teguar, “ Electrical Performance of 400-kV Cap-Pin and Composite String Insulators. COMSOL Multiphysics Simulations," *2023 the 23rd International Symposium on High Voltage Engineering (ISH)*, Glasgow, UK, 2023, pp. 260-264, DOI: 10.1049/icp.2024.0483.

[25] R. Salhi, A. Mekhaldi, M. Teguar and O. Kherif, “Optimizing corona ring design for 400 kV cap-pin string insulator to minimize surface electric field under various surface conditions," *2023 International Conference on Electrical Engineering and Advanced Technology (ICEEAT)*, Batna, Algeria, 2023, pp. 1-5, DOI: 10.1109/ICEEAT60471.2023.10426163.

Rabie Salhi received his PhD in Electrical Engineering from Ecole Nationale Polytechnique in July 2024.

Abdelouahab Mekhaldi received the degree of Engineer in 1984 in electrical engineering, the MSc degree in 1990 and a Ph.D. in high voltage engineering in 1999 from Ecole Nationale Polytechnique (ENP) of Algiers. He is currently a Professor at ENP. His main research areas are in discharge phenomena, outdoor insulators pollution, polymeric cables insulation, lightning, artificial intelligence application in high voltage insulation diagnosis and electric field calculation.

Madjid Teguar received the degree in electrical engineering, the master’s degree, and the Ph.D. degree in high voltage engineering from the École Nationale Polytechnique (ENP) of Algiers, in 1990, 1993, and 2003, respectively. He is currently a Professor of Electrical Engineering with ENP. His research interests include insulation systems, insulation coordination, earthing of electrical power systems, and polymeric cables insulation.

Omar Kherif received a M.Eng. and Ph.D. degrees in electrical engineering from the Ecole Nationale Polytechnique (ENP) in 2015 and 2019, respectively. He was a mathematical-analysis teacher with ENP from 2016 to 2018. He was also researcher with the Laboratoire de Recherche en Electrotechnique (LRE) of the ENP, where he co-supervised several M.S. theses. He is currently a KTP Associate with Cardiff University and a Technical Consultant with Kingsmill Industries Ltd (UK). His main interests are in high voltage engineering, electromagnetic transients, earthing and power system protection. Dr Kherif is a member of IEEE and some of IEEE societies since 2017

Methylene Blue Adsorption Kinetics Investigation by Coconut Shell Activated Carbon Adsorbent Using Fractional Power, Avrami and Bangham Models

Abdulghaffaar Assayyidi Yusuf, Abdulhalim Musa Abubakar, Muhammad Abdulrazak, Kamran Khan, and G. Rajasekar

Abstract−Methylene blue is not easily biodegradable, and its persistence in water can contribute to long-term contamination if not properly treated. Numerous adsorption kinetic study successes were achieved utilizing activated carbons of coconut shell, especially the Pseudo-First and Pseudo-Second order models with little/no regards to the unique behavior described by the Avrami, Bangham and the Fractional Power kinetic models. Herein, the parameters in those models, such as k_{AV} & n_{AV}; K_f & α and; k & v, respectively, were determined to describe the sorption mechanism. Avrami model fitting results in $n_{AV} = 0.72537$ (< 1), suggesting a complex adsorption process which does not follow the first-order kinetic; but a k_{AV} of 0.24926 obtained, signifies a positive adsorption rate. A '$v < 1$' obtained deviates from the first-order but shows that the Fractional Power model best described the Coconut Shell- Activated Carbon Methylene blue bio-sorption process at constant adsorption capacity of 15937.8 mg/g. Findings show that Bangham kinetic model does not fit the experimental data for MB sorption from aqueous solution. MB exposure issues like gastrointestinal discomfort, skin and eye irritation, and imbalances in the populations of various species in aquatic ecosystems due to impacts on their growth, reproduction and survival, may be solved using a very effective adsorbent, such as the CS-AC used here.

***Keywords*− Methylene blue dye, Coconut shell, Avrami model, Bangham model, Fractional power kinetic**

NOMENCLATURE

FP	Fractional Power.
RSM	Response Surface Methodology.
MB	Methylene Blue.
CS	Coconut Shell.
AC	Activated Carbon.

I. INTRODUCTION

In practice, researchers often choose a kinetic model based on the observed behavior of the bio-sorption process and validate the selection by comparing model predictions to experimental data. Fractional Power (FP), Avrami, and Bangham bio-sorption kinetic models are three distinct approaches used to describe the kinetics of bio-sorption processes. Amongst them, a sigmoidal shape, making it suitable for bio-sorption processes with a gradual decrease in the adsorption rate over time, characterizes Bangham model. Avrami model incorporates an exponential term in addition to a power-law term, offering versatility in capturing a variety of bio-sorption mechanisms (including surface adsorption and diffusion-controlled processes) [1], [2]. On the other hand, the FP model uses a power-law relationship with a fractional exponent [3], providing flexibility in describing kinetics with non-integer reaction orders. The appropriateness of a model depends on the specific characteristics of the bio-sorption system under investigation. While isotherm studies focus on equilibrium conditions [4]–[8], describing the distribution of sorbate between the bio-sorbent and the solution at a specific time, kinetic studies visualize the rate at which sorption occurs over time. Kinetic studies are often conducted first to understand the fundamental behavior of the bio-sorption process. Once key parameters are identified, response surface methodology (RSM) can be employed for systematic optimization [9], [10]. In some cases, kinetic information can be integrated into the optimization process. For example, kinetic constants derived from experimental data can be used as input parameters in the optimization model. Now, majority of the existing kinetics of methylene blue (MB) removal from wastewater using coconut shell (CS) activated carbon (AC) as adsorbent, as an example, had already been studied. Backed only with an isotherm study, Olafadehan et al. (2012) demonstrated the effectiveness of CS-AC in treating brewery wastewater.

CS-AC is a low-cost adsorbent for wastewater purification [12]–[15], also studied in a fixed bed column [16]–[18] and sometimes, a two-stage adsorber (Wong et al., 2022). MB, a synthetic dye with a distinctive blue color, is used in various

Manuscript received February 15, 2024; revised June 28, 2024.

A. A. Yusuf is with Department of Sciences, National Institute of Construction Technology and Management (NICTM) Uromi, Ugboha Road, Edo State, NIGERIA (abdulghaffaaro@gmail.com)

A. M. Abubakar is with Department of Chemical Engineering, Faculty of Engineering, Modibbo Adama University, P.M.B. 2076, Yola, Adamawa State, NIGERIA (abdulhalim@mau.edu.ng)

M. Abdulrazak is with Department of Agricultural Technology, Federal College of Horticulture Dadin Kowa, Gombe State, NIGERIA (sherifokene@gmiail.com)

K. Khan is with Department of Petroleum and Gas Engineering, BUITEMS QUETTA, Balochistan, PAKISTAN (kk699@uowmail.edu.au)

G. Rajasekar is with Plant Pathology, Adhiyamaan College of Agriculture and Research, Tamilnadu, INDIA (rajasekar.raj999@gmail.com)

Digital Object Identifier (DOI): 10.53907/enpesj.v4i1.259

industrial applications, including textile dyeing [20]–[22], laboratory testing, and as a stain in medical and biological procedures. While it serves its intended purposes, the presence of MB in water can be a cause for concern due to several reasons, including its toxicity, health risk and the loss of water aesthetic quality. Adsorption [23], [24], chemical precipitation, advanced oxidation processes and biological treatment are major MB removal techniques. Thus, variants of the coconut parts or its derivative have also been applied in several sorption processes involving CS. As such variants or derivative, one has shell [25], charcoal [26]-[27], choir [28]–[31], fiber (Al-Aoh et al., 2016; Zhang et al., 2018), AC [34]-[35], dreg [36], leaves [37]–[39], tree bark [40], spent grated coconut [41], coating/modifications [42]–[45], hydrochar [46], biochar [47] and additives [48]- [49]. In addition, the removal of other dye types from water had been examined using CS [50], [51].

Study conducted by Shah & Parmar (2018) show that AC derived from CS has 5.5 pH, 2% moisture content, 10.7% ash content, 0.5 g/cm3 bulk density, 1227 mg/g iodine number, 249 mg/g MB number and 936 m^2/g specific surface area. Also, optimization of operating variables for the production of AC from CS was investigated by Liang et al. (2020), reporting a lesser iodine value of 698.37 mg/g. None among published articles between 2000-2024 employed the FP, Bangham and the Avrami kinetic model to explain the adsorption mechanism of MB dye by CS-AC. However, Pseudo First order, Pseudo Second order [30], [38], [54]–[56], Weber & Morris intra-particle diffusion [57]–[60], Natarajan & Khalaf, Bhattachara & Venkobachar [61], Bangham [62], [63], Mekay et al. and the liquid film diffusion [62] kinetic had been studied for this particular adsorbent and adsorbate.

This study wishes to estimate the kinetic parameters from the three models described, to study the behavior of the adsorbent at 10, 20, 30, 40, 50 and 60 mins contact time. Previously, Khuluk et al. (2019) carried similar study at 40, 60 and 80 min equilibrium time, but studied the isotherm only. Abdullah et al. (2017), Ismail et al. (2015) and Foo & Hameed (2012) studied the effect of acid and/or base treatment to MB sorption using CS-AC and; Yasin et al. (2007) and Gimba et al. (2000) investigated the adsorption of MB unto potassium hydroxide treated CS-AC and iron and calcium chloride activated powdered CS-AC, respectively.

Thermodynamic studies previously conducted [70], highlights the energy requirements during MB adsorption using variety of CS parts. Though, the present study is only interested in MB removal from aqueous solution, it suffices and will serve as a guide towards carrying out similar studies on plastic industry, tannery, cosmetic industry, photographic, laboratory, printing, paper, pharmaceutical, dye manufacturing and leather industry wastewaters, which may contain the dye. Thus, the order and mechanism of the adsorption process may be understood, contribution of the 3 different kinetic models to the overall adsorption behavior is assessed and process conditions for efficient removal of MB from aqueous solutions can be optimized.

II. METHOD

A. Process Condition

Procedure for the adsorption of MB unto CS-AC were set, as shown in Table 1. Method followed in the preparation of AC from CS in this study, was partly in accordance with Shaheed et al. (2015), Das et al. (2015), Sulyman & Sulyman (2018) and Rangari & Chavan (2017).

Table 1: Bio-sorption Process Conditions

Condition	Measurement
CS-AC Dosage	0.2g
Contact Time	10-60 min
Temperature	303 K (30°C)
Initial MB Concentration	100 mg/L
Agitation Speed	250 rpm
Volume of Solution	50 L
AC Particle Size	63-125μm

Activating agent used was sodium hydroxide (NaOH), as described in Mercileen et al. (2023), Cazetta et al. (2011) and Chong & Tam (2020). During MB adsorption by CS-AC, Wong et al. (2013) utilized a particle size of 150 μm larger than the size employed in this study.

B. Model Fitting

Constant parameters in Bangham model (Equation 1) [63], Avrami (Equations 2 & 3) [78], [79] and the FP kinetic model (Equations 4 & 5) [2] were determined using experimental kinetic variables in Table 2.

$$Log \log\left(\frac{C_i}{C_i - q_t\, M}\right) = \log\left(\frac{K_f\, M}{2.303\, V}\right) + \alpha \log t \qquad (1)$$

$$q_t = q_e[1 - \exp(-k_{AV} t^{n_{AV}})] \qquad (2)$$

$$\ln\left[\ln\left(\frac{q_e}{q_e - q_t}\right)\right] = n_{AV} \ln k_{AV} + n_{AV} \ln t \qquad (3)$$

$$q_t = kt^v \qquad (4)$$

$$\log q_t = \log k + v \log t \qquad (5)$$

Where, C_i = initial concentration of dye solution (mg/L), V = volume of dye solution (L), M = mass of CS adsorbent (g), q_t = quantity of dye adsorbent at time, t (mg/g), α (< 1) and K_f = constants obtainable from slope and intercept of Equation 1, respectively. k_{AV} = Avrami adsorption kinetic constant ($min^{-n_{AV}}$), n_{AV} = Avrami model exponent of time related to the change in mechanism of adsorbent. $k =$ FP rate constant, and v = constant that is usually less than unity if adsorption kinetic data fits well into power function model. Unknown parameters were determined by plotting relevant variable/term data in Table 2 based on the linearized form of the Bangham (Equation 1), Avrami (Equation 3) and the FP (or Equation 5) model. However, before any other step, the maximum adsorption capacity of CS-AC for MB, q_e (mg/g) was determined by running a user-defined regression analysis in Origin Pro 2018 using Equation 2 (a nonlinear model). Initial guesses for q_e, k_{AV} and n_{AV} was made to allow the statistical analysis software estimate their new set of value based on good fit or high coefficient of determination (R^2) of the predicted and experimental q_t vs. contact time plot. Linear version of the depiction is re-illustrated using Equation 3 and comparison was made as to the best kinetic parameter estimated between nonlinear method of solution and graphical/linear results.

Thus, a plot of $\ln\left[\ln\left(\frac{q_e}{q_e - q_t}\right)\right]$ againt $\ln t$ was carried out, taken/using q_e value obtained from regression analysis. Relevant graphical representation was also produced to analyze the Bangham and FP model. Essentially, q_t was calculated using Equation 6 [80]–[83].

$$q_t = \frac{(C_i - C_e)V}{M} \qquad (6)$$

Where, M, C_i, C_e and V are as defined earlier.

Table 2: Axis Data for Parameter Determination

t (min)	C_e (mg/L)	q_t (mg/g)	q_t (mg/g)	ln t	$\ln\left[\ln\left(\frac{q_e}{q_e - q_t}\right)\right]$		log t
		Expt.	Prdct.		Expt.	Prdct.	
10	68.52	7870	11699.01	2.3025851	-0.38447	0.280967	3.895975
20	41.61	14597.5	14153.55	2.9957323	0.906554	0.783756	4.164278
30	38.3	15425	15093.93	3.4011974	1.234452	1.077868	4.188225
40	38.02	15495	15511.09	3.6888795	1.276271	1.286544	4.190192
50	37.82	15545	15711.93	3.912023	1.309159	1.448405	4.191591
60	36.72	15820	15814.08	4.0943446	1.590695	1.580656	4.199206
t (min)	**log t**	**$q_t \times 10^3$ (mg/g)**		**$\log q_t$**	**$Log \log\left(\frac{C_i}{C_i - q_t M}\right)$**		
10	1	7.87		3.895975	−2.16177		
20	1.30103	14.5975		4.164279	−1.89049		
30	1.47712	15.425		4.188225	−1.86617		
40	1.60206	15.495		4.190192	−1.86418		
50	1.69897	15.545		4.191591	−1.86275		
60	1.77815	15.82		4.199207	−1.85502		

III. RESULTS AND DISCUSSION

A. Avrami Model Parameters

Figure 1a was obtained as a result of defining the Avrami kinetic model as a user-defined model in Origin Pro by selecting the Orthogonal Distance Regression (Pro) iteration algorithm. For the linearized plot (Figure 1b), q_e must be known and is cautiously taken from nonlinear regression conducted.

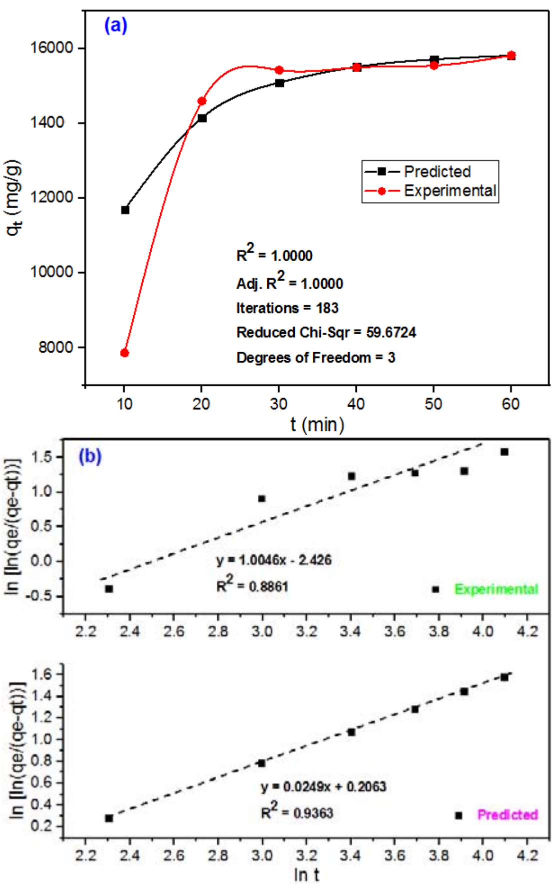

Figure 1: Avrami Kinetic Parameter from (a) Nonlinear Regression and (b) Graphical Method

Normally, when $\ln\left[\ln\left(\frac{q_e}{q_e-q_t}\right)\right]$ is plotted against $\ln t$ for the Avrami biosorption kinetic model, a straight line with a slope equal to the Avrami exponent 'n_{AV}' and a y-intercept equal to $\ln t$ is obtained [84]. Similarly, using the experimental and predicted $\ln\left[\ln\left(\frac{q_e}{q_e-q_t}\right)\right]$ data, new sets of k_{AV} and n_{AV} can be calculated from straight-line equations shown in Figure 1b. The Avrami parameter values for the adsorption of MB by CS-AC adsorbent is shown in Table 3.

Table 3: Avrami MB Adsorption Kinetic Parameters

Parameter	Nonlinear Method	Graphical Method	
		Predicted Data	Experimental Data
q_e (mg/g)	15937.83593	15937.83593	15937.83593
k_{AV} (*)	0.24926	3964.522	0.089377
n_{AV}	0.72537	0.0249	1.0046
R^2	1.0000	0.9363	0.8861

**Unit depends on the unit of time*

As expected, predicted $\ln\left[\ln\left(\frac{q_e}{q_e-q_t}\right)\right]$ values vs. $\ln t$ gives an almost perfect fit ($R^2 = 0.9363$) than the experimental data with $R^2 = 0.8861$, for similar actual and predicted $q_e = 15937.84$ mg/g. Often, the graphical method of finding kinetic parameters utilizes experimental x- and y-axis data and not the predicted ones. As such, Avrami parameters obtained following the nonlinear and experimental data are close. Value of $k_{AV} = 3964.522$ obtained from the use of predicted data graphical method is too high and odd, even though the fit is better. It does not satisfy the corresponding value of $n_{AV} = 0.0249$ obtained, because normally, if $n_{AV} = 0$ or $\cong 0$, the plot of $\ln\left[\ln\left(\frac{q_e}{q_e-q_t}\right)\right]$ against $\ln t$ will be a horizontal line with a slope of zero. Therefore, natural logarithm of the ratio $\frac{q_e}{q_e-q_t}$ remains constant with time. This suggests that the biosorption process follows a zero-order reaction, where the rate of the reaction is independent of the concentration of the MB. The adsorption occurs at a constant rate until equilibrium is reached. This observation strikes out estimates form the predicted data obtained graphically, leaving the experimental graphical result and the nonlinear regression estimates. Researchers will find the R 'PUPAK Package' containing model fitting functions for linear and non-linear adsorption kinetic and diffusion models developed by Magalong et al. (2022), a better and easier way of predicting bio-sorption kinetic parameters in the future. Since the Orthogonal Distance Regression algorithm gives a higher R^2 value of unity, implying a better fit compared to the experimental graphical parameters in Table 3, it may be adopted as the most accurate Avrami parameter values for MB CS-AC bio-sorption. If $n_{AV} = 1$ in the Avrami model, the plot of $\ln\left[\ln\left(\frac{q_e}{q_e - q_t}\right)\right]$ against $\ln t$ will be a straight line with a slope $= k_{AV}$, and this suggests first-order kinetics in the Avrami model, almost in agreement with $n_{AV} = 1.0046$ obtained empirically. But $n_{AV} < 1$ for this study, suggests a complex adsorption process that does not strictly follow first-order kinetics, as obtained via regression. When $n_{AV} = 2$, it is a second-order reaction. Rate constant ($k_{AV} = 0.24926\, min^{-n_{AV}}$) reflects the speed of the MB adsorption process, where a positive value, indicates a positive rate of adsorption. In a study conducted by Kuete et al. (2020), $k_{AV} = 0.213\, min^{-1}$ closer to this study and $n_{AV} = 0.562$ was realized during thymol blue adsorption by Garcinia cola nut shells.

B. Fractional Power Kinetic Parameters

k and v FP kinetic parameters, as determined using the nonlinear FP model (or Equation 4) and the linearized model (or Equation 5) also explains the behaviour of the CS-AC biosorbent.

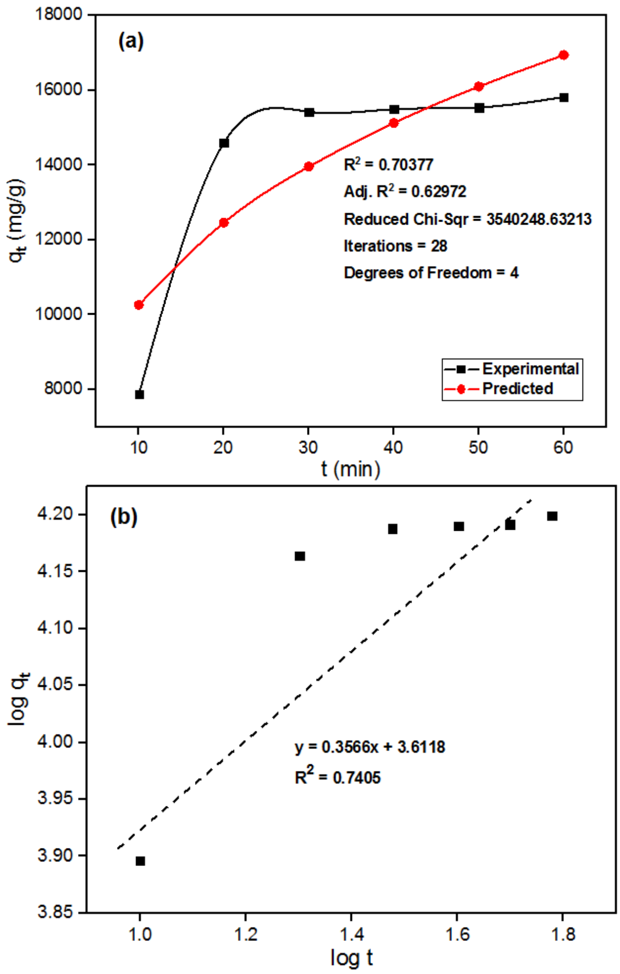

Figure 2: FP Model Parameter Determination by (a) Regression and (b) Graphical Method

The fact that 'v' < 1 [86], implies that the adsorption kinetic data determined via the two approaches in Table 4, fits well into the power function model. However, since R^2 is higher, as observed under the graphical technique (0.7405), the corresponding k and v values at which it occurs is the most accurate prediction.

Table 4: Estimated FP Model Parameters

Parameter	Nonlinear Technique	Graphical Technique
k (mg/g min)	5390.83675	4090.722
v	0.27972	0.3566
R^2	0.70377	0.7405

Important derivations from this analysis are as follows: (1) the adsorption of MB on CS-AV follows a FP kinetic model, indicating a deviation from classical first-order kinetics, (2) adsorption rate (k) is relatively high, suggesting a rapid adsorption process and (3) the model moderately fits the experimental data (R^2 values around 0.7). Generally, a value of v between 0 and 1 suggests fractional-order kinetics, as obtained in Kuete et al. (2020) and Mozaffari et al. (2020). The higher the value of v, the more the kinetics deviate from classical first-order kinetics. Here, both techniques provide similar values for v, indicating a fractional-order adsorption process. In addition, a higher k value points to faster adsorption rate. In that case, the following assumptions of the FP model are satisfied:

(1) A homogeneous system where the concentration of MB is uniform throughout the CS-AC.
(2) A single-component adsorption based on the assumption that only MB is involved in the process.
(3) A constant temperature (in this case, 30℃) throughout the bio-sorption process,
(4) No external mass transfer resistance from the bulk solution to the CS-AC surface.
(5) The model assumes well-defined initial conditions (Table 1) for the process.
(6) A negligible effect between MB molecules on the CS-AC surface.

C. Bangham Kinetic Parameters

It is discovered that q_t data in Table 2 are too large to give a meaningful value of $Log \log\left(\frac{C_i}{C_i - q_t M}\right)$. Hence, $q_t \times 10^3$ was the re-scaled value used to estimate the Bangham model kinetic parameters. So, a plot of $Log \log\left(\frac{C_i}{C_i - q_t M}\right)$ against $\log t$ is shown in Figure 3.

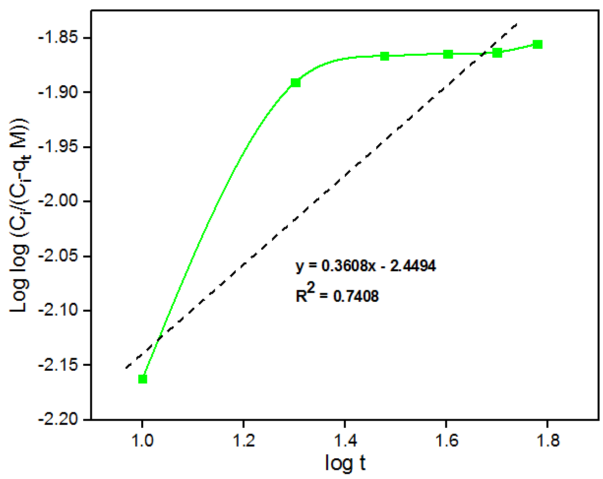

Figure 3: Bangham Kinetic Plot for MB Biosorption via CS-AC

Even so, the plot of $Log \log\left(\frac{C_i}{C_i - q_t M}\right)$ against $\log t$ is not linear as expected, showing that the Bangham model is not an appropriate description of the adsorption kinetics in this system. Kavitha & Namasivayam (2007) obtained a perfect linear plot at 35℃ using coconut coir as adsorbent to remove MB, as also realized in Inyinbor et al. (2016) at $R^2 > 0.9$ using a different adsorbate-adsorbent system. The model parameters in question (Table 5) were then computed from slopes and intercepts of Equation 1 plotted.

Table 5: Bangham Kinetic Parameters for MB Sorption using CS

Parameter	Value
K_f	2.045662
α	0.3608
R^2	0.7408

Rate constant, K_f associated with the Bangham kinetic model is dependent on the order of the reaction while α represent the fractional attainment of equilibrium or the proportionality between the rate of adsorption and the driving force. Specific range of K_f values considered "high" or "low" is context-dependent and can vary for different adsorbate-adsorbent systems. Researchers may compare K_f values with those obtained for other adsorbate-adsorbent systems or under different conditions to assess relative adsorption rates; such as in Kavitha & Namasivayam (2007). Prajapati & Mondal (2020) obtained $K_f = 2.35$ and $\alpha = 0.74$ at 100 mg/L MB C_i sorbed by modified CS. An $\alpha = 0$ can be interpreted as the initial stage of adsorption where the process has not yet reached equilibrium. Values within the range: $0 < \alpha < 1$ may suggest that the adsorption process is reaching equilibrium, and the dimensionless $\alpha = 0.3608$ represents the fraction of equilibrium attained. And lastly, $\alpha = 1$ indicate complete attainment of equilibrium. R^2 measures how well the experimental data fits the Bangham kinetic model and an R^2 of 0.7408 infer a reasonable fit. Overall, the occurrence of undefined logarithmic terms can suggest that the model fit may not be appropriate for the entire adsorption process and the $q_t \times 10^3$ values resulting in Figure 3 are just exploratory. That is, the Bangham assumption that the rate of adsorption is directly proportional to the number of available adsorption sites on the adsorbent material or first-order kinetics is not satisfied. Other assumptions similar with '1' and '3' in FP model is also in agreement. In addition, the model assumes that the rate of adsorption remains constant throughout the adsorption process. This is a simplification, and in reality, the adsorption rate might change as the CS-AC bio-sorbent becomes saturated.

IV. Conclusion

Moderate success had been achieved in finding the best kinetic model amongst Avrami, FP and Bangham models, that describes the adsorption of MB from aqueous solution using CS-AC. For thorough and accurate representation of the reaction kinetics, reaction order from Bangham (α) and Avrami model (n_{AV}) were determined in the process via nonlinear regression or graphical method, as appropriate. It was discovered that very large q_t obtained in this study is not supported by the Bangham kinetic model and when it was re-scaled for ease of interpretation, an α value of 0.3608 described MB CS-AC system as an adsorption process approaching equilibrium. In this study, FP best describe the sorption of MB, favored by $k = 4090.722$ mg/g min, $v = 0.3566$ and $R^2 = 0.7405$. The Avrami nonlinear parameter estimate also suggest that the empirical data fits the model prediction. The analysis result almost abides by the assumptions of both FP and Avrami models. To know whether the bio-sorption is pore diffusion dependent at the particle size range (63-125μm) exploited, the intra particle diffusion kinetic model may be used. Elovich, Boyd and the general order biosorption kinetics is still not investigated for MB removal using CS adsorbent.

References

[1] J. R. Magalong, J. DelaCruz, J. Bumatay, and C. Deocaris, "Parameter estimation, and plot visualization of adsorption kinetic models: Package 'PUPAK.'" pp. 1–30, 2022, [Online]. Available: https://cran.r-project.org/web/packages/PUPAK/PUPAK.pdf.

[2] O. A. Olafadehan, V. E. Bello, K. O. Amoo, and A. M. Bello, "Isotherms, kinetic and thermodynamic studies of methylene blue adsorption on chitosan flakes derived from African giant snail shell," African J. Environ. Sci. Technol., vol. 16, no. 1, pp. 37–70, 2022, doi: 10.5897/AJEST2021.3065.

[3] A. R. Netzahuatl-Muñoz, M. del C. Cristiani-Urbina, and E. Cristiani-Urbina, "Chromium biosorption from Cr(VI) aqueous solutions by Cupressus lusitanica Bark: Kinetics, equilibrium and thermodynamic studies," PLoS One, vol. 10, no. 9, pp. 1–23, 2015, doi: 10.1371/journal.pone.0137086.

[4] Amrutha, G. Jeppu, C. R. Girish, B. Prabhu, and K. Mayer, "Multi-component adsorption isotherms: Review and modeling studies," Environ. Process., vol. 10, no. 38, pp. 1–52, 2023, doi: 10.1007/s40710-023-00631-0.

[5] N. Ayawei, A. N. Ebelegi, and D. Wankasi, "Modelling and interpretation of adsorption isotherms," J. Chem., vol. 2017, no. 3039817, pp. 1–12, 2017, doi: 10.1155/2017/3039817.

[6] D. P. Samal, "Characterization and study of adsorption of methylene blue dye using activated carbon," Bachelor of Technology (Chemical Engineering)-National Institute of Technology (NIT), Rourkela, 2014.

[7] F. O. Okeola and E. O. Odebunmi, "Comparison of Freundlich and Langmuir isotherms for adsorption of methylene blue by agrowaste derived activated carbon," Adv. Environ. Biol., p. 329+, 2010, [Online]. Available: link.gale.com/apps/doc/A252944760/AONE?u=anon~1e5d5ac0&sid=googleScholar&xid=a88a7c3d.

[8] F. O. Okeola and E. Odebunmi, "Freundlich and Langmuir isotherms parameters for adsorption of methylene blue by activated carbon derived from agrowastes," Adv. Nat. Appl. Sci., vol. 4, no. 3, pp. 281–288, 2010, [Online]. Available: https://www.researchgate.net/publication/283774009.

[9] I. A. W. Tan, A. L. Ahmad, and B. H. Hameed, "Optimization of preparation conditions for activated carbons from coconut husk using response surface methodology," Chem. Eng. J., vol. 137, pp. 462–470, 2008, doi: 10.1016/j.cej.2007.04.031.

[10] E. Danso-Boateng, M. Fitzsimmons, A. B. Ross, and T. Mariner, "Response surface modelling of methylene blue adsorption onto seaweed, coconut shell and oak wood hydrochars," Water, vol. 15, no. 977, pp. 1–25, 2023, doi: 10.3390/w15050977.

[11] O. A. Olafadehan, O. W. Jinadu, L. Salami, and O. T. Popoola, "Treatment of brewery wastewater effluent using activated carbon prepared from coconut shell," Int. J. Appl. Sci. Technol., vol. 2, no. 1, pp. 165–178, 2012, [Online]. Available: https://www.ijastnet.com.

[12] B. N. Shelke, M. K. Jopale, and A. H. Kategaonkar, "Exploration of biomass waste as low cost adsorbents for removal of methylene blue dye: A review," J. Indian Chem. Soc., vol. 99, no. 7, 2022, doi: 10.1016/j.jics.2022.100530.

[13] M. A. Mohammed, A. Shitu, and A. Ibrahim, "Removal of methylene blue using low cost adsorbent: A review," Res. J. Chem. Sci., vol. 4, no. 1, pp. 91–102, 2014, [Online]. Available: http://www.isca.me.

[14] R. Karthik, R. Muthezhilan, A. J. Hussain, K. Ramalingam, and V. Rekha, "Effective removal of methylene blue dye from water using three different low-cost adsorbents," Desalin. Water Treat., vol. 57, no. 23, pp. 10626–10631, 2015, doi: 10.1080/19443994.2015.1039598.

[15] P. K. Mondal, R. Ahmad, and R. Kumar, "Adsorptive removal of hazardous methylene blue by fruit shell of Cocos nucifera," Environ. Eng. Manag. J., vol. 13, no. 2, pp. 231–239, 2014, doi: 10.30638/eemj.2014.026.

[16] E. Salehi, M. Askari, A. Azizi, and A. Barati, "Comparison of fixed-bed properties of walnut shell and coconut shellbased activated carbons for dynamic adsorption of methylene blue," in 5th International Conference on Recent Innovations in Chemistry and Chemical Engineering [ICCCE February 2018], Tehran, Iran, 2018, pp. 1–10, [Online]. Available: https://www.iccce.ir.

[17] Ç. Sarici-Özdemir, "Removal of methylene blue by activated carbon prepared from waste in a fixed-bed column," Part. Sci. Technol., vol. 32, no. 3, pp. 311–318, 2014, doi: 10.1080/02726351.2013.851132.

[18] H. C. B. Man, C. O. Akinbile, and C. X. Jun, "Coconut husk adsorbent for the removal of methylene blue dye from wastewater," Bioresources, vol. 10, no. 2, pp. 2859–2872, 2015, doi: 10.15376/biores.10.2.2859-2872.

[19] A. C. W. Wong, S. Lawal, and M. A. A. Zaini, "Optimizing the two-stage adsorber of NaOH-activated coconut shell carbon for methylene blue removal," Int. J. Chem. React. Eng., vol. 20, no. 9, pp. 903–910, 2022, doi: 10.1515/ijcre-2021-0220.

[20] A. Tagade, S. R. Geed, K. B. Samal, and C. Engineering, "Treatment of textile dye methylene blue using coconut adsorbent," Int. Res. J. Eng. Technol., vol. 6, no. 8, pp. 1239–1242, 2019, [Online]. Available: www.irjet.net.

[21] A. M. Aljeboree, A. N. Alshirifi, and A. F. Alkaim, "Kinetics and equilibrium study for the adsorption of textile dyes on coconut shell activated carbon," Arab. J. Chem., vol. 10, no. 2, pp. S3381–S3393, 2017, doi: 10.1016/j.arabjc.2014.01.020.

[22] T. Khan and M. Chaudhuri, "Comparison of adsorption behaviour of coconut coir activated carbon and commercial activated carbon for textile dye," WIT Trans. Ecol. Environ., vol. 148, no. 12, pp. 105–116, 2011, doi: 10.2495/RAV110111.

[23] A. Xavier, J. G. Rajan, D. Usha, and R. Sathya, "Removal of methylene blue by adsorption process - A comparative study," Mater. Sci. Forum, vol. 699, pp. 245–264, 2011, doi: 10.4028/www.scientific.net/MSF.699.245.

[24] V. Yesuratnam, D. Meghavathu, and R. P. Sree, "Removal of methylene blue from aqueous solution using coconut shell powder," iManager's J. Futur. Eng. Technol., vol. 7, no. 2, pp. 25–33, 2012, [Online]. Available: https://www.proquest.com/openview/.

[25] M. Y. Chong and Y. J. Tam, "Bioremediation of dyes using coconut parts via adsorption: a review," SN Appl. Sci., vol. 2, no. 2, pp. 1–16, 2020, doi: 10.1007/s42452-020-1978-y.

[26] S. Srisorrachatr, P. Kri-arb, S. Sukyang, and C. Jumruen, "Removal of basic dyes from solution using coconut shell charcoal," Fifth Int. Multi-Conference Eng. Technol. Innov. 2016 (IMETI 2016), vol. 119, no. 01019, pp. 1–6, 2017, doi: 10.1051/matecconf/201711901019.

[27] N. Prasoetsoph, I. Soonsook, A. Panyayaw, P. Nanon, W. Singsang, and I. Sittitanadol, "Adsorption of methylene blue and ferrous metal solution by using coconut shell charcoal," J. Mater. Sci. Appl. Energy, vol. 12, no. 2, pp. 1–6, 2023, doi: 10.55674/jmsae.v12i2.248672.

[28] Y. C. Sharma and S. N. Upadhyay, "Removal of a cationic dye from wastewaters by adsorption on activated carbon developed from coconut coir," Energy & Fuels, vol. 23, pp. 2983–2988, 2009, doi: 10.1021/ef9001132.

[29] J. D. S. Macedo et al., "Kinetic and calorimetric study of the adsorption of dyes on mesoporous activated carbon prepared from coconut coir dust," J. Colloid Interface Sci., vol. 298, pp. 515–522, 2006, doi: 10.1016/j.jcis.2006.01.021.

[30] U. J. Etim, S. A. Umoren, and U. M. Eduok, "Coconut coir dust as a low cost adsorbent for the removal of cationic dye from aqueous solution," J. Saudi Chem. Soc., vol. 20, pp. S67–S76, 2016, doi: 10.1016/j.jscs.2012.09.014.

[31] S.-A. Ong, L.-N. Ho, Y.-S. Wong, and A. Zainuddin, "Adsorption behavior of cationic and anionic dyes onto acid treated coconut coir," Sep. Sci. Technol., vol. 48, no. 14, pp. 2125–2131, 2013, doi: 10.1080/01496395.2013.792839.

[32] H. A. Al-Aoh et al., "Optimization of conditions for preparation of activated carbon from coconut husk fiber using responses from measurements of surface area and adsorption," Asian J. Chem., vol. 28, no. 4, pp. 714–724, 2016, doi: 10.14233/ajchem.2016.19373.

[33] L. Zhang et al., "Coconut-based activated carbon fibers for efficient adsorption of various organic dyes," RSC Adv., vol. 8, pp. 42280–42291, 2018, doi: 10.1039/C8RA08990F.

[34] V. E. Efeovbokhan et al., "Preparation and characterization of activated carbon from plantain peel and coconut shell using biological activators," in International Conference on Engineering for Sustainable World-Journal of Physics: Conference Series, 2019, vol. 1378, no. 032035, pp. 1–15, doi: 10.1088/1742-6596/1378/3/032035.

[35] O. Edokpayi, O. Osemwenkhae, B. V Ayodele, J. Ossai, S. A. Fadilat, and S. E. Ogbeide, "Batch adsorption study of methylene blue in aqueous solution using activated carbons from rice husk and coconut shell," J. Appl. Sci. Environ. Manag., vol. 22, no. 5, pp. 631–635, 2018, doi: 10.4314/jasem.v22i5.4.

[36] H. Shukor, A. Z. Yaser, N. F. Shoparwe, M. M. Z. Makhtar, and N. Mokhtar, "Biosorption study of methylene blue (MB) and brilliant red remazol (BRR) by coconut dregs," Int. J. Chem. Eng., vol. 2022, no. 8153617, pp. 1–11, 2022, doi: 10.1155/2022/8153617.

[37] A. H. Jawad et al., "Microwave-assisted preparation of mesoporous activated carbon from Coconut (Cocos nucifera) leaf by H3PO4-activation for methylene blue adsorption," Chem. Eng. Commun., pp. 1–48, 2017, doi: 10.1080/00986445.2017.1347565.

[38] R. Abd Rashid, A. H. Jawad, M. A. M. Ishak, and N. N. Kasim, "FeCl3-activated carbon developed from coconut leaves: Characterization and application for methylene blue removal," Sains Malaysiana, vol. 47, no. 3, pp. 603–610, 2018, doi: 10.17576/jsm-2018-4703-22.

[39] A. H. Jawad, R. Abd Rashid, R. M. A. Mahmoud, M. A. M. Ishak, N. N. Kasim, and K. Ismail, "Adsorption of methylene blue onto coconut (Cocos nucifera) leaf: optimization, isotherm and kinetic studies," Desalin. Water Treat., pp. 1–15, 2015, doi: 10.1080/19443994.2015.1026282.

[40] S. Parvin, W. Rahman, I. Saha, J. Alam, and M. R. Khan, "Coconut tree bark as a potential low-cost adsorbent for the removal of methylene blue from wastewater," Desalin. Water Treat., vol. 146, pp. 385–392, 2019, doi: 10.5004/dwt.2019.23598.

[41] K. Khalid, M. A. K. M. Hanafiah, W. K. Azira, and W. M. Khalir, "Effect of physicochemical parameters on methylene blue adsorption by sulfuric acid treated spent grated coconut," Appl. Mech. Mater., vol. 752–753, pp. 71–76, 2015, doi: 10.4028/www.scientific.net/AMM.752-753.71.

[42] L. Wu, X. Zhang, J. A. Thorpe, L. Li, and Y. Si, "Mussel-inspired polydopamine functionalized recyclable coconut shell derived carbon nanocomposites for efficient adsorption of methylene blue," J. Saudi Chem. Soc., vol. 24, no. 8, pp. 642–649, 2020, doi: 10.1016/j.jscs.2020.07.002.

[43] L. Wu, X. Zhang, and Y. Si, "Polydopamine functionalized superhydrophilic coconut shells biomass carbon for selective cationic dye methylene blue adsorption," Mater. Chem. Phys., vol. 279, no. 125767, 2022, doi: 10.1016/j.matchemphys.2022.125767.

[44] P. C. V Regunton, D. Sumalapao, and N. R. Villarant, "Biosorption of methylene blue from aqueous solution by coconut (Cocos nucifera) shell-derived activated carbon-chitosan composite," Orient. J. Chem., no. 34, pp. 115–124, 2018, doi: 10.13005/OJC/340113.

[45] N. A. Abdullah, P. S. Abdullah, M. F. M. Amin, and N. A. Zainol, "Application of magnetic coconut shell-derived biocarbon for methylene blue removal," in Proceedings of The 2nd International Conference On Advance And Scientific Innovation [ICASI 2019, 18 July], Banda Aceh, Indonesia, 2019, pp. 1–8, doi: 10.4108/eai.18-7-2019.2288485.

[46] A. Islam, M. J. Ahmed, W. A. Khanday, M. Asif, and B. H. Hameed, "Mesoporous activated coconut shell-derived hydrochar prepared via hydrothermal carbonization-NaOH activation for methylene blue adsorption," J. Environ. Manage., vol. 203, no. Pt 1, pp. 237–244, 2017, doi: 10.1016/j.jenvman.2017.07.029.

[47] A. Musa, B. S. Sani, F. B. Ibrahim, and A. Giwa, "Comparative analysis of the adsorption of methylene blue using magnetised and non-magnetised coconut shell biochar," UNIOSUN J. Eng. Environ. Sci., vol. 1, no. 2, pp. 36–47, 2019, doi: 10.36108/ujees/9102.10.0250.

[48] W. Widiyastuti, M. F. Rois, N. M. I. P. Suari, and H. Setyawan, "Activated carbon nanofibers derived from coconut shell charcoal for dye removal application," Adv. Powder Technol., vol. 31, no. 8, pp. 3267–3273, 2020, doi: 10.1016/j.apt.2020.06.012.

[49] H. T. Van, T. M. P. Nguyen, V. T. Thao, X. H. Vu, T. V. Nguyen, and L. H. Nguyen, "Applying activated carbon derived from coconut shell loaded by silver nanoparticles to remove methylene blue in aqueous solution," Water, Air, Soil Pollut., vol. 229, no. 393, pp. 1–14, 2018, doi: 10.1007/s11270-018-4043-3.

[50] A. Qisti, Y. Utomo, and D. A. Rokhim, "Treatment of dye wastewater from batik industry by coconut shell activated carbon adsorption," Fuller. J. Chem., vol. 6, no. 1, pp. 7–13, 2021, doi: 10.37033/fjc.v6i1.213.

[51] A.-S. Kamdod and M. V. P. Kumar, "Adsorption of methylene blue, methyl orange, and crystal violet on microporous coconut shell activated carbon and its composite with chitosan: Isotherms and kinetics," J. Polym. Environ., vol. 30, pp. 5274–5289, 2022, doi: 10.1007/s10924-022-02597-w.

[52] K. Shah and A. Parmar, "Physico-chemical characteristics of activated carbon prepared from coconut shell," Int. J. Latest Eng. Res. Appl., vol. 3, no. 1, pp. 27–31, 2018, [Online]. Available: http://www.ijlera.com.

[53] Q. Liang et al., "Optimized preparation of activated carbon from coconut shell and municipal sludge," Mater. Chem. Phys., vol. 241, no. 122327, pp. 1–35, 2020, doi: 10.1016/j.matchemphys.2019.122327.

[54] Y. C. Sharma, Uma, A. S. K. Sinha, and S. N. Upadhyay, "Characterization and adsorption studies of Cocos nucifera L. activated carbon for the removal of methylene blue from aqueous solutions," J. Chem. Eng. Data, vol. 55, no. 8, pp. 2662–2667, 2010, doi: 10.1021/je900937f.

[55] A. O. Alabdullatif, A. H. Yahaya, R. Yahya, and H. A. Al-Aoh, "Removal of methylene blue from synthetic waste water by coconut husk fiber based-activated carbon," Asian J. Chemis, vol. 26, no. 24, pp. 8325–8332, 2014, doi: 10.14233/ajchem.2014.16954.

[56] B. H. Hameed, D. K. Mahmoud, and A. L. Ahmad, "Equilibrium modeling and kinetic studies on the adsorption of basic dye by a low-cost adsorbent: Coconut (Cocos nucifera) bunch waste," J. Hazard. Mater., vol. 158, pp. 65–72, 2008, doi: 10.1016/j.jhazmat.2008.01.034.

[57] H. Al-Aoh, R. Yahya, M. J. Maah, and M. R. Bin Abas, "Adsorption of methylene blue on activated carbon fiber prepared from coconut husk: isotherm, kinetics and thermodynamics studies," Desalin. Water Treat., vol. 52, pp. 6720–6732, 2014, doi: 10.1080/19443994.2013.831794.

[58] O. Oribayo et al., "Coconut shell-based activated carbon as adsorbent for the removal of dye from aqueous solution: Equilibrium, kinetics, and thermodynamic studies," Niger. J. Technol., vol. 39, no. 4, pp. 1076–1084, 2020, doi: 10.4314/njt.v39i4.14.

[59] I. A. W. Tan, A. L. Ahmad, and B. H. Hameed, "Adsorption of basic dye on high-surface-area activated carbon prepared from coconut husk: Equilibrium, kinetic and thermodynamic studies," J. Hazard. Mater., vol. 154, pp. 337–346, 2008, doi: 10.1016/j.jhazmat.2007.10.031.

[60] S. Islam, B. C. Ang, S. Gharehkhani, and A. B. M. Afifi, "Adsorption capability of activated carbon synthesized from coconut shell," Carbon Lett., vol. 20, pp. 1–9, 2016, doi: 10.5714/CL.2016.20.001.

[61] N. Kannan and M. M. Sundaram, "Kinetics and mechanism of removal of methylene blue by adsorption on various carbons-A comparative study," Dye. Pigment., vol. 51, pp. 25–40, 2001, doi: 10.1016/S0143-7208(01)00056-0.

[62] A. K. Prajapati and M. K. Mondal, "Comprehensive kinetic and mass transfer modeling for methylene blue dye adsorption onto CuO nanoparticles loaded on nanoporous activated carbon prepared from waste coconut shell," J. Mol. Liq., vol. 307, no. 112949, pp. 1–18, 2020, doi: 10.1016/j.molliq.2020.112949.

[63] D. Kavitha and C. Namasivayam, "Experimental and kinetic studies on methylene blue adsorption by coir pith carbon," Bioresour. Technol., vol. 98, pp. 14–21, 2007, doi: 10.1016/j.biortech.2005.12.008.
[64] R. H. Khuluk, A. Rahmat, and B. Suharso, "Removal of methylene blue by adsorption onto activated carbon from coconut shell (Cocous nucifera L.)," Indones. J. Sci. Technol., vol. 4, no. 2, pp. 229–240, 2019, [Online]. Available: http://ejournal.upi.edu/index.php/ijost/.
[65] N. H. Abdullah et al., "Effect of acidic and alkaline treatments to methylene blue adsorption from aqueous solution by coconut shell activated carbon," Int. J. Curr. Sci. Eng. Technol., pp. 1–6, 2017, doi: 10.30967/ijcrset.1.S1.2018.319-324.
[66] M. Ismail, M. A. K. M. Hanafiah, M. S. Z. Abidin, Z. Hussin, and K. Khalid, "Kinetics of methylene blue adsorption on sulphuric acid treated Coconut (Cocos nucifiera) frond powder," Am. J. Environ. Eng., vol. 5, no. 3A, pp. 33–37, 2015, doi: 10.5923/c.ajee.201501.06.
[67] K. Y. Foo and B. H. Hameed, "Coconut husk derived activated carbon via microwave induced activation: Effects of activation agents, preparation parameters and adsorption performance," Chem. Eng. J., vol. 184, pp. 57–65, 2012, doi: 10.1016/j.cej.2011.12.084.
[68] Y. Yasin, M. Z. Hussein, and F. H. Ahmad, "Adsorption of methylene blue onto treated activated carbon," Malaysian J. Anal. Sci., vol. 11, no. 11, pp. 400–406, 2007, [Online]. Available: https://www.researchgate.net/publication/251289860.
[69] C. E. Gimba, J. Y. Olayemi, S. T. Okunnu, and J. A. Kagbu, "Adsorption of methylene blue by activated carbon from coconut shell," Glob. J. Pure Appl. Sci., vol. 7, no. 2, pp. 265–267, 2000, doi: 10.4314/gjpas.v7i2.16242.
[70] A. H. A. Dabwan, N. Yuki, N. A. M. Asri, H. Katsumata, T. Suzuki, and S. Kaneco, "Removal of methylene blue, rhodamine B and ammonium ion from aqueous solution by adsorption onto sintering porous materials prepared from coconut husk waste," Open J. Inorg. Non-Metallic Mater., vol. 5, pp. 21–30, 2015, doi: 10.4236/ojinm.2015.52003.
[71] R. Shaheed, C. H. Azhari, A. Ahsan, and W. H. M. W. Mohtar, "Production and characterisation of low-tech activated carbon from coconut shell," J. Hydrol. Environ. Res., vol. 3, no. 1, pp. 6–14, 2015, [Online]. Available: https://hdl.handle.net/10652/4505.
[72] D. Das, D. P. Samal, and B. C. Meikap, "Preparation of activated carbon from green coconut shell and its characterization," J. Chem. Eng. Process Technol., vol. 6, no. 5, pp. 1–7, 2015, doi: 10.4172/2157-7048.1000248.
[73] E. Z. Sulyman and N. Z. Sulyman, "Preparation of activated carbon from coconut shells- Use the Kim-al-Ali as abond material and use it to adsorb the pigment of the methylene blue," Iraqi Natl. J. Chem., vol. 18, no. 2, pp. 104–116, 2018, [Online]. Available: http://iqnjc.com/default.aspx.
[74] P. J. Rangari and P. Chavan, "Preparation of activated carbon from coconut shell," Int. J. Recent Res. Sci. Eng. Technol., vol. 3, no. 4, pp. 598–603, 2017, [Online].Available: http://www.ijrrset.com/upload/2017/april/2_PREPARATION_IEEE.pdf.
[75] O. L. Mercileen, A. K. Patan, and M. V. V. C. Lakshmi, "Selection of chemical activating agent for the synthesis of activated carbon from coconut shell for enhanced dye treatment - its kinetics and equilibrium study," Mater. Proc., vol. 72, no. Part 1, pp. 274–285, 2023, doi: 10.1016/j.matpr.2022.07.290.
[76] A. L. Cazetta et al., "NaOH-activated carbon of high surface area produced from coconut shell: Kinetics and equilibrium studies from the methylene blue adsorption," Chem. Eng. J., vol. 174, pp. 117–125, 2011, doi: 10.1016/j.cej.2011.08.058.
[77] Y. C. Wong, M. S. R. Senan, and N. A. Atiqah, "Removal of methylene blue and malachite green dye using different form of coconut fibre as absorbent," J. Basic Appl. Sci. Mississauga, vol. 9, pp. 172–177, 2013, [Online].Available: https://www.proquest.com/openview/e92f740f71fbbd890b93cfcdd7c366b9/.
[78] N. Singh and C. Balomajumder, "Equilibrium isotherm and kinetic studies for the simultaneous removal of phenol and cyanide by use of S. odorifera (MTCC 5700) immobilized on coconut shell activated carbon," Appl. Water Sci., pp. 1–15, 2016, doi: 10.1007/s13201-016-0470-8.
[79] A. O. Dada, F. A. Adekola, E. O. Odebunmi, A. S. Ogunlaja, and O. S. Bello, "Two–three parameters isotherm modeling, kinetics with statistical validity, desorption and thermodynamic studies of adsorption of Cu(II) ions onto zerovalent iron nanoparticles," Sci. Rep., vol. 11, no. 16454, pp. 1–15, 2021, doi: 10.1038/s41598-021-95090-8.
[80] J. S. Piccin, G. L. Dotto, and L. A. A. Pinto, "Adsorption isotherms of thermochemical data of FD&C red No 40 binding by chitosan," Brazilian J. Chem. Eng., vol. 28, no. 2, pp. 295–304, 2011, [Online]. Available: http://www.abeq.org.br/bjche.
[81] Y. Premkumar and K. Vijayaraghavan, "Biosorption potential of coco-peat in the removal of methylene blue from aqueous solutions," Sep. Sci. Technol., pp. 37–41, 2015, doi: 10.1080/01496395.2014.968262.
[82] A. Shee, J. M. Onyari, J. N. Wabomba, and D. Munga, "Methylene blue adsorption onto coconut husks/polylactide blended films: Equilibrium and kinetic studies," Chem. Mater. Res., vol. 6, no. 11, pp. 28-, 2014, [Online]. Available: http://www.iiste.org.
[83] H. K. Yagmur and I. Kaya, "Synthesis and characterization of magnetic ZnCl2-activated carbon produced from coconut shell for the adsorption of methylene blue," J. Mol. Struct., vol. 1232, no. 130071, pp. 1–12, 2021, doi: 10.1016/j.molstruc.2021.130071.
[84] N. Mozaffari, A. H. S. Mirzahosseini, and N. Mozaffari, "A new kinetic models analysis for CO adsorption on palladium zeolite nanostructure by roll-coating technique," Anal. Methods Environ. Chem. J., vol. 3, no. 2, pp. 92–107, 2020, doi: 10.24200/amecj.v3.i02.106.
[85] I.-H. T. Kuete, D. R. T. Tchuifon, G. N. Ndifor-Angwafor, A. T. Kamdem, and S. G. Anagho, "Kinetic, isotherm and thermodynamic studies of the adsorption of thymol blue onto powdered activated carbons from Garcinia cola nut shells impregnated with H3PO4 and KOH: Non-linear regression analysis," J. Encapsulation Adsorpt. Sci., vol. 10, pp. 1–27, 2020, doi: 10.4236/jeas.2020.101001.
[86] J. O. Ojediran, A. O. Dada, S. O. Aniyi, R. O. David, and A. D. Adewumi, "Mechanism and isotherm modeling of effective adsorption of malachite green as endocrine disruptive dye using acid functionalized maize cob (AFMC)," Sci. Rep., vol. 11, no. 21498, pp. 1–15, 2021, doi: 10.1038/s41598-021-00993-1.
[87] A. A. Inyinbor, F. A. Adekola, and G. A. Olatunji, "Kinetics, isotherms and thermodynamic modeling of liquid phase adsorption of Rhodamine B dye onto Raphia hookerie fruit epicarp," Water Resour. Ind., vol. 15, pp. 14–27, 2016, doi: 10.1016/j.wri.2016.06.001.

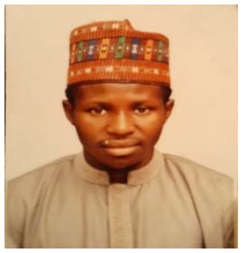

Abdulghaffaar Assayyidi Yusuf is currently working as a lecturer in the Department of Science, School of General Studies, National Institute of Construction Technology and Management, Uromi, Edo State, Nigeria. He has completed his Bachelors and Masters of Engineering in Chemical Engineering from the University of Maiduguri, Nigeria. His research in PG focused on the 'Development and Assessment of Activated Carbon Derived from Coconut Shell on Adsorption of Methylene Blue Dye in Wastewater'. He has published 4 international articles at various journals. He has teaching experience of more than 3 years.

Abdulhalim Musa Abubakar works as Assistant Lecturer at Modibbo Adama University, Yola, Adamawa State, Nigeria in the Department of Chemical Engineering since 2019. He obtained a B.Eng. and M.Eng. Degrees from University of Maiduguri in 2018 and 2023, respectively. He had basic experience in programming languages (C++, Fortran & R, inclusive) and had identified the scope of those languages in chemical engineering, where he solved several numerical problems, witnessed in some of his publications. Moreso, other research interest he had contributed a lot are in biomass conversion, environmental engineering, plant design and simulation, sustainable energy and bioremediation. Altogether, more than 57 of his peer-reviewed local and international journal publications covers those areas mentioned.

Abdulrazak Muhammad is currently working as Lecturer II in the Department of Agricultural Technology at Federal College of Horticulture Dadin Kowa, Gombe state. He has completed his B. Eng. Degree in Mechanical Engineering at University of Maiduguri, Borno state of Nigeria as well as his Masters Program in the same institution. His M.Eng. research work was on 'Maximum Power Point Tracking of Photovoltaic System Modules at FECOHORT' and 'Working on Improved Particle Swarm Optimization of Maximum Power Point Tracking of Solar PVs under Partial

Shading Conditions'. He has published in national and international journals. He has participated in various national and international conferences, seminars, webinars and workshops organized by different reputed institutions. He received numerous certificates in that respect. Engr. Abdulrazak has teaching experience of more than 10 years. He guided 23 Undergraduate Project Students from 2016-2023.

Kamran Khan is PhD Scholar in Environmental Engineering in University of Wollongong Australia. Before then, he completed his Master's Degree in Petroleum and Mining Engineering from Politecnico Di Torino, Italy in 2021. He completed his Bachelor's Degree in Petroleum and Gas Engineering at BUITEMS, Pakistan in 2015.

G. Rajasekar is currently working as an Assistant Professor in the Department of Plant Pathology at Adhiyamaan College of Agriculture and Research, Athimugam, Hosur, affiliated to Tamil Nadu Agricultural University (TNAU), Coimbatore. He has completed his B.Sc. Degree in Agriculture at Annamalai University, Chidambaram; PG, at Agricultural College and Research Institute (TNAU), Killikulam, Tuticorin and; completed his Ph.D. Program at Agricultural College and Research Institute (TNAU), Madurai. His research in PG focused on 'Studies on the fusarium head blight disease of wheat caused by *Fusarium graminearum* (Schwabe.)' and his Ph.D. research work was on 'Exploring antifungal potential of phylloplane bacteria and plant extracts against brown spot of rice incited by *Bipolaris oryzae* Subr. and Jain'. He has published 7 National and International articles at various journals, 35 popular articles, 1 book chapter and 1 book. He has participated in various national and international conferences, seminars (totaling to 10, organized by different reputed institutions) and webinars, where he received numerous certificates.

Light yield measurement of the Ce3+ activated LuAG nano-powder garnet scintillating detector

Hamza Mekki, Lakhdar Guerbous, Hicham Bousbia-Salah, Billel Zahra, and Allaoua Boukerika.

Abstract− This paper focuses on the characterization of nano-powder (NP) scintillator, specifically presenting preliminary results of the measurement of the light yield (LY) of a newly synthesized Lutetium Aluminum (LuAG) garnet phosphor NP scintillator, doped with 0.1% cerium. The scintillation light yield was measured using the comparative method. Considering the light-scattering and self-absorbing properties of powder scintillators, alpha particles from ^{241}Am source were used for excitation instead of Gamma/X rays, while a Ce^{3+} activated LuAG single crystal (SC) was employed as the reference detector due to its well-established light yield. A photomultiplier tube (PMT) served as the photodetector, and signals were read out by a nuclear instrumentation chain. The results demonstrate that the newly prepared LuAG:Ce NP exhibits a light output that is approximately 90% of that of the single crystal reference. These findings highlight the promising potential of NP scintillators as a viable alternative to single crystals, especially in applications where the preference for powder scintillators is evident.

***Keywords*− LuAG scintillation detector, light yield measurement, alpha particles, nano-powder.**

Nomenclature

Am	Americium
HV	High Voltage
LY	Light Yield
MCA	Mulichannel Analyzer
NP	Nano-powder
PL	Photoluminescence
PMT	Photomultiplier Tube
SC	Single crystal

I. Introduction

Several applications [1], [2] such as homeland security, medical imaging diagnosis, high energy physics (HEP), industrial nondestructive control, environmental monitoring rely on radiation detection using scintillating materials as detectors. In these applications, certain scintillating detector characteristics are crucial for their effectiveness. For example, medical imaging diagnosis applications like positron emission tomography (PET) require high scintillation light yield (LY) and fast time resolution to improve signal-to-noise ratio, image quality, accuracy, and reduce patient dose[1], [3]–[5]. In certain applications, nano-sized scintillator, such as rare earth activated garnet phosphor NPs, can serve as an alternative to single crystal scintillators, as they are easier to synthesize compared to growing single crystals. This makes them a more cost-effective option for applications like high energy physics (HEP) and X-ray computed tomography (CT) [6].

Among the inorganic scintillators, Ce^{3+}-activated lutetium aluminum garnet with the general formula Lu3Al5O12 (LuAG:Ce^{3+}) in powder form shows promise due to its excellent properties, including chemical and mechanical stability, good optical properties, and high density (6.73 g/cm3) [7]. However, determining the optimal composition for achieving the best scintillation performances requires both theoretical and experimental investigations. Scintillators in powder form are known for light scattering and self-absorption [8]. Powder samples with a thickness of (1-3) mm are not transparent, resulting in a significant fraction of generated photons being scattered and reabsorbed by the material itself. As result, only a limited number of photons are able to reach the photodetector, Making it challenging to measure scintillation characteristics in the absence of certain elements, such as the lack of a photo-peak in the energy spectrum. This lack of efficiency, especially for gamma and X-rays is due to the requirement for significant absorption depth, which is not achievable with small powder samples. On the other hand, thick powder samples exhibit strong light scattering and absorption. Consequently, powder materials are not efficient in terms of gamma and X-ray absorption [9]. Therefore, careful attention should be given for the choice of excitation radiation when measuring the scintillation properties of powder materials[1][9]. In characterization tasks, achieving a high scintillation light yield (LY) is crucial for obtaining accurate measurement signals. However, obtaining a high LY with gamma and X-ray radiation is a challenge. On the other hand, it has been found that alpha particles are more efficient when interacting with powder scintillators. This is because alpha particles are absorbed in the surface layers of the sample (within a few microns) [1], Additionally, alpha particles have high energy, leading to a greater production of photons and thus better measurement signals. In such circumstances, the excitation geometry also plays a role in ensuring a good collection of the scintillation photons. Considering the excitation geometry is important for efficiency of the measurement setup[1][6]. In addition, and for the excitation with alpha particles, The investigation demonstrated that the

Manuscript received July 23, 2023; revised July 3, 2024.

H. Mekki and B. Zahra are with the Electronics Department, Ecole Nationale polytechnique, Algiers, ALGERIA, and with Department of detection and nuclear instrumentation, centre de recherche nucléaire de Birine (CRNB), (e-mail: hamza.mekki@g.enp.edu.dz, billel.zahra@g.enp.edu.dz).).

L. Guerbous Author is with the Laser Department, Centre de recherche Nucléaire d'Alger, Algiers, ALGERIA (e-mail: l.guerbous@crna.dz).

H. Bousbia-salah is with the Electronics Department, Ecole Nationale polytechnique, Algiers, ALGERIA (e-mail: hicham.bousbia-salah@g.enp.edu.dz).

A. Boukerika is with the Physics division, Centre de recherche Nucléaire d'Alger, Algiers, ALGERIA (e-mail: a.boukerika@crna.dz).

Digital Object Identifier (DOI): 10.53907/enpesj.v4i1.222

reflection geometry is more suitable for evaluating the scintillation properties of powder scintillators, rather than transmission geometry [1][9].

The objective of this work is to measure the scintillation light yield of a newly prepared Ce^{3+} doped lutetium aluminum garnet $Lu_3Al_5O_{12}$ (LuAG) NP scintillator. The scintillator was synthesized using the Sol-Gel method, and a previous study investigated the effect of Ce^{3+} concentration on the photoluminescence (PL) properties, determining that the optimal Ce^{3+} dopant concentration for the highest PL performance is 0.1% [7].

Various methods are commonly used to measure the scintillation light yield of scintillator detectors, which are detailed in [10]. In this work, the comparison method was employed, and the light yield was estimated using a Ce-doped LuAG single crystal as a reference detector, as its light yield is known (12000-15000 ph/MeV) [11]–[13]. Alpha particles with an energy of 5.48 MeV from ^{241}Am were used for excitation, a photomultiplier tube (PMT) was served as a photodetector and the reflection geometry was applied.

II. METHOD AND EXPERIMENTAL DETAILS

A. Samples preparation

Ce^{3+} doped lutetium aluminum garnet NPs (LuAg:Ce^{3+}) were synthesized using the sol-gel method, as described in[7]. The NP scintillator was synthesized with a Ce^{3+} concentration of 0.1%. The resulting NPs were then pressed and compacted to form a pellet measuring approximately 1 cm in diameter and 3 mm in thickness, as illustrated in **Fig. 1**.

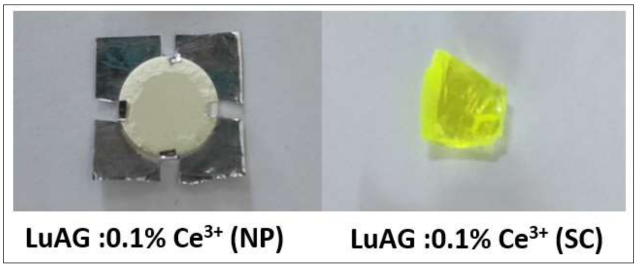

Fig. 1: Photography of the prepared LuAg:0.1%Ce^{3+} (NP) and the LuAg:0.1%Ce^{3+} (SC), the single crystal was used as a reference detector.

The LuAG:0.1%Ce^{3+} SC was developed using the Czochralski growth method. A small portion of comparable size with the NP sample was used as a reference for measuring the light yield. The single crystal sample is shown in Fig. 1. Further details regarding the development of the single crystal can be found in[14], [15].

B. Light yield measurement method

The scintillation light yield (LY), measured in Photons/MeV, is a key characteristic of scintillation detectors. Several methods, including the method of comparison, are commonly employed to determine the LY [16]. The comparison method, as described in the literature[1][10], involves determining the relative light yield (RLY) by comparing the signal amplitudes of the detector under characterization with those of a reference detector with a known LY. Both detectors should be measured in the same setup and under room temperature. The RLY can be calculated using Equation (1):

$$RLY_D(\%)= \frac{PP_{-D}}{PP_{-RD}} * \frac{G_{RD}}{G_D} \tag{1}$$

Where: RLY is the relative light yield (in % of the reference detector), PP_{-D} is the signal amplitude from the detector under test, PP_{-RD} is the signal amplitude from the reference detector, G_{RD} is the amplifier gain applied to reference detector and G_D is the amplifier gain applied to the detector under characterization. The absolute light yield (in ph/Mev) of the detector under characterization can be estimated by multiplying the RLY by the known LY of the reference detector [1] as given in the equation (2).

$$ALY_D=RLY_D .LY_{RD} \tag{2}$$

Where ALY_D is the absolute light yield (in ph/Mev) of the detector under characterization , LY_{RD} is the absolute light yield of the reference detector (in ph/Mev), the absolute light yield of the yield is reported in [11] .

For the measurement of the light yield (LY) of the prepared Ce-doped LuAG NP sample, the LuAg:0.1%Ce^{3+} single crystal was employed as a reference detector. Both of LuAg:Ce SC and NP are depicted in Fig. 1. A calibrated detection chain was utilized to acquire measurement signals and to collect energy spectrums from both the NP and single crystal detectors, in the same configuration and under the reflection geometry.

Alpha particles were used for excitation for two reasons. Firstly, their high energy enables effective discrimination of noise and the production of a well-defined full absorption peak [1]. Secondly, alpha particles interact effectively with scintillator materials over short distances (tens of microns). To determine the light yield (LY), alpha particles with an energy of 5.48 MeV from ^{241}Am (with an 85% yield) were employed as the excitation source. In order to prevent any external light from penetrating, a tightly closed box was used to house the excitation source, samples, and PMT.

The experimental setup used for measuring the light yield of the prepared sample is presented in Fig. 2. The light emitted by the scintillators under excitation by alpha particles was detected by a photomultiplier tube (PMT). The PMT model used was the 6292-DUMONT, featuring a multi-alkali S-9 photocathode. The spectral response of the PMT is well-matched to the spectral emission of the Ce-doped LuAG, with a maximum response in the range of 400-550 nm [17], which exactly aligns with the peak emission wavelength of LuAg:Ce at 500 nm [18]. Both the spectral emission of LuAg:Ce and the spectral response of the PMT fall within the visible light range.

The output of the PMT was connected to the input of the ORTEC 572 amplifier, which served to amplify and shape signals. The amplification gain was fixed at 50 for both prepared and reference detectors. Energy spectra were acquired using the EASY-MCA-8K-CH multichannel analyzer (MCA) from ORTEC and collected using Maestro Software, also from ORTEC.

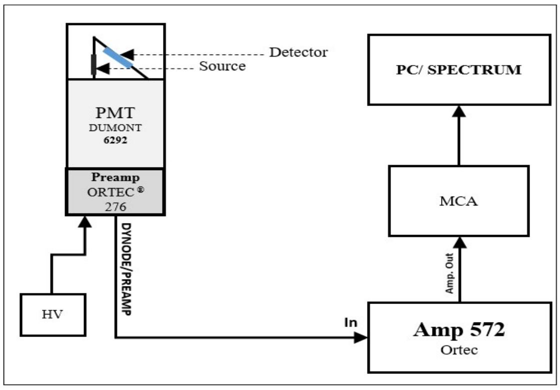

Fig.2: Schematic view of the light measurement setup.

A pulse height spectrum was initially recorded using the LuAg:0.1%Ce^{3+} single crystal reference detector. This process was then repeated with the LuAg:0.1%Ce^{3+} NP detector under characterization. By comparing the positions of the 5.48 MeV photo-peak obtained with the LuAg:Ce single crystal and the

NP, an estimation of the light output of LuAG:0.1%Ce NP can be determined. Fig. 3 illustrates the pulse height spectra recorded for both the LuAg:Ce NP and the single crystal under 5.48 MeV alpha particles excitation, using a shaping time of 6 µs for the amplifier. The selected shaping time allows for the collection of all charges produced in the PMT, ensuring the maximum collection of photons from the scintillator detectors[19]. The PMT was biased with a 1400V high voltage (HV) power supply, and the PMT bias, shaping time, and amplifier gain were the same for both spectrums. To accurately determine the photo-peak center positions, Gaussian fitting was performed on the obtained photo-peaks.

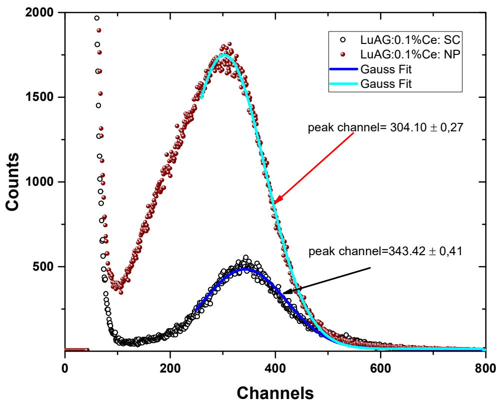

Fig.3: Pulse height spectra of 5.48 Mev alpha particles recorded with LuAg: Ce NP and single crystal (HV=1400V,Shaping time = 6µs, amplification gain = 50, spectra were collected for a time of 1000 s)

III. RESULTS AND DISCUSSION

As shown in the Fig.3, both spectrums show different photo-peak positions. By analyzing the obtained photo-peak for both the LuAg: 0.1%Ce^{3+} NP (detector under test) and the LuAg:0.1%Ce^{3+} SC (reference detector), it was determined that the light output of the prepared sample of the LuAg:0.1%Ce^{3+} NP is approximately 89% of the light output of the LuAg:0.1%Ce^{3+} SC used as reference. Results of the light yield (LY) measurement are presented in both relative and absolute values in Table 1. The absolute LY value of the reference detector used for comparison is that reported in [11] which is of 15000 Ph/MeV.

Table. I
LIGHT YIELD MEASUREMENT RESULTS

Scintillators	PEAK POSITIONS	RELATIVE LIGHT YIELD (%)	ABSOLUTE LIGHT YIELD (PH/MEV)
LuAG SC	343.42±0.4	100	15000
LuAG NP	304.10±0.3	88.55±0.13	13395±25

IV. CONCLUSION

This study is a part of an ongoing endeavor to develop and enhance NP scintillating detectors. The main focus of this research was to characterize the scintillation light yield. By utilizing a reference detector and alpha particles, the light output of a newly developed Ce-activated LuAG NP scintillator was successfully measured. The results indicated that the NP scintillator demonstrates a relatively high light output, comparable to that of the single crystal reference. These findings suggest that NP scintillators have the potential to serve as an alternative to single crystals in certain applications, owing to their ease of development. However, it is important to acknowledge that characterizing powder scintillators presents additional challenges compared to single crystals due to their tendency for light scattering, which can reduce efficiency when detecting certain types of radiation, such as Gamma and X-rays. Further advancements in characterization methods are necessary in this regard. Future work will involve investigating other scintillation properties of NPs, such as timing characteristics, as well as exploring the impact of dopant concentrations on scintillation characteristics.

REFERENCES

[1] E. Gordienko et al., “Synthesis of crystalline Ce-activated garnet phosphor powders and technique to characterize their scintillation light yield,” Opt. Mater. (Amst)., vol. 78, pp. 312–318, 2018, doi: 10.1016/j.optmat.2018.02.045.

[2] C. Dujardin et al., “Needs, trends, and advances in inorganic scintillators,” IEEE Trans. Nucl. Sci., vol. 65, no. 8, pp. 1977–1997, 2018, doi: 10.1109/TNS.2018.2840160.

[3] E. Auffray et al., “A comprehensive and systematic study of coincidence time resolution and light yield using scintillators of different size and wrapping,” IEEE Trans. Nucl. Sci., vol. 60, no. 5, pp. 3163–3171, 2013, doi: 10.1109/TNS.2013.2270089.

[4] M. Salomoni, R. Pots, E. Auffray, and P. Lecoq, “Enhancing light extraction of inorganic scintillators using photonic crystals,” Crystals, vol. 8, no. 2, pp. 1–35, 2018, doi: 10.3390/cryst8020078.

[5] A. Knapitsch and P. Lecoq, “Review on photonic crystal coatings for scintillators,” Int. J. Mod. Phys. A, vol. 29, no. 30, 2015, doi: 10.1142/S0217751X14300701.

[6] G. Dosovitskiy et al., “Polycrystalline scintillators for large area detectors in HEP experiments,” J. Instrum., vol. 12, no. 6, pp. 1–23, 2017, doi: 10.1088/1748-0221/12/06/C06045.

[7] A. Boukerika and L. Guerbous, “Investigation of the structural and photoluminescence properties of Ce3+-doped LuAG nanopowders prepared via sol-gel method,” Opt. Mater. (Amst)., vol. 40, pp. 14–19, 2015, doi: 10.1016/j.optmat.2014.11.039.

[8] S. Sinha, J. Kwong, W. G. J. Langeveld, and P. Ryge, “Characterization of ZnO, BaF2 and PbWO4 scintillator detectors for cargo inspection using transmitted X-ray spectroscopy,” IEEE Trans. Nucl. Sci., vol. 60, no. 2, pp. 1016–1023, 2013, doi: 10.1109/TNS.2013.2241451.

[9] H. Mekki, L. Guerbous, A. Boukerika, and K. Lebbou, “Scintillation properties of (Lu1−x Yx)3Al5O12:Ce3+ nanoscintillator solid solution garnet materials,” J. Instrum., vol. 18, 2023, doi: https://doi.org/10.1088/1748-0221/18/02/P02007.

[10] E. Sysoeva, V. Tarasov, and O. Zelenskaya, “Comparison of the methods for determination of scintillation light yield,” Nucl. Instruments Methods Phys. Res. Sect. A Accel. Spectrometers, Detect. Assoc. Equip., vol. 486, no. 1–2, pp. 67–73, 2002, doi: 10.1016/S0168-9002(02)00676-9.

[11] “High Precision Scintilation Crystals Phosphor Ce:LuAG Crystal High Light Yield,” 2021. http://www.crystro.com/sale-11745046-high-precision-scintilation-crystals-phosphor-ce-luag-crystal-high-light-yield.html

[12] S. Liu, X. Feng, Z. Zhou, M. Nikl, Y. Shi, and Y. Pan, “Effect of Mg2+ co-doping on the scintillation performance of LuAG: Ce ceramics,” Phys. Status Solidi - Rapid Res. Lett., vol. 8, no. 1, pp. 105–109, 2014, doi: 10.1002/pssr.201308199.

[13] T. Yanagida et al., “Scintillation properties of LuAG (Ce) ceramic and single crystalline scintillator,” IEEE Nucl. Sci. Symp. Conf. Rec., pp. 1612–1614, 2010, doi: 10.1109/NSSMIC.2010.5874048.

[14] K. L. A. Nehari, G. Alombert-Goget, O. Benamara, H.Cabane, M. Dumortier, P. Jeandel, I. Lasloudji, F.Mokhtari, T.Baron, G.Wong, M. Allani, J. Boy, S.Alzuaga, L. Arapan, F.Gegot, T.Dufar, “Czochralski crystal growth and characterization of large Langatate (La3Ga5.5Ta0.5O14, LGT) crystals for SAW application,” R. Soc. Chem., vol. 21, no. 11, pp. 1764–1771, 2019, doi: 10.1039/C8CE02157K.

[15] H. Li, E. A. Ghezal, A. Nehari, A. Brenier, and K. Lebbou, “Bubbles defects distribution in sapphire bulk crystals grown by Czochralski technique,” Opt. Mater. (Amst)., vol. 35, pp. 1071–1076, 2013, doi: 10.1016/j.optmat.2012.12.022.

[16] K. S. Shah et al., “CeBr/sub 3/ scintillators for gamma-ray spectroscopy,” in IEEE Symposium Conference Record Nuclear Science 2004., 2004, vol. 7, pp. 4278–4281. doi: 10.1109/NSSMIC.2004.1466835.

[17] DUMONT, “DUMONT_PMT_6292.” [Online]. Available: https://frank.pocnet.net/sheets/085/6/6292.pdf02/Dumont_PMT_6292.pdf

[18] A. Boukerika and L. Guerbous, “Investigation of the structural and photoluminescence properties of Ce3+-doped LuAG nanopowders prepared via sol-gel method,” Opt. Mater. (Amst)., vol. 40, pp. 14–19, 2015, doi: 10.1016/j.optmat.2014.11.039.

[19] K. S. Shah et al., “CeBr 3 scintillators for gamma-ray spectroscopy,” IEEE Trans. Nucl. Sci., vol. 52, no. 6, pp. 3157–3159, 2005, doi: 10.1109/TNS.2005.860155.

Hamza Mekki is currently a PhD from Ecole Nationale polytenchinque, Algiers, Algeria. He has a B.Sc degree in electronics from Blida1 university, Algeria (2004) and Magister degree in signals and systems from the same university (2009). His research involves the challenges and solutions in the nuclear instrumentation field. He currently works as a principale researcher at the department of the detection and nuclear instrumentation of the nuclear research center of Birine.

Lakhdar Guerbous is currently Research Director, Senior Expert Researcher of Physics at Nuclear Research Centre of Algiers. He earned his Bachelor of Mathematics at the Athmane ben Afane High School in M'sila in Algeria in 1990 and his PhD in Physical in luminescent materials from the University of Setif in 2007. Currently, he is developing nano scintillator materials for applications dealing with the nuclear detection and photodynamic therapy. He is author of more than 100 articles, guest speakers at many international conferences, regular reviewer for international journals in his field. Organizer of international conferences and member of many scientific councils of research institutions.

Hicham Bousbia-Salah is currently Associate Professor, Researcher in Signal Processing at Ecole Nationale Polytechnique, Algiers. He earned his Engineering degree in Electronics at Ecole Nationale Polytechnique, Algiers in 1981, his Master degree in Computer Engineering at Wayne State University in USA in 1984 and his PhD in Electronics in Signal Processing from the Ecole Nationale Polytechnique, Algiers in 2006. Currently, he is interested in the field of blind separation of multiple sources from convolutive mixtures and its implementation in signal processing.

Billel Zahra was born in Blida, Algeria. He completed his Bachelor's degree in Mathematics at Ibn Khaldun High School in 2000 and earned an engineering degree in Electronics from Saad Dahleb Blida1 University, Algeria, in 2005. He obtained his Ph.D. in Electronics in 2023 from the Ecole Nationale Polytechnique in Algiers, Algeria. Currently, his research focuses on nuclear instrumentation and the development of new Nano-scintillator-based detectors for radiation detection applications.

Allaoua Boukerika is a Senior Researcher in Materials Physics at the Nuclear Research Center of Algiers. His primary focus lies in the development of new materials based on mixed garnet structures for novel detectors of ionizing radiation. He obtained his PhD in Materials Physics from the University of Jijel in 2014 after completing his bachelor's degree in Science of Nature and Life.

Kinematic Modelling of Humanoid Robot Based on Vectorial Approach

Nacer Hadidi, Chawki Mahfoudi, Mohamed Bouaziz, Zaharuddin Mohamed, and Ahcene Bouzida

Abstract— The present work is dedicated to the study of the inverse kinematics solution of a humanoid bipedal robot with 30 degrees of freedom using a newly approach based on vectors that generated from the geometric space of the robot. The solutions of the inverse kinematics problem for all joints articulations are carried out through a simple and linear equations. Finally, simulations of results are performed through harmonization of trajectories of end effectors of the robot's members.

***Keywords*— biped robot, Humanoid robot, inverse kinematics, robotic, vectors calculus.**

NOMENCLATURE

DKM: Direct Kinematic Model.
IKM : Inverse Kinematic Model.
SSP : Simple support phase.
DSP : Double Support Phase.
$C(\theta_i)$: $\cos(\theta_i)$
$S(\theta_i)$: $\sin(\theta_i)$

I. INTRODUCTION

Robotics has captivated a portion of the scientific community due to its alluring prospects across various domains [1]. Indeed, robotics has progressed rapidly, transcending what was once considered science fiction into reality. Among the many branches of robotics, humanoid bipedal robots have garnered intense research in recent years [2-4]. Researchers continue to tackle challenges in various aspects, striving for advancements beyond completed studies. Researchers have emphasized various concepts within this domain, including mechanical design, kinematic and dynamic modeling…etc.Mechanical design aims to create human-sized robots with a high degree of freedom within a compact volume, presenting a significant challenge [5], [6]. Consequentelly, mathematical modeling in robotics makes another side of chanllenging, like kinematic modeling. In fact, this last one (kinematic modeling) plays a crucial role in providing the foundational equations used in robot's dynamics and control.

This paper presents an inverse kinematics study of a bipedal robot with a significant number of degrees of freedom (30 DOF). The robot is devided on six mains parts, each parts is modeled in its proper frame. However, this last one is reconducted in the principal frame on the robot's hip which will be expressed on the global frame. Basically, according to the used approach, each angle that represent one degrees of fredom is described by three vectors from which should be expressed by its magnitude and its rotation sense.

II. THE MODEL OF THE BIPED ROBOT

The robot model has 30 degrees of freedom (30 DOF) which allow great mobility (Fig. 1).

The robot structure is divided into 06 main parts: the trunk, the neck-head, the upper limbs (right and left arms), and the lower limbs (right and left legs). A primary reference frame is fixed at the hip. Than, all frames within the robot structure are defined according to the Denavit-Hartenberg (DH) convention as it is illustrated in Fig. 1. This allows providing the different matrices that will be used in the Forward Kinematics (Fk). Table 1 summarizes the lengths of the various links of the robot.

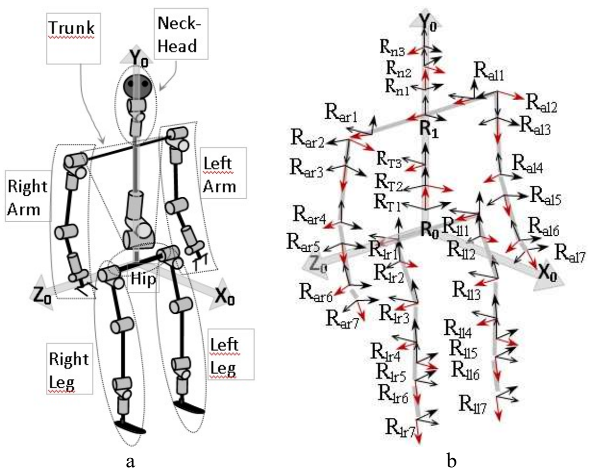

Fig.1: Robot Model. a. Kinematic diagram of the robot. b. Different frames of the robot.

Manuscript received May 22, 2024; revised July 4, 2024.

N. Hadidi is with dept. of mechanical Engineering, Ecole Nationale Superieure des sciences appliquées, Algiers,ALGERIA. (email: nacer.hadidi@ensta.edu.dz).

C. Mahfoudi is with dept. of Mechanical Engeeniring, Univ. of Larbi Ben M'hidi, Oum El Bouaghi, ALGERIA.(email: c_mahfoudi_dz@yahoo.fr).

M. Bouaziz is with dept. of mechanical Engineering, Ecole Nationale Polytechnique, Algiers, ALGERIA. (email: mbouaziz@yahoo.fr).

Z. Mohamed is with dept. Mechatronics, Faculty of Electrical Engineering, Universiti Teknologi Malaysia, Johor Bahru, MALAYSIA. (email: zahar@utm.my).

A. BOUZIDA is with dept. Elctrical Engineering, Univ. Akli Mohand Oulhadj, Bouira, ALGERIA. (email: a.bouzida@univ-bouira.dz).

Digital Object Identifier (DOI): 10.53907/enpesj.v4i1.271

Table 1.
LENGTHS OF ROBOT LINKS

MECHANISMS	ELEMENTS	LENGTHES (m)
Uper limb	Fore-arm	$L_{fa} = 0.28$
	arm	$L_a = 0.30$
	hand	$L_h = 0.10$
Lower limb	Leg	$L_l = 0.30$
	Shin	$L_s = 0.30$
	feet	$L_f = 0.10$
Middle part	Trunc	$L_T = 0.30$
	Hip	$L_H = 0.10$
Head-neck	Head-neck	$L_n = 0.10$

III. KINEMATIC MODELING OF THE ROBOT

Kinematic modeling serves as the foundation in robotics, known through the Forward Kinematic Model (FKM) and Inverse Kinematic Model (IKM).

A. Forward kinematic Model

According to DH convention, the transformation from basic frame to end-effector is expressed by the following matrix given in (1).

$$\begin{bmatrix} s_x n_x a_x P_{dx} \\ s_y n_y a_y P_{dy} \\ s_z n_z a_z P_{dz} \\ 0\ 0\ 0\ \ 1 \end{bmatrix} = {}^0T_1\ {}^1T_2\ {}^2T_3 \ldots {}^{n-1}T_n \qquad (1)$$

$$= [\mathbf{S\ N\ A\ P}]$$

Where:

[**S N A P**]: exprime orientation and position of end-effector in basic frame. ${}^{i-1}T_i$ is a matrix of homogeneous transformation between two successive frames ($i = 1 \ldots n$).

B. Principle of the Inverse Kinematic Calculation Approach.

In this section, we use the new proposed approach that established by [7] which is fonded on a vectorial description of the robot to solve the IK problem. One of the most useful mathematical formula that used to be explored in robotics in provinding analythecal solution of variable articulation β (angle) expressed between two vectors, $\vec{U}$ and $\vec{V}$, is given in (2).

$$\beta = atan2\left(\sin(\vec{U},\vec{V}), \cos(\vec{U},\vec{V})\right) \qquad (2)$$

Subsequentlly, the formula in (2) has an advantage in provinding the correct orientation and value of the angle β at any quadrant of the cercle. In addition, a suitable relation between $\sin(\vec{U},\vec{V})$ and $\det(\overrightarrow{n_U},\overrightarrow{n_V},\overrightarrow{n_W})$ is established by [7].

$$\sin(\vec{U},\vec{V}) = \det(\overrightarrow{n_U},\overrightarrow{n_V},\overrightarrow{n_W}) \qquad (3)$$

Where:

$\overrightarrow{n_U} = \frac{\vec{U}}{U}$, $\overrightarrow{n_V} = \frac{\vec{V}}{V}$ and $\overrightarrow{n_W} = \frac{\vec{w}}{w}$ are, respectivelly, unit vectors of $\vec{U}$, $\vec{V}$ and $\vec{W}$. The vector $\vec{W}$ could be the cross product of $\vec{U}$and $\vec{V}$ or any other orthogonal vector to the plane formed by $\vec{U}$and $\vec{V}$ (UV-plane).

A notable characteristic of determinant regarding its sign emerges when two columns are swapped [8].

$$\det(\overrightarrow{n_U},\overrightarrow{n_V},\overrightarrow{n_W}) = (-1)\det(\overrightarrow{n_V},\overrightarrow{n_U},\overrightarrow{n_W})$$

By knowing, the determinant calculated from the vectors concerning the angle and its cosine value, equation (2) fully determines the angle, including both its sign and value. Hence, equation (2) can be writen as shown in (3)

$$\beta = atan2\left(\det(\overrightarrow{n_U},\overrightarrow{n_V},\overrightarrow{n_W}), \cos(\vec{U},\vec{V})\right) \qquad (3)$$

C. Calculation and identification of angles of the bipedal robot.

As mentioned in the introduction, the biped robot is divided into 06 parts. Therefore, we proceed to model each one separately.

1) Inverse Kinematic Modeling of the Trunk

The movement of the trunk is generated by three joint angles (Fig.2).

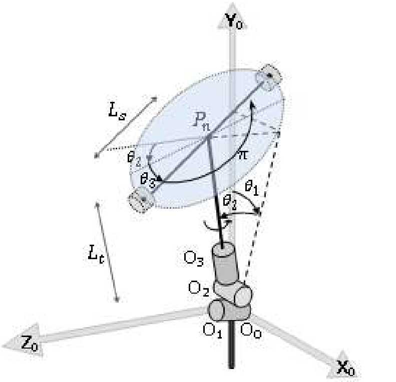

(a)

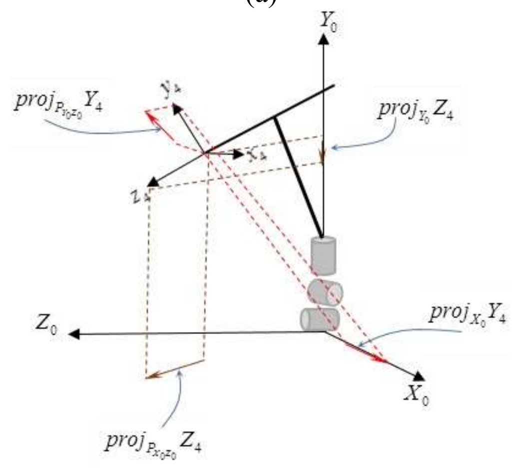

(b)

Fig.2: Geometric Description of the Trunk and Shoulder mechanism. a. Geometric Modeling of the Trunk. b. Current Position of the Shoulder.

The joint angle θ_3 is determined by the following three vectors: $proj_{P_{X0Z0}}\overrightarrow{Z_4}$, $\overrightarrow{Z_0}$ et $\overrightarrow{Y_0}$.

Knowing that: $proj_{P_{X0Z0}}\overrightarrow{Z_4} = \overrightarrow{Z_4} - proj_{Y_0}\overrightarrow{Z_4}$. is the projection of the vector $\overrightarrow{Z_4}$ onto the plane $P_{X_0Z_0}$.

$\overrightarrow{Z_4}$ is a direction cosine vector of the desired shoulder position matrix.

So, θ_3 is expressed by (4):

$$\theta_3 = \text{atan2}\left(det_{\theta_3}, \cos\theta_3\right) \qquad (4)$$

Where: $det_{\theta_3} = det\left[\overrightarrow{Z_0}\ \ proj_{P_{X0Z0}}\overrightarrow{Z_4}\ \ \overrightarrow{Y_0}\right]^T$ and $\cos\theta_3 = \overrightarrow{Z_0} \cdot proj_{P_{X0Z0}}\overrightarrow{Z_4}$

Determining the joint angles θ_1 and θ_2 involves first determining the position of the midpoint (P_n) through the matrix giving the desired shoulder position via the following relationship :

$$\overrightarrow{OP_n} = \overrightarrow{OP_s} - L_s\,\overrightarrow{A_4}$$

Where

$\overrightarrow{OP_n}$: Vector expressing midpoint of schoulders.

$\overrightarrow{OP_s}$: Vector expressing schoulder position.

L_s : Length of schoulder.

$\overrightarrow{A_4}$: Vector of cosine direction of schoulder's frame on z-axis.

The angle θ_1 is determined by the following vectors: $proj_{P_{X0Y0}}\overrightarrow{n_{Pn}}$, $\overrightarrow{Y_0}$ and $\overrightarrow{Z_0}$.

Given that: $proj_{P_{X0Y0}}\overrightarrow{n_{Pn}} = \overrightarrow{n_{Pn}} - proj_{Z_0}\overrightarrow{n_{Pn}}$ it is the projection of the vector $\overrightarrow{n_{P_n}}$ onto the plane $P_{X_0Y_0}$

Where: $\overrightarrow{n_{P_n}}$ is the unit vector of $\overrightarrow{OP_n}$.

$$\theta_1 = atan2\left(det_{\theta_1}, \cos(\theta_1)\right) \qquad (5)$$

With : $det_{\theta_1} = det\left[\overrightarrow{Y_0}\ \ proj_{P_{X0Y0}}\overrightarrow{n_{Pn}}\ \ \overrightarrow{Z_0}\right]^T$ and $\cos(\theta_1) = \overrightarrow{Y_0}\,.\,proj_{P_{X0Y0}}\overrightarrow{n_{Pn}}$

Angle θ_2 is determined by the following vectors: $proj_{P_{Y0Z0}}\overrightarrow{n_{Pn}}$, $\overrightarrow{Y_0}$ et $\overrightarrow{X_0}$

Given that: $proj_{P_{Y0Z0}}\overrightarrow{n_{Pn}} = \overrightarrow{n_{Pn}} - (proj_{X_0}\overrightarrow{n_{Pn}})$. It is the projection of the vector $\overrightarrow{n_{P_n}}$ onto the plane $P_{Y_0Z_0}$

$$\theta_2 = atan2\left(det_{\theta_2}, \cos(\theta_2)\right) \qquad (6)$$

With: $det_{\theta_2} = det\left[\overrightarrow{Y_0}\ \ proj_{P_{Y0Z0}}\overrightarrow{n_{Pn}}\ \ \overrightarrow{X_0}\right]^T$ and

$$\cos(\theta_2) = \overrightarrow{Y_0}\,.\,proj_{P_{Y0Z0}}\overrightarrow{n_{Pn}}$$

2) Inverse Kinematic Modeling of the Neck-Head Mechanism

The movement of the head is governed by the joints incorporated at the robot's neck θ_4, θ_5 and θ_6 as shown in Fig.3.

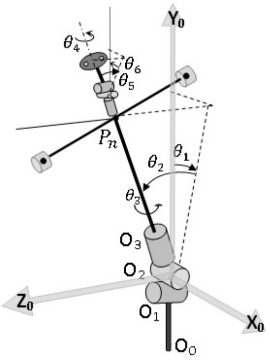

Fig.3: Joints angles of the Neck-Head.mechanism.

During the robot's movement, the head that is connected to trunk at midpoint by the neck with three joint articulations is assumed to be on the vertical straight position.

Therefore, and from Fig.3, the joints θ_5 and θ_6 must respectively have the same values as θ_2 and θ_1 of the trunk, but in opposite rotation, as expressed in (7). Also, the Joint θ_4 is assumed to be stationary.

$$\theta_5 = -\theta_2 \quad et \quad \theta_6 = -\theta_1 \qquad (7)$$

3) Inverse Kinematic Modeling of the Upper Limb (Arm).

Fig. 4 depicts a right upper limb with 6 degrees of freedom of the bipedal robot distributed among three links: the upper arm (L_a), the forearm (L_{fa}), and the hand (L_h)

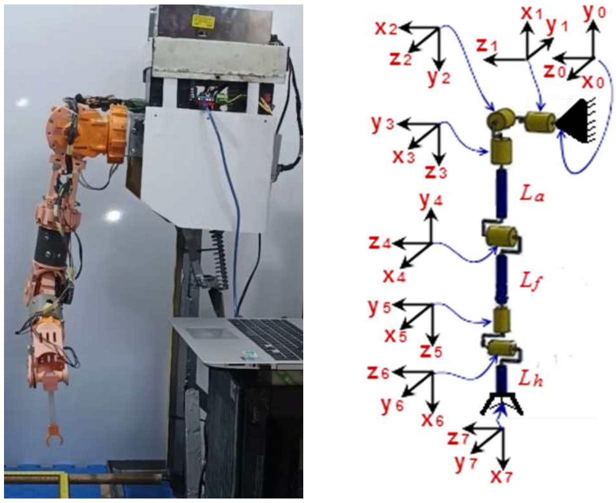

(a) (b)

Fig.4: Right upper limb of a bipedal robot and assignment of frames according to the DH convention. a. Image of the robot arm. b. inematic chain of the robot arm [7].

In this work, the following assumptions are considered:

- The shoulder, with its 3 degrees of freedom (3DOF), has its rotation axes intersecting at the same point. Therefore, the rotational movement of the shoulder can be treated as a single geometric point.

- Similarly, the same assumption is applied to the wrist, which has 2 DOF.

Fig. 5 depicts a geometric parametrization of the robot (geometric entities) that will be used in the process of solving the IKM.

The strategy to solve the inverse geometric problem is divided into two phases:

- the first phase involves in determining the geometric entities that allowed the determination of the vectors defining each joint.

- The second phase focuses on determining the angles of each joint.

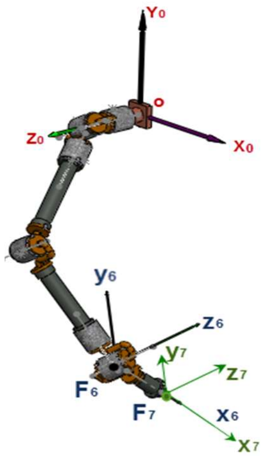

(a)

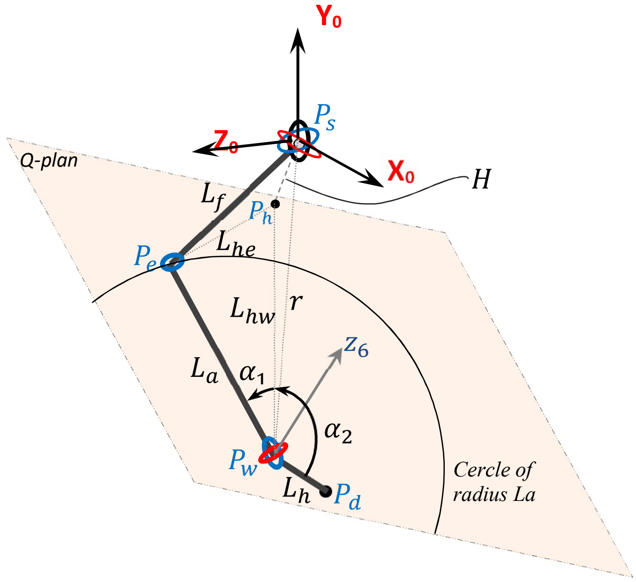

(b)

Fig.5: Geometric parametrization of a right upper limb of a bipedal robot. a. Robot configuration with assignment of main frames. b. Geometric entities [7].

a) *Calculation of Geometric Entities of the Robot*

To do this, the following strategy is adopted:
- Determine the position of the wrist.
- Determine the position of the elbow.

The position of the wrist is given by (8).

$$\overrightarrow{OP_w} = \overrightarrow{OP_d} - L_h \overrightarrow{S_6} \tag{8}$$

where:

$\overrightarrow{OP_w} = (P_{wx}, P_{wy}, P_{wz})^T$ and $\overrightarrow{OP_d} = (P_{dx}, P_{dy}, P_{dz})^T$ respectively are the coordinates of the wrist position and the desired position of the end effector (hand). L_h is the length between wrist and hand. We define the circle of the center P_w (wrist position) and radius L_f (forearm length) on the plane *Q-plan* that is defined by

$$\overrightarrow{OP_c} = \overrightarrow{OP_w} + L_f\cos(\varphi)\overrightarrow{S_6} + L_f\sin(\varphi)\overrightarrow{N_6} \tag{9}$$

Where:

$\overrightarrow{OP_e} = (P_{ex}, P_{ey}, P_{ez})^T$ and $\overrightarrow{OP_w} = (P_{wx}, P_{wy}, P_{wz})^T$ are, respectively,the coordinates of the circumference of the circle and the center of the circle. $\overrightarrow{S_6}$ and $\overrightarrow{N_6}$ are, respectively, the unit vectors of the x_6-axis et y_6-axis. And φ is the angle between x_6-axis and $\overrightarrow{V_{we}}$ (vector defined by wrist and elbow). Thus, from (9), the position of the elbow is determined by the vector of coordinates given in (10).

$$\overrightarrow{OP_c} = \overrightarrow{V_{oe}} = \left(P_{ex}\ ,P_{ey}\ ,P_{ez}\right)^T \tag{10}$$

By determining the necessary geometric entities, we proceed for identification of joint angles.

b) *Calculation of Arm Joint Angles*

Geometrically, three vectors (Fig.6), from which two mathematical arguments (arg1, arg2) are expressed and will be used in (6), describe each joint angle.

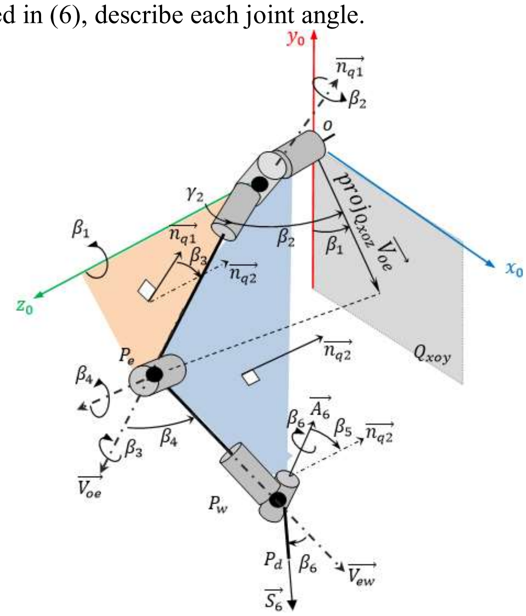

Fig.6: Vectorial description of arm's joint angles.

- *Joint angle* β_1

The vectors define the angle:

$proj_{Q_{xoz}}\overrightarrow{V_{oe}}$, $-\overrightarrow{y_0}$ and $\overrightarrow{z_0}$. Given that :

$$det_{\beta_1} = \det(-\overrightarrow{y_0}, proj_{Q_{xoz}}\overrightarrow{V_{oe}}\ ,\overrightarrow{z_0}\ )$$

$$cos(\beta_1) = -\overrightarrow{y_0}\ .proj_{Q_{xoz}}\overrightarrow{V_{oe}}$$

Hence

$$\beta_1 = \text{atan2}\left(det_{\beta_1}, cos(\beta_1)\right) \tag{11}$$

- *Joint angle* β_2

From Fig.6, β_2 can be written as follows:

$\beta_2 = \frac{\pi}{2} - \gamma_2$

γ_2 is expressed by the formula bellow:

$\gamma_2 = atan2\left(det_{\gamma_2}, \cos(\gamma_2)\right)$.

Where

γ_2 is the angle between $\overrightarrow{z_0}$ and $\overrightarrow{V_{oe}}$

$\overrightarrow{z_0}$ *and* $\overrightarrow{V_{oe}}$ are, respectivelly, the cosine vector of z_0-axis of fixed frame at schoulder and the vector between schoulder and elbow points.

$$\cos(\gamma_2) = \overrightarrow{z_0}.\overrightarrow{V_{oe}} \text{ and } det_{\gamma_2} = det\left[\overrightarrow{n_{q1}}\,\overrightarrow{z_0}\,\overrightarrow{V_{oe}}\right]^T$$

So

$$\beta_2 = \frac{\pi}{2} - \operatorname{atan2}\left(det_{\gamma_2}, \cos(\gamma_2)\right) \tag{12}$$

- *Joint angle* β_3

The arguments for the angle β_3 are given bellow

$$\cos(\beta_3) = \overrightarrow{n_{q1}}.\overrightarrow{n_{q2}} \text{ and } det_{\beta_3} = det\left[\overrightarrow{V_{eo}}\,\overrightarrow{n_{q1}}\,\overrightarrow{n_{q2}}\right]^T.$$

So

$$\beta_3 = \operatorname{atan2}\left(det_{\beta_3}, \cos(\beta_3)\right) \tag{13}$$

Where

$\overrightarrow{n_{q1}}$ and $\overrightarrow{n_{q2}}$ are respectivelly, the normal vectors of Q_1-plan and Q_2-plan. The first one is defined by two vectors $\overrightarrow{z_0}$ and $\overrightarrow{V_{oe}}$. The second one is defined by two vectors $\overrightarrow{V_{oe}}$ and $\overrightarrow{V_{ew}}$.

- *Joint angle* β_4

The joint angle β_4 is an angle between $\overrightarrow{V_{oe}}$ (arm) and $\overrightarrow{V_{ew}}$ (forearm) as illustrated in Fig.6. Where $\overrightarrow{n_{oe}}$ and $\overrightarrow{n_{ew}}$ respectively are the normalized vectors of $\overrightarrow{V_{oe}}$ and $\overrightarrow{V_{ew}}$.

The arguments for the angle β_4 are: $\cos(\beta_4) = \overrightarrow{n_{oe}}.\overrightarrow{n_{ew}}$ and $det_{\beta_4} = det\left[\overrightarrow{n_{q1}}\,\overrightarrow{n_{oe}}\,\overrightarrow{n_{ew}}\right]^T$

So

$$\beta_4 = \operatorname{atan2}\left(det_{\beta_4}, cos(\beta_4)\right) \tag{14}$$

- *Joint angle* β_5

The joint angle β_5 is defined between the vectors $\overrightarrow{n_{q2}}$ and $\overrightarrow{A_6} = (a_x, a_y, a_z)^T$ of the z_6--axis as illustrated in Fig.6. Thus, β_5 is expressed in (15) as follows

$$\beta_5 = atan2\left(det_{\beta_5}, cos(\beta_5)\right) \tag{15}$$

Where

$$\cos(\beta_5) = \overrightarrow{n_{q2}}\,.\,\overrightarrow{A_6} \text{ and } det_{\beta_5} = det\left[\overrightarrow{n_{we}}\overrightarrow{n_{q2}}\overrightarrow{A_6}\right]^T.$$

- *Joint angle* β_6

The joint angle β_6 is the angle between the forearm and the hand of the robot. It is defined by the vectors $\overrightarrow{V_{ew}}$ (elbow-wrist) and $\overrightarrow{V_{wd}}$ (wrist-desired position) (Fig.6). Thus, β_6 is the angle between two vectors: $\overrightarrow{n_{ew}} = \frac{1}{|\overrightarrow{V_{ew}}|}\overrightarrow{V_{ew}}$ and $\overrightarrow{S_6} = (s_x, s_y, s_z)^T$. Consequently, the two arguments of β_6 are given below

$$\cos(\beta_6) = \overrightarrow{n_{ew}}\,.\,\overrightarrow{S_6} \text{ and } det_{\beta_6} = det\left[\overrightarrow{A_6}\overrightarrow{n_{ew}}\overrightarrow{S_6}\right]^T.$$

Finally, β_6 is expressed by (16)

$$\beta_6 = atan2\left(det_{\beta_6}, cos(\beta_6)\right) \tag{16}$$

4) Inverse Kinematic Modeling of the Lower Limb (Leg).

The leg, with 06 degrees of freedom (right or left), is composed of three links that are connected to each other (Fig.7). After calculating the position of the ankle and the knee, we proceed to identify the joint angles of this latter.

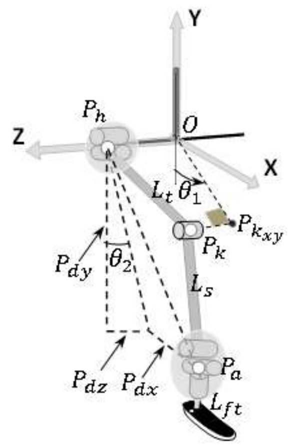

Fig.7: Geometric description of θ1 and θ2

- *Joint angle* θ1

The joint angle θ1 can be calculated via (17) using (3) with the help of the following three vectors: $\overrightarrow{OZ}$, $\overrightarrow{OY}$, $\overrightarrow{OP_{kxy}}$.

$$\theta_1 = a\tan 2\left(\det_{\theta_1},\quad \cos\theta_1\right) \tag{17}$$

Where

$\det_{\theta_1} = \det(\overrightarrow{OZ}, \overrightarrow{OP_{kxy}}, -\overrightarrow{OY})$

$\cos\theta_1 = \cos(\overrightarrow{OP_{kxy}}, -\overrightarrow{OY})$

$\overrightarrow{OZ} = (0,0,1)$, $\overrightarrow{OY} = (0,1,0)$ two units vectors of the hip's frame.

$\overrightarrow{OP_{kxy}} = (P_{kx}, P_{ky}, 0)$ is the projection of knee's point on *xy-plane* that is defined by axes $\overrightarrow{OX}$ and $\overrightarrow{OY}$ of the hip's frame.

- *Joint angle* θ2

From Fig.7, these three points: P_h(hip's point) , P_k (knee's point) , and P_a (ankle's point) belong to the same plane which is initially parallel to *XY-plane* can move laterally only by the joint θ2.

Therefore, the joint angle θ2.can be calculated by (18) as follows

$$\theta_2 = \arccos\left(\frac{P_{az}}{P_{ay}}\right) \tag{18}$$

Where

$\left(P_{ax}, P_{ay}, P_{az}\right)^T$ are the coordinates of the vector $\overrightarrow{V_{oa}}$ that is defined between the origin of hip's frame and the ankle.

- *Joint angle* θ3

From Fig.8, the triangular formula bellow is defined

$$r_{ha}^2 = L_s^2 + L_l^2 - 2\, L_s\, L_l\, \cos\alpha$$

Where

$r_{ha} = P_{ax}^2 + P_{ay}^2 + P_{az}^2$

L_s: length of the shin.

L_l: length of the leg.

From the above equality, the angle α (between two links: leg and shin) is expressed in (19) bellow

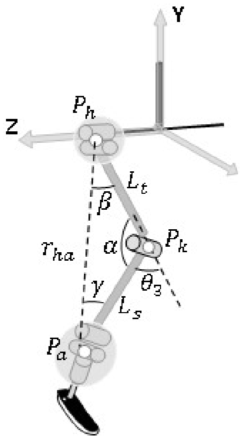

Fig.8: Geometric description of θ3.

$$\alpha = \arccos\left(\frac{r_{ha}^2 - L_{tb}^2 + L_J^2}{2\, L_{tb}\, L_J}\right) \tag{19}$$

Therefore, from Fig.8 and using (19), θ3 is obtained through (20).

$$\theta_3 = \pi - \alpha \tag{20}$$

- *Joint angle* θ4 *and* θ5

A new orthonormal frame $F_A(A, x_A, y_A, z_A)$ is defined at ankle point, where the position of L_f will be treated as a case of spherical coordinates by θ_4 and θ_5 (Fig.9).

Let P_Q be the plane by the normal vector $\overrightarrow{n_{ka}} = (a, b, c)^T$ expressed in (21)

$$P_Q\colon a\,x + b\,y + c\,z + D = 0 \tag{21}$$

Where

$D = a\,P_{kx} + b\,P_{ky} + c\,P_{kz}$

And the constants a, b, c are the components of normal vector $\overrightarrow{n_{ka}}$ written in (22)

$$\overrightarrow{n_{ka}} = \frac{1}{\sqrt{V_{kax}^2 + V_{kay}^2 + V_{kaz}^2}}\left(V_{kax}, V_{kay}, V_{kaz}\right) \tag{22}$$

Given that : $\overrightarrow{n_{ka}}$: Normal vector of the plane P_Q deduced from the vector $\overrightarrow{V_{ka}}$ defined by the points of the knee and the ankle.

Using (21) and (22), the axes of the new orthonormal frame $F_A(A, x_A, y_A, z_A)$ are defined bellow

$\overrightarrow{x_A} = (x1_A, x2_A, x3_A)$: $\overrightarrow{n_{ka}} = (a, b, c)^T$: Normal vector of the plane P_Q

$\overrightarrow{z_A} = (z1_A, z2_A, z3_A)$: $proj_{P_Q}\widehat{Z_0}$: Projection of $\widehat{Z_0}$ onto the plane P_Q

$\overrightarrow{y_A} = (y1_A, y2_A, y3_A)$: Cross product of $proj_{P_Q}\widehat{Z_0}$ and $\overrightarrow{n_{ka}}$

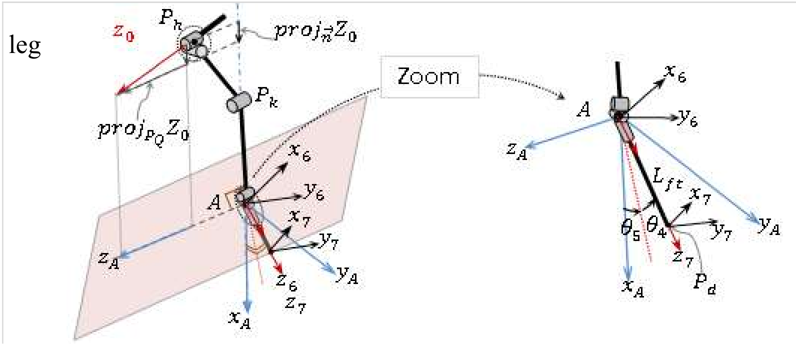

Fig.9: Geometric description of θ4 and θ5 into the new frame $R_A(A, x_A, y_A, z_A)$.

Conseauently, the new frame $F_A(A, x_A, y_A, z_A)$ can be described into the hip's frame by the following matrix.

$$T_{ha} = \begin{bmatrix} x_{A1} & y_{A1} & z_{A1} & P_{Ax} \\ x_{A2} & y_{A2} & z_{A2} & P_{Ay} \\ x_{A3} & y_{A3} & z_{A3} & P_{Az} \\ 0 & 0 & 0 & 1 \end{bmatrix}$$

Thus, one can express the determination of the coordinates of point Pd in the new frame FA as follows

$${}^{R_A}P_d = \left[T_{ha}\right]^{-1}\, {}^{R_0}P_d \tag{23}$$

Finally, from the coordinates ${}^{R_A}P_d$ given by (23), the determination of the rotational joints θ_4 and θ_5 is carried out using the spherical coordinates of the radius L_f, the foot link, (or $\boldsymbol{L_{ad}}$, the length between the ankle and the desired position).

$$\begin{cases} {}^{R_A}P_{dx} = L_f\, \cos\theta_4 \\ {}^{R_A}P_{dy} = L_f\, \sin\theta_4 \cos\theta_5 \\ {}^{R_A}P_{dz} = L_f\, \sin\theta_4 \sin\theta_5 \end{cases} \tag{24}$$

Finally, from (24), θ_4 and θ_5 can be expressed by (25) and (26) bellow

$$\theta_4 = \arccos\left(\frac{{}^{R_A}P_{dx}}{L_P}\right) \tag{25}$$

And

$$\theta_5 = \arctan\left(\frac{{}^{R_A}P_{dz}}{{}^{R_A}P_{dy}}\right) \tag{26}$$

- *Joint angle* θ6

The last rotational joint θ_6 (See Fig.10) of the leg can be obtained through a simple matrix calculation given by (27).

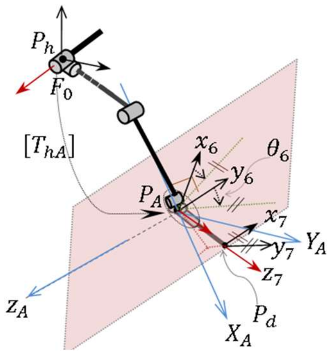

Fig.10: Geometric definition of θ_6 of the leg.

$$
\begin{aligned}
&{}^{0}T_7 = {}^{0}T_4\, {}^{4}T_5\, {}^{5}T_6\, {}^{6}T_7 \\
\Rightarrow\ &{}^{6}T_7 = \left[{}^{5}T_6\right]^{-1} \left[{}^{4}T_5\right]^{-1} \left[{}^{0}T_4\right]^{-1} \left[{}^{0}T_7\right]
\end{aligned}
\tag{27}
$$

Where

${}^{0}T_7$: Matrix of the given situation of the end effector (foot position).

${}^{0}T_4$: Matrix of the situation of the frame $\boldsymbol{R_A}$ inserted at the robot's ankle. This matrix is none other than the matrix T_{ha}

$$[{}^{0}T_4] = [T_{hA}] = [{}^{0}T_1]\,[{}^{1}T_2]\,[{}^{2}T_3]\,[{}^{3}T_4]$$

${}^{6}T_7$: Transformation matrix between R_6 and R_7 which is expressed by θ_6.

The components of the matrix ${}^{6}T_7$ are given below:

$$
{}^{6}T_7 = \begin{bmatrix} \cos\theta_6 & -\sin\theta_6 & 0 & 0 \\ \sin\theta_6 & \cos\theta_6 & 0 & 0 \\ 0 & 0 & 1 & L_P \\ 0 & 0 & 0 & 1 \end{bmatrix}
$$

Thus, (27) can be reformulated as follows:

$$
{}^{6}T_7 = \left[{}^{5}T_6\right]^{-1} \left[{}^{4}T_5\right]^{-1} \left[\ T_{ha}\right]^{-1} \left[{}^{0}T_7\right] \tag{28}
$$

By identifying the terms in (28), θ_6 can be easily found in (29).

$$
\theta_6 = a\tan 2\left(\sin\theta_6, \cos\theta_6\right) \tag{29}
$$

Note.

Due to symmetry of robot, the same modeling procedure used for the right leg will be applied to the left leg.

IV. PARAMETRICS EQUATIONS OF END-EFFECTOR'S TRAJECTORIES

In order to verify the obtained results of the used approach in solving IK problem of biped robot, we plan to conduct simulations using Matlab software and leveraging the solutions the previously obtained results. However, it is necessary to determine the set of trajectories for the various members of the robot.

A. The trajectory of the hip.

The trajectory of the hip is defined by the three parametric equations below: (30), (31) and (32)

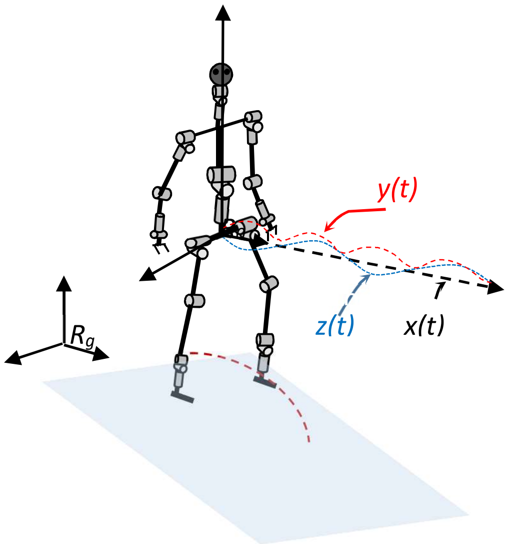

Fig.11: Trajectory hodograph of the hip.

$x_h(t)$: Linear equation on x-axis.

$$
x_h\left(t\right) = at + b \tag{30}
$$

$y_h(t)$: Polynomial equation of degree five in the plane (o:x,y).

$$
y_{hs}\left(t\right) = k_0 + k_1 t + k_2 t^2 + k_3 t^3 + k_4 t^4 + k_5 t^5 \tag{31}
$$

$z_h(t)$: Sinusoidal equation in the plane (o: x, z)

$$
z(t) = A_z \sin\left(a\left(x(t) - x_0\right)\right) \tag{32}
$$

B. Trajectory of the foot in flight.

Let $X_{pS}(t)$ and $X_{pd}(t)$ denote the functions expressing respectively the trajectories of the simple support Phase (SSP) and the double support phase (DSP). Given that.

$X_{PS}(t):\left\{\, x_{ps}\left(t\right), y_{ps}\left(t\right), z_{ps}\left(t\right)\right\}$ and

$X_{Pd}(t):\left\{\, x_{pd}\left(t\right), y_{pd}\left(t\right), z_{pd}\left(t\right)\right\}$

Where

$\left\{x_{ps}\left(t\right), y_{ps}\left(t\right), z_{ps}\left(t\right)\right\}$ and $\left\{x_{pd}\left(t\right), y_{pd}\left(t\right), z_{pd}\left(t\right)\right\}$ denote its parametric equations expressed in the principal frame. Howerver, the double support phase represents 20% of the single support phase [9].

$x_h(t)$: Cubic polynomial equation.

$$
x_{ps}\left(t\right) = a_0 + a_1 t + a_2 t^2 + a_3 t^3 \tag{33}
$$

$y_h(t)$: Quintic polynomial equation.

$$
y_{ps}\left(t\right) = b_0 + b_1 t + b_2 t^2 + b_3 t^3 + b_4 t^4 + b_5 t^5 \tag{34}
$$

zh(t) : no movement of the foot along the z-axis.

$$z_p\left(t\right)=0 \tag{35}$$

C. Trajectory of the upper limbs.

The two upper limbs swing in an alternating and opposite manner between a forward and backward movement. (Fig. 12).

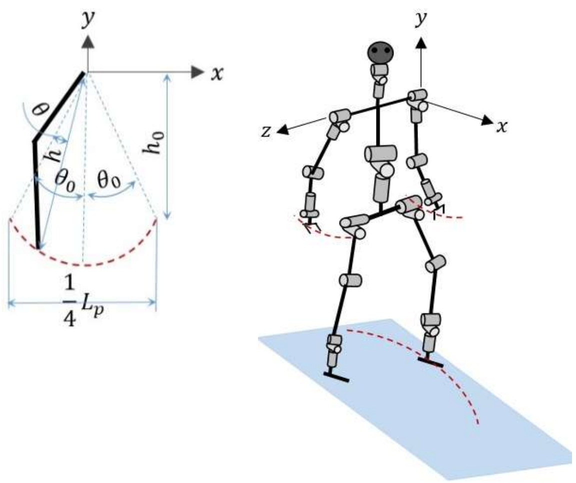

a b

Fig.12: Hodograph of the robot's upper limbs.

Their parametric equations with respect to the shoulder frame are expressed by the following equations

xm(t) : Linear equation along the x-axis.

$$x_m\left(t\right)=at+b \tag{36}$$

ym(t) : Cosinusoidal equation

$$y_m(t)=-R\cos\theta(t) \tag{37}$$

Where:

$R \leq L_a + L_{fa}$

$\theta(t)=\dfrac{2}{T_c}\theta_0\, t-\theta_0$: Linear equation.

zh(t) : No movement of the foot along the z-axis.

$$z_m\left(t\right)=0 \tag{38}$$

Note.

All the constants in the parametrics equations (30-38) of trajectories are detrmined with respect to condition and exigences of walk of robot. Primarlly, bellow parameters are used:

L_p : Step length.

T_s : Step period for the SSP.

T_d : Step period for the DSP.

H_f : Maximum height of the flight foot.

S_f : Corresponding abscissa to H_f.

H_{max} and H_{min} : Respectively, maximum and minimum height of the hip .

H_{x_0} : Hip initial position on *x-axis*.

V. Simulation of inverse kinematic model of the biped robot

The simulations are conducted on the bipedal robot to validate the IKM solutions obtained previously. The bipedal robot should walk correctly by following the trajectories imposed on its gait-members (hip, upper limbs, and lower limbs).

Simulation parameters values.

- Lengths of links of robot are given in Tab.1.
- Maximum and minimum height of the hip respectively : h_{max} = 0.69; h_{min} = 0.66[*m*]
- Maximum foot height in flight: H_f = 0.10[*m*].
- One-step period : T_p=Ts+Td =1.3+0.3 =1.6[s]
- Average time corresponding to H_f : $T_m = T_s / 2$[s]
- Step length: L_p = 0.32[*m*].
- Final position of the hip in DSP : $H_{xf} = 0.5.Lp + H_{x_0}$. [*m*]

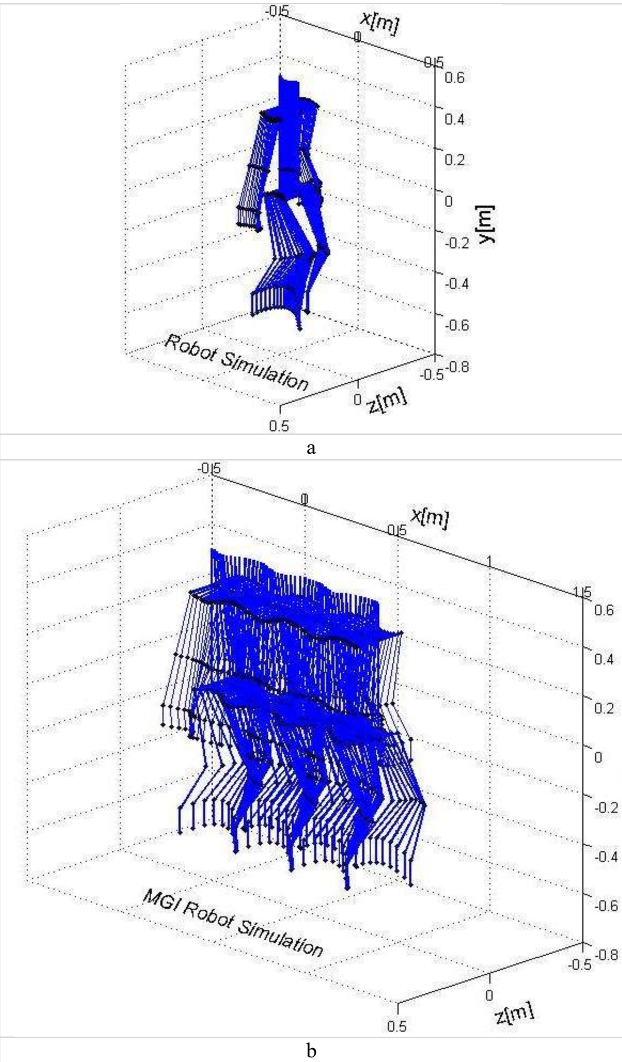

a

b

Fig.13: Simulation of the inverse kinematic model of the robot (IKM). a. simulation of a single step. b. simulation of six successive steps.

These simulations, depicted in Fig.13, demonstrates that the developed solutions in solving IKM presented above is correct and accurate.

VI. General conclusion

An attractive and basic topic in robotics was developped in this work. An application on biped robot with 30 degree of freedom was presented. Topologically, this robot consists of a central mechanism (the trunk), two upper limbs (right arm and left arm), two lower limbs (right leg and left leg), and a neck-head mechanism.

This work extends to inverse kinematic modeling by employing an alternative approach based on vectors and the geometric environment of the robot. This approach offers a significant advantage in obtaining solutions through linear and uncoupled equations. In fact, all joint variables of the bipedal robot with 30 degrees of freedom are determined using this approach. Simulations were conducted and the obtained results align with the expected goals. Thus, this work contributes to the advancement of knowledge in the field of robotics.

REFERENCES

[1] A. Singh, A. Singla. Kinematic Modeling of Robotic Manipulators. Proc. Natl. Acad. Sci., India, Sect. A Phys. Sci. pp.303–319, 2017. DOI: 10.1007/s40010-016-0285-x

[2] M.Menad, z. Derouiche, Z-A. Foitih, W. Nouibat. Kinematic modeling of a humanoid robot with 18 DOF in a virtual environment. IEEE 3rd Inter. Conf. on Innov. Comp. Tech. (INTECH 2013).2013. DOI: 10.1109/INTECH.2013.6653656

[3] W-A. Bin Wan Daud, W. Faizura, M. Azmi Adly, I. Elamvazuthi, M. Begam. Kinematic modeling of humanoid arm. IEEE Inter. Conf. on Intell. and Adv. Syst.. 2011. DOI: 10.1109/ICIAS.2010.5716210

[4] W. Dewandhana, K. I. Apriandy, B. S. B. Dewantara, D. Pramadihanto. Forward Kinematics with Full-Arm Analysis on "T-FLoW" 3.0 Humanoid Robot. International Electronics Symposium. IES) 2021.

[5] Y.Liu, J. Weng, F. Wang, J. Tang et all. Design and Control of the Biped Robot HTY. Springer nature Singapore. ICIRA 2023, LNAI 14270, pp. 404–415, 2023.

[6] J. Lee and H-M. Joe. Design of Humanoid Robot Foot to Absorb Ground Reaction Force by Mimicking Longitudinal Arch and Transverse Arch of Human Foot. 2023. Springer International Journal of Control, Automation, and Systems 21(11) (2023) 3519-3527

[7] N. Hadidi, M. Bouaziz, C. Mahfoudi, M. Zaharuddin. Geometric Approach to Solve Inverse Kinematics of Six DoF Robot With Spherical Joint. Acta polytechnica, 63(5), pp. 326–346. Https://doi.org/10.14311/ap.2023.63.0326

[8] T. Lyche. A short review of linear algebra. Numerical Linear Algebra and Matrix Factorizations. Springer Nature, Switzerland AG:15-18, 2020. https://doi.org /10.1007/978-3-030-36468-7-1.

[9] Z. Tang, C. Zhou & Z. Sun. Trajectory Planning for Smooth Transition of a Biped Robot. IEEE Intern. Conf. of Robotics & Automation. Taiwan.. vol.2. Issue: 14-19 . pp. 2455- 2460. 2003

Nacer Hadidi was born in Bouira, Algeria, in 1980. He received the Engineer's degrees in Mechanical Engineering from University of Blida Saad Dahleb in 2004, the Magister degree from Ecole Nationale Polytechnique, Algiers, in 2010. He is currently a Ph.D student at the Mechanical Department at the same establishement. His interest research area is mechanisms and robotics. He is an assistant professor at Ecole Nationale Superieure des Technologies avancées since 2012 in Algiers.

Chawki Mahfoudi is a Professor at Department of mechanical engineering of university of Larbi ben M'hidi in Oum El Bouaghi, Algeria. He held differents positions in this University. He was the head of mechanical engineering department. Currently, He is the Dean of the same university. His interest research is robotics and control.

Mohamed Bouaziz was a Professor at Departement of Mechanical engineering at Ecole Nationale Polytechnique, Algeria. He spend more than 30 years at Ecole Nationale Polytechnique, teaching and supervising.

Zaharuddin Mohamed is a Professor at Universiti Technologi Malaysia (UTM), School of Electrical Engineering. He graduated and obtained bachelor degree in Electrical, Electronics and Systems Engineering at Universiti Kebangsaan Malaysia, Malaysia, in 1993. In 1995, He got Master of Science in Control Systems Engineering from the University of Sheffield, UK. He conducted his PhD at the same university in Control Engineering in UK, in 2003. His interest area of research is control of under-actuated systems, robotics, and mechatronics.

Ahcene Bouzida was born in Medea, Algeria, in 1981. He performed his study at Department of Electrical Engineering at Ecole Nationale Polytechnique of Algiers, Algeria, where He graduated and obtained his Engineer, Master and PhD diploima respectivelly in 2004, 2007 and 2011. Now, He is a Professor at University of Bouira-M'hand Oulhadj, department of electrical engineering.

Friction Stir Welding of AZ31 Mg Alloy: Microstructure, Micro hardness and Electrochemical Behavior

Khawla Amara, Mabrouk Bouabdallah, Riad Badji, and Mouloud Aissani

Abstract− In this investigation, rolled plates of AZ31 Mg alloy were successfully friction-stir welded. It was found that the process leads to the microstructural refinement in the NZ due to the dynamic recrystallization with a global microstructural heterogeneity through the weld. The maximum microhardness values were attributed to the finest microstructure. The obtained results revealed that the cathodic behavior of the grain boundaries improves the corrosion resistance of the NZ. Thus, the corrosion resistance enhancement was ascribed to the most homogeneous microstructure and the finest grains.

***Keywords*− AZ31 magnesium alloy, electrochemical behavior, friction stir welding, micro-hardness, microstructure.**

NOMENCLATURE

FSW	Friction stir welding.
NZ	Nugget zone.
BM	BM.
HAZ	Heat-affected zone.
TMAZ	Thermomechanically affected zone.
IMC	Intermetallic compound.
OCP	Open circuit potential
PDP	Potentiodynamic polarization
EIS	Electrochemical impedance spectroscopy

I. INTRODUCTION

Owing to the exceptional features of lightness, specific resistance, and damping capacity, magnesium and its alloys are extensively employed throughout the automotive [1] and aerospace [2]. Even so, the conventional welding processes involving fusion reveal the poor weldability of Mg alloys with defects such as hot cracks, porosity and high residual stresses [3]. To ameliorate joint efficiency, FSW can effectively alternate the conventional welding processes and become a more efficient joining process [4],[5]. Further, numerous studies have been carried out on the microstructure, crystallographic texture, and mechanical properties of the AZ31 FSW joint [6]–[8]. The FSW microstructures are characterized by recrystallized fine grain, tiny second phases with uniform distribution, and dominance of the basal texture in the NZ [9], [10] [11]. This characterized microstructure contributes to the enhancement of the ultimate tensile strength, and microhardness, and decreases the residual stress level [8]. Besides, numerous papers reported that grain refinement of the FSW AZ31 joint significantly improves its corrosion resistance [12] whereas others denied the effect of grain boundary [13] and attributed the corrosion resistance to the cathodic Al-Mn IMCs [13], [14]. Thus, this study aims to examine the microstructure in the area that has undergone the most significant evolution NZ and TMAZ compared to the BM. The purpose of this investigation is to characterize the microstructural evolution and related electrochemical behavior in the BM, TMAZ, and NZ zones which experienced crucial microstructural changes in a friction stir welded joint of AZ31 magnesium alloy.

Manuscript received April 27, 2023; revised July 5, 2024.

K. Amara is with Ecole Nationale Polytechnique, Algiers, ALGERIA (e-mail: amara_khawla@hotmail.fr).

M. Bouabdallah was with Ecole Nationale Polytechnique, Algiers, ALGERIA(e-mail: mabrouk.bouabdallah@g.enp.edu.dz).

R. Badji is with the Research Center in Industrial Technologies, Algiers, ALGERIA (e-mail: r.badji@crti.dz)

M. Aissani is with the Research Center in Industrial Technologies, Algiers, ALGERIA (e-mail:m.aissani@ crti.dz)

Digital Object Identifier (DOI): 10.53907/enpesj.v4i1.198

II. MATERIALS AND EXPERIMENTAL PROCEDURES

The material used in this study is an 8 mm thick rolled plate of AZ31 Mg alloy with a nominal chemical composition (Mg - 2.9Al - 0.87Zn - 0.37Mn). The plates were prepared in the desired dimensions (200 x 100) mm^2 and friction stir welded at a rotational speed of 950 rpm and a welding speed of 43 mm/min, as described previously [15].

The joint has been cut perpendicularly to the welding direction. Microstructure observation was realized on a transversal cross-section. The samples underwent a metallographic preparation consisting of mechanical polishing followed by a finishing polishing by a diamond suspension and eventually etched with Picral reagent (4.2 g picric acid, 10 ml acetic acid, 70 ml ethanol and 10 ml distilled water). The microstructures of the BM, TMAZ, and NZ were observed using (Nikon Elipse LV100ND) optical microscope and a (ZEISS – GEMINI 300) scanning electron microscope.

The micro hardness test was performed on the Vickers hardness tester (Buehler Wilson 3500) with an applied load of 100 g force and a dwell time of 20 s. The micro hardness profile was taken at the mid-thickness of a transversal cross-section; the distance between every two points is 1 mm.

Electrochemical measurements were performed in an electrochemical cell with three electrodes: working electrodes (BM, TMAZ, and NZ with an exposure area of 0.25 cm^2), an auxiliary electrode (platinum grid) and a reference electrode (SCE Ag/AgCl), connected to AMETEK-PARSTAT 3000 potentiostat, the data were collected and managed using VersaStudio software. The working electrodes were immersed in a 3.5 wt% NaCl solution at room temperature for 1 h to reach the open circuit potential (OCP). Electrochemical impedance spectroscopy (EIS) measurements were carried out in the frequency range from 20 kHz to 0.01 Hz and Potentiodynamic polarization (PDP) was conducted in the potential range of -250 mV to +250 mV approximately the OCP with a scan rate of 0167 mV.s^{-1}.

III. Results

Fig. 1.a shows a typical macrographic view of the AZ31 FSW joint from a transversal cross-section. Morphological characterization by optical microscope revealed the distinction of three zones, in addition to the BM, across the joint namely: NZ, TMAZ and HAZ depicted in the center area of the joint, the width of the NZ was approximately 7 mm. Furthermore, the extent of TMAZ on the retreating side (RS) is slightly greater than that on the advancing side (AS) due to the strain accumulated in RS during friction stir welding [16]. To estimate the maximum temperature calculated during FSW, the following empirical law can be used [10]:

$$\frac{T}{Tm} = k\left(\frac{W^2}{V}.\frac{1}{10^4}\right)^{\alpha} \qquad (1)$$

Where: Tm: melting temperature of the AZ31 alloy (610°C), T: maximum temperature reached during FSW in the NZ, W: rotation speed, V: welding speed, K and α: constants can be considered 0.0442 and 0.8052 respectively.

The above equation indicates that rotational speed and welding speed are the main contributors to heat generation during the FSW process. Thus, the temperature might reach high values (about 500°C) in the NZ.

Fig. 1-b displays a twinned microstructure of the BM, it consists both of relatively coarse and fine equiaxed grains with an average grain size of 10 µm. Fig. 1-c represents the microstructure of the NZ, it is characterized by fine equiaxed grains with an average grain size of 6.4 µm. The nugget zone has undergone a grain refinement as was expected [8] due to the dynamic recrystallization, under the combined effects of the excessive heat input and the severe plastic deformation. The TMAZ, shown in Fig. 1-d, contains both coarse grains elongated in the stirring direction (i.e. material flow), and some newly recrystallized grains were found at the grain boundary because of moderate plastic deformation at a relatively low temperature that this zone has experienced partially. This result is in good accordance with the analysis of the available literature [11]. The average grain size of the TMAZ is about 13 µm. Fig. 1.e represents the microstructure of HAZ. It is characterized by its similarity to the BM with a moderate presence of the IMCs, the twins have been removed because of the elevated temperature in this zone.

Fig. 2 represents the SEM image of the BM, NZ, TMAZ, and HAZ respectively. According to the Energy-dispersive Spectroscopy (EDS) analysis, these particles correspond to Al_8Mn_5 intermetallic compounds with an average atomic ratio (Al at. % /Mn at. %) of 1.91, 1.6, 1.65, and 1.65 for BM, NZ, TMAZ, and HAZ respectively. During the FSW, these IMCs are fragmented and randomly distributed along the grain boundaries in polygonal shapes with an average particle size is about 2-4 µm. The elemental composition of Al_8Mn_5 is not affected by the temperature achieved during FSW due to its high melting temperature.

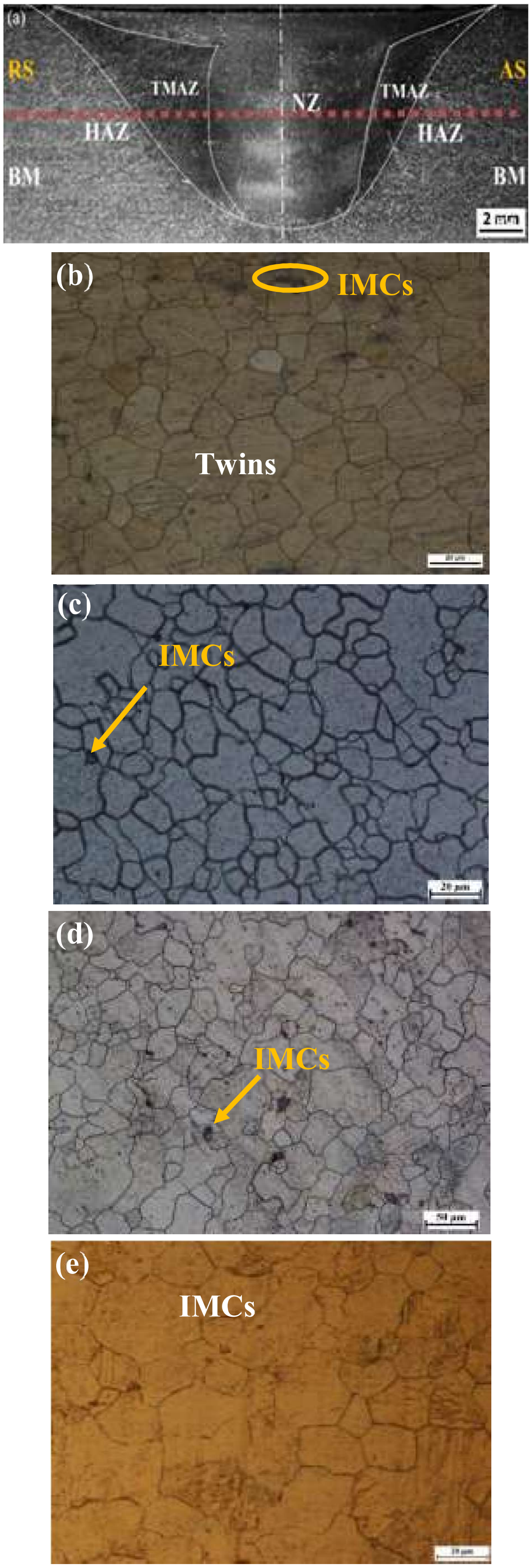

Fig. 1: Optical views of the different zones in FSW AZ31 joint (a) cross section macrostructure, (b) BM, (c) NZ, (d) TMAZ and (e) HAZ

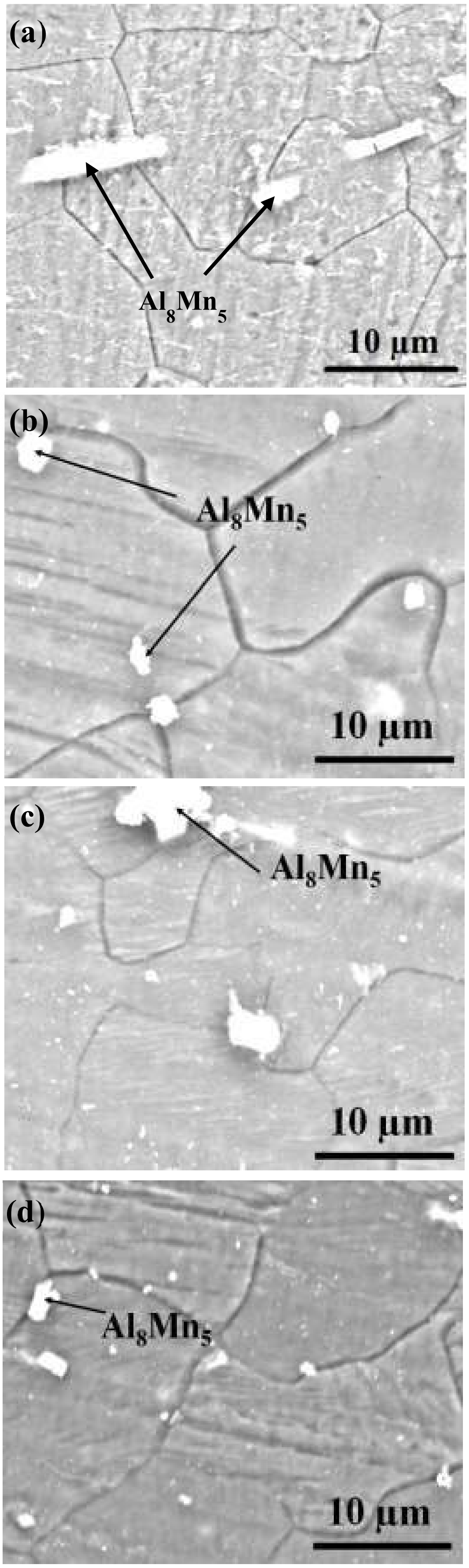

Fig. 2: SEM images of AZ31 FSW joint: (a) BM, (b) NZ, (c) TMAZ and (d) HAZ

Fig. 3 shows micro-hardness profile distribution at the midthickness of the FSW AZ31 joint. The average micro-hardness value of the BM is approximately 55 Hv.

The lowest micro hardness values were measured in HAZ at RS (~48 Hv) while the highest micro-hardness values in NZ and TMAZ were (~58 Hv). According to the Hall-Petch formula, the smaller the grain size, the higher the hardness is. The heterogeneity of the micro hardness distribution was attributed to the NZ microstructural heterogeneity. NZ underwent a high thermal input during FSW which leads to heterogeneous microstructure (fine recrystallized grains and coarse grains) while TMAZ has a higher average micro hardness compared to the other zones. This is attributed to the partial recrystallization and the high dislocation density induced by the thermo mechanical action. The presence of Al_8Mn_5 IMCs does not affect the micro hardness evolution. Such a distribution of micro hardness would be due to the unequal heat input flow and plastic deformation during FSW, which is a consequence of the heterogeneity of the microstructure.

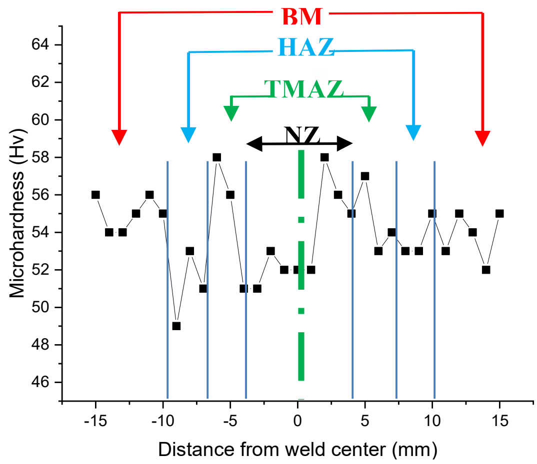

Fig. 3: Micro-hardness profile distribution of FSW AZ31 joint.

Fig. 4 and Fig. 5 summarize the electrochemical test results of BM, TMAZ, and NZ studied in a 3.5 wt% NaCl media. Fig. 4.a shows the OCP curves of the different zones of the FSW AZ31 joint. From Table I, the OCP values are classified as follows: NZ (-1.508 mV) > BM (-1.547 mV) > TMAZ (1.551 mV). Increasing the OCP value of NZ as a function of time implies the formation of a more stable oxide layer on the surface of NZ, whereas decreasing the OCP values of TMAZ and BM as a function of time may involve the destruction of the oxide layer. Thus, more positive OCP values suggest a tendency toward enhanced corrosion resistance.

Fig. 4.b displays the PDP curves of BM, TMAZ and NZ after immersion for 1 hour in 3.5 wt. NaCl. All the PDP curves present the same overall appearance, which indicates that the FSW does not affect the corrosion mechanism. These PDP curves of the NZ and TMAZ shift to the lowest current density values 17 $\mu A.cm^{-2}$ and 49 $\mu A.cm^{-2}$ respectively compared to that of the BM (52 $\mu A.cm\text{-}^{2}$). Also, the FSW seems not to affect the cathodic brunch. Nevertheless, the anodic brunch shows an inflection point corresponding to the passivity breakdown. The breakdown point Eb represents a region of intense local anodic activity that could be explained by the progressive deterioration of the oxide layer. Icorr is classified as BM<TMAZ<N. The corrosion resistance of NZ is therefore higher. This indicates that the FSW process improves the corrosion resistance of the joint regarding the BM.

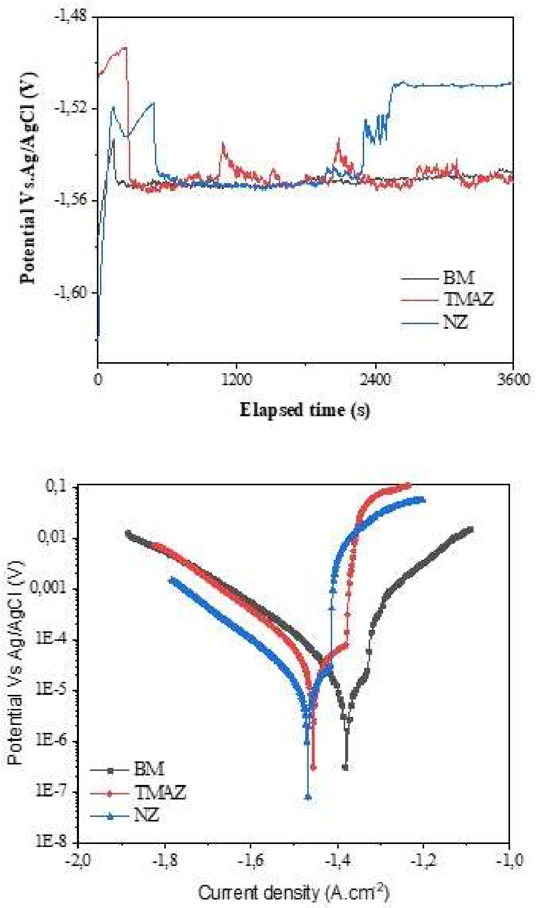

Fig. 4: Electrochemical results of the different zones in the FSW AZ31 joint in 3.5 %wt. NaCl (a) Open circuit potentiel, (b) PDP.

Table. I
POTENTIODYNAMIC POLARIZATION PARAMETERS OF THE DIFFERENT ZONES OF THE AZ31 JOINT.

	Eb (V)	*Ecorr (V)*	*Icorr (µA/cm²)*	*βc (mV)*	*βa (mV)*	*|Eb-Ecorr| (V)*	*OCP (V)*
BM	-	-1.427	52	138	-	-	-1.552
TMAZ	-1.379	-1.456	49	156	192	0.077	-1.551
NZ	-1.413	-1.468	17	160	124	0.055	-1.508

Likewise, the EIS was measured after 1 hour of immersion in 3.5 %wt. NaCl. Fig. 5.a displays the Nyquist plots of the BM, ZATM and NZ. The Nyquist plots of the BM and TMAZ consist of capacitive and inductive loops at higher and lower frequencies respectively while the Nyquist plot of the NZ consists of two capacitive loops. The loop diameter is associated with the charge-transfer resistance Rct i.e. corrosion resistance. Table II presents the Fitting parameters of Nyquist plots of the different zones in the FSW AZ31 joint in 3.5 wt% NaCl. It is concluded that the Rct values can be ranked as follows: BM (102 Ω.cm^2) < TMAZ (350 Ω.cm^2) < NZ (2093 Ω.cm^2).

The inductive loop of BM and TMAZ could be attributed to the breaking of the formed oxide layer by pitting corrosion, resulting in the dissolution of the metal in the corrosion process. The change in the inductive loop size may be indicative of a decrease in the thickness and deterioration of the oxide layer [17]. It can be suggested that the extent of the inductive loop depends on the thickness of the corrosion layer formed.

Fig 5.b and 5.c are the Bode modulus and phase respectively. The NZ shows maximum values of both Bode modulus |Z|and Bode phase, which confirms the further improvement in corrosion resistance of this zone. Furthermore, the shift in the peak position of the Bode phase confirms the deterioration of the oxide layer.

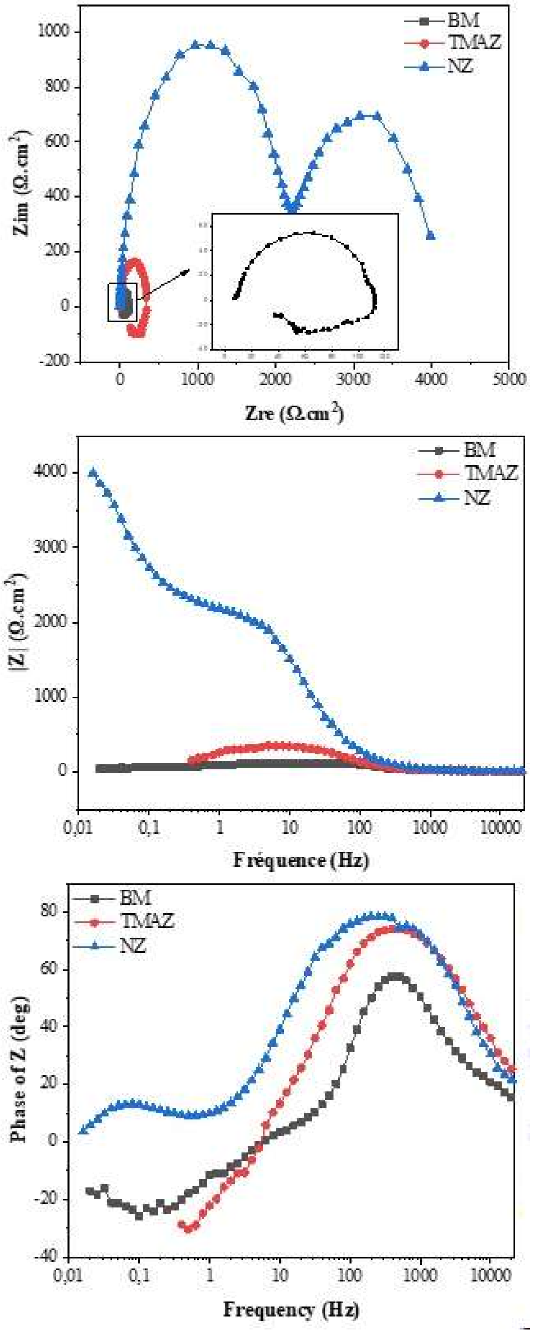

Fig. 5: electrochemical impedance spectroscopy results of the different zones in the FSW AZ31 joint in 3.5 %wt. NaCl (a) Nyquist plots, (b) Bode modulus, (c) Bode phase.

Table. II
FITTING PARAMETERS OF NYQUIST PLOTS OF THE DIFFERENT ZONES OF THE AZ31 JOINT.

	BM	*TMAZ*	*NZ*
Rs (Ω.cm²)	7.89	3.13	6.77
CPE.Y₀ (F.cm⁻² sn⁻¹)	1.53E-04	1.64E-05	9.00E-06
Freq. power n	0.9496	0.929	0.9307
C (F.cm⁻²)	1.83E-02	6.10E-04	1.06E-04
Rct (Ω.cm²)	102	350	2093
CPE.Y₀ (F.cm⁻² sn⁻¹)	-	-	1.35E-03
Freq. power n	-	-	0.8926
C (F.cm⁻²)	-	-	6.09E-04
Rct (Ω.cm²)	-	-	1911
Rf (Ω.cm²)	58	182	-
L (H.cm²)	75	122	-

Where Rs is the solution resistance, Rct is the resistance of the charge transfer, C is the capacitance of the oxide layer, and Rf is the resistance to the penetration of the Cl^- into the oxide layer.

IV. Discussions

The corrosion reactions involved in neutral and alkaline environments for magnesium and their alloys are quite similar. The global reaction can be described as follows:

$$Mg + 2H_2O \rightarrow Mg(OH)_2 + H_2\uparrow \qquad (2)$$

However, the above reaction is a general description and does not explain the involvement of the different steps of corrosion. The naturally formed oxide layer on the surface of the alloy may have high corrosion resistance. However, the same alloy may suddenly exhibit very rapid corrosion after passing a critical exposure period during which galvanic corrosion begins or after experiencing deterioration of this oxide layer. Therefore, the corrosion resistance of magnesium alloys is associated with the nature of the naturally formed oxide layer present on their surfaces and is also related to the grain boundaries and second cathodic phase present in the matrix.
The PDP curves provide the effect of the FSW on the anodic and cathodic reactions. For cathodic potential values, the Tafel curves exhibit a cathodic reaction that is characterized by hydrogen evolution as indicated by equation (3).

$$2H^+ + 2e^- \rightarrow H_2\uparrow \qquad (3)$$

For anodic potential values, the Tafel curves exhibit an anodic reaction that is assumed to represent the anodic dissolution of α-Mg according to the reaction:

$$Mg \rightarrow Mg^{2+} + 2e^- \qquad (4)$$

The corrosion resistance of the NZ, TMAZ, and the BM, were studied and compared. It was found that after FSW, ZN exhibits higher corrosion resistance than BM and TMAZ. This is in agreement with previous work that showed that NZ is more resistant than BM [12], [19]–[21], i.e. FSW improves corrosion resistance. This is mainly attributed to grain boundaries arising from grain refinement under dynamic recrystallization in NZ (low dislocation density), those grain boundaries might act as barriers against corrosion growth due to their cathodic behavior [14], [15].
NZ owns more nucleation sites for the formation of a stable and robust oxide layer due to the high density of grain boundaries [22], [23], i.e., the grain boundaries are the most favorable sites for the nucleation of an oxide layer as the grain size decreases. As described previously in the PDP results (Table I), the passivity range on the anodic brunch confirms the formation of the oxide layer on the surface of NZ and TMAZ, which is manifested by the Eb-Ecorr difference. Therefore, it is reasonable to suggest that the enhancement in corrosion resistance may result from the increase in passivity of the oxide layer as the grain size decreases [23].

V. Conclusion

The effect of the FSW on the microstructure evolution and the electrochemical behavior of the BM, TMAZ, and NZ was reported in this investigation. The conclusions drawn from this study will be presented below:

- Free-defect FSW AZ31 joints were produced with heterogeneous microstructure. Al_8Mn_5 are the main IMCs with random distribution at grain boundaries.
- Irregular distribution of the micro hardness profile due to the microstructure heterogeneity with maximum values in NZ and TMAZ (58 Hv).
- The corrosion resistance depends mainly on the cathodic grain boundaries and the oxide layer formed on the surface alloy, and the difference in the corrosion rate throughout the welded joint zones was due to the microstructure heterogeneity.

References

[1] M. K. Kulekci, « Magnesium and its alloys applications in automotive industry », Int. J. Adv. Manuf. Technol., vol. 39, no 9‑10, p. 851‑865, nov. 2008, doi: 10.1007/s00170-007-1279-2.
[2] A. H. van der Laan, R. Curran, M. J. L. van Tooren, et C. Ritchie, « Integration of friction stir welding into a multi-disciplinary aerospace design framework », Aeronaut. J., vol. 110, no 1113, p. 759‑766, nov. 2006, doi: 10.1017/S0001924000001627.
[3] F. Liu, « Microstructure, mechanical properties, and corrosion resistance of friction stir welded Mg-Al-Zn alloy thick plate joints », Weld World, p. 13.
[4] J. Zhao, F. Jiang, H. Jian, K. Wen, L. Jiang, et X. Chen, « Comparative investigation of tungsten inert gas and friction stir welding characteristics of Al–Mg–Sc alloy plates », Mater. Des., vol. 31, no 1, p. 306‑311, janv. 2010, doi: 10.1016/j.matdes.2009.06.012.
[5] S. Rajakumar, V. Balasubramanian, et A. Razalrose, « Friction stir and pulsed current gas metal arc welding of AZ61A magnesium alloy: A comparative study », Mater. Des., vol. 49, p. 267‑278, août 2013, doi: 10.1016/j.matdes.2013.01.051.
[6] W. Li, P. L. Niu, S. R. Yan, V. Patel, et Q. Wen, « Improving microstructural and tensile properties of AZ31B magnesium alloy joints by stationary shoulder friction stir welding », J. Manuf. Process., vol. 37, p. 159‑167, janv. 2019, doi: 10.1016/j.jmapro.2018.11.014.
[7] S. H. Chowdhury, D. L. Chen, S. D. Bhole, X. Cao, et P. Wanjara, « Friction Stir Welded AZ31 Magnesium Alloy: Microstructure, Texture, and Tensile Properties », Metall. Mater. Trans. A, vol. 44, no 1, p. 323336, janv. 2013, doi: 10.1007/s11661-012-1382-3.
[8] L. Commin, M. Dumont, R. Rotinat, F. Pierron, J.-E. Masse, et L. Barrallier, « Influence of the microstructural changes and induced residual stresses on tensile properties of wrought magnesium alloy friction stir welds », Mater. Sci. Eng. A, vol. 551, p. 288‑292, août 2012, doi: 10.1016/j.msea.2012.05.021.
[9] S. Mironov, T. Onuma, Y. S. Sato, et H. Kokawa, « Microstructure evolution during friction-stir welding of AZ31 magnesium alloy », Acta Mater., vol. 100, p.301‑312,nov. 2015, doi: 10.1016/j.actamat.2015.08.066.
[10] L. Commin, M. Dumont, J.-E. Masse, et L. Barrallier, « Friction stir welding of AZ31 magnesium alloy rolled sheets: Influence of processing parameters », Acta Mater., vol. 57, no 2, p. 326‑334, janv. 2009, doi: 10.1016/j.actamat.2008.09.011.
[11] J. Peng et al., « The effect of the inhomogeneous microstructure and texture on the mechanical properties of AZ31 Mg alloys processed by friction stir processing », J. Alloys Compd., vol. 792, p. 16‑24, juill. 2019, doi: 10.1016/j.jallcom.2019.04.014.
[12] F. Liu, Y. Ji, Z. Sun, J. Liu, Y. Bai, et Z. Shen, « Enhancing corrosion resistance and mechanical properties of AZ31 magnesium alloy by friction stir processing with the same speed ratio », J. Alloys Compd., vol. 829, p. 154452, juill. 2020, doi: 10.1016/j.jallcom.2020.154452.
[13] B. M. Hasani, H. Hedaiatmofidi, et A. Zarebidaki, « Effect of friction stir process on the microstructure and corrosion behavior of AZ91 Mg alloy », Mater. Chem. Phys., vol. 267, p. 124672, juill. 2021, doi: 10.1016/j.matchemphys.2021.124672.
[14] L. Lu, T. Liu, J. Chen, et Z. Wang, « Microstructure and corrosion behavior of AZ31 alloys prepared by dual directional extrusion », Mater. Des. 1980-2015, vol. 36, p. 687‑693, avr. 2012, doi: 10.1016/j.matdes.2011.12.023.
[15] K. Amara, R. Badji, M. Bouabdallah, B. Cheniti, M. Aissani, A. Haddad, A. Ziouche, « Effect of PWHT on microstructure and corrosion resistance of the nugget zone in AZ31 friction stir weld », Int J Adv Manuf Technol., vol. 123, n° 7, p. 2757–2769, dec. 2022. doi: 10.1007/s00170-022-10379-w.
[16] I. Hadji, R. Badji, M. Gaceb, et B. Cheniti, « Dissimilar FSW of AA2024 and AA7075: effect of materials positioning and tool deviation value on microstructure, global and local mechanical behavior », Int. J. Adv. Manuf. Technol., vol. 118, no 7‑8, p. 2391‑2403, févr. 2022, doi: 10.1007/s00170-021-08120-0.
[17] S. Feliu, L. Veleva, et F. García-Galvan, « Effect of Temperature on the Corrosion Behavior of Biodegradable AZ31B Magnesium Alloy in Ringer's Physiological Solution », Metals, vol. 9, no 5, p. 591, mai 2019, doi: 10.3390/met9050591.

[18] S. Feliu, L. Veleva, et F. García-Galvan, « Effect of Temperature on the Corrosion Behavior of Biodegradable AZ31B Magnesium Alloy in Ringer's Physiological Solution », Metals, vol. 9, no 5, p. 591, mai 2019, doi: 10.3390/met9050591.
[19] X. Zhang, Z. P. Cano, B. Wilson, J. R. McDermid, et J. R. Kish, « Effect of surface preparation on the corrosion resistance of friction stir linear lap welded AZ31B-H24 », Can. Metall. Q., vol. 56, no 3, p. 308�321, juill. 2017, doi: 10.1080/00084433.2017.1327500.
[20] F. Liu, Y. Ji, et Y. Bai, « Influence of multipass high rotating speed friction stir processing on microstructure evolution, corrosion behavior and mechanical properties of stirred zone on AZ31 alloy », Trans. Nonferrous Met. Soc. China, vol. 30, no 12, p. 3263�3273, déc. 2020, doi: 10.1016/S1003-6326(20)65459-0.
[21] B. Lingampalli et S. Dondapati, « Corrosion behaviour of friction stir welded ZM21 magnesium alloy », Mater. Today Proc., vol. 46, p. 1464�1469, 2021, doi: 10.1016/j.matpr.2021.03.394.
[22] D. Song, A. Ma, J. Jiang, P. Lin, D. Yang, et J. Fan, « Corrosion behavior of equal-channel-angular-pressed pure magnesium in NaCl aqueous solution », Corros. Sci., vol. 52, no 2, p. 481�490, févr. 2010, doi: 10.1016/j.corsci.2009.10.004.
[23] J. Liao, M. Hotta, et N. Yamamoto, « Corrosion behavior of fine-grained AZ31B magnesium alloy », Corros. Sci., vol. 61, p. 208�214, août 2012, doi: 10.1016/j.corsci.2012.04.039.

Khawla Amara is a Ph.D. student at the Ecole Nationale Polytechnique, Algiers, ALGERIA. She received the degree of Engineer, Master in Metallurgy from Ecole Nationale Polytechnique.

Mabrouk Bouabdallah was a Professor and research director at Ecole Nationale Polytechnique, Algiers.

Riad Badji is a Research Director at the Research Center in Industrial Technologies, Algiers.

Mouloud Aissani is a Research Director at the Research Center in Industrial Technologies, Algiers.

Renewables in the Energy Mix of Algeria, a pledge for food security

Saliha Haddoum, Hocine Bennour, and Toudert Ahmed Zaid

Abstract− This paper examines the renewables potential in the energy mix of Algeria with a special insight to bioenergy and food security. In recent years, and at global scale, bioenergy was seen as the leading renewable energy source. That contribution was particularly consistent with long-term climate targets. The 2015-updated version of the Algeria Renewable Energy Development Program foresees the introduction of biomass sector with a contribution of 1000 MW by 2030. This represents barely 5% of the country's renewable energy targets which amount to 22 000 MW, 93.5% of which are planned for solar and wind. In 2020, this objective has been reduced to 15,000 MW and the deadline extended to 2035. To date, despite the growing perception of a real desire to encourage clean energy projects, the renewable energy installed capacity is less than 500 MW without any contribution from the biomass sector. However, whatever the goals or the achievements, the need for renewable deployment is crucial for strategic purposes such as energy, water desalination and food security. The relationship between food security, sustainable development, and renewable energy is well demonstrated. Ensuring food security is closely linked with energy, hence with renewable energy sources in the middle and long terms, including biomass valorization. This paper presents a comprehensive outlook of the bioenergy sector, highlighting the barriers, which stand in the path of biomass recovery and use. Today, it appears clearly that a significant increase in renewable energy can only be achieved by higher solar power production.

***Keywords*− Biomass, Bioenergy, Energy mix, Energy and Food security.**

I. Introduction

.Globally, humanity consumes nearly 15 billion tons of oil equivalents. This represents approximately 1.8 tons per inhabitant. The current trend in energy consumption is indeed very worrying, with a rate of about 2% per year of growth [1], which means a doubling of this consumption every 35 years. Several elements clearly indicate that the current global energy system is not sustainable in the long term and that it must change. As energy sources are not evenly distributed worldwide, each nation has to optimize its own energy mix taking into account its potentials and possibilities. In the same time, climate change accelerating drastic effects on the planet is calling for an urgent need to transition towards renewables while geopolitics is thwarting trade and the way fossil energy is exchanged across regions. This makes the options even tougher for decision makers when it comes to energy planning. Sadly enough, because of a massive gas supplies disruption, instead of accelerating the pace towards cleaner energy sources, we are witnessing a comeback of coal in many parts of the world despite climate goals and environmental issues. It can be argued that the upheaval caused by the Ukrainian crisis in the international energy landscape has led to an unexpected lack of interest in the energy transition in many countries. The main reason oil and gas producers are obviously reluctant to turn their back on fossil fuels which provide external income, especially when the ongoing conflict which has led to the disruption of Russian gas supplies to Europe, has pushed prices up to pre-2014 levels. Almost everywhere in Europe, coal-fired power plants are back in service, to cope with the cut in the supply of Russian gas. It seems clear that the priority of the leaders of European countries dependent on Russian gas supplies does not seem to be in the energy transition, at least for the moment. In Germany for example, nearly a third of the electricity came from coal-fired power plants in the first half of 2022. In these countries, where the concept of energy transition was born and matured, the most urgent thing is to find new gas suppliers and manage to reduce the impact of rising energy prices on the way of life of their citizens. However, Algeria was counting on these countries to come and invest in the field of renewable energies to boost its energy transition. Oddly enough, the tender that was issued in March 2022 for the production of 100 MW solar electricity has not received much attention. It is also clear that, as one of the most fossil fuel-rich regions of the world, the Middle East and North Africa has not been at the forefront of the energy transition so far [2]. However, things are starting to move, with global zero-carbon targets pushing the region's countries towards developing their own carbon-neutrality targets and low-carbon fuel strategies. Egypt, for example, is aiming to provide the lowest-emissions natural gas and is emerging as an exporter of low-carbon LNG, electric power and green ammonia to Europe and beyond [2]. Other countries in the Gulf region have issued ambitious hydrogen strategies, and they are set to exploit abundant access to solar and wind power, natural gas reserves for blue hydrogen. Meanwhile, Algeria is aiming to make hydrogen a strategic vector of its energy transition program and its climate commitments. It is also keen to take advantage of its competitive advantages to supply the European hydrogen market with 10% of its needs by 2040 according to the media and officials declarations. Figure 1 shows the take-off of hydrogen production in the Middle East and North Africa from the 2030s. The production of hydrogen for energy purposes will be multiplied by ten in two decades, rising from less than 1 Mt in 2030 to nearly 10 Mt in 2050. Initially, it will consist almost entirely of blue hydrogen

Manuscript received May 28, 2024; revised July 5, 2024.

S. Haddoum and T. Ahmed Zaïd are with the Chemical engineering Department, Laboratoire de Valorisation des Energies Fossiles, Ecole Nationale Polytechnique, Algiers, ALGERIA. (emails: saliha.haddoum@g.enp.edu.dz, toudert.ahmed-zaid@g.enp.edu.dz)

H. Bennour is with the Mechanical Engineering Department, Ecole Nationale Polytechnique, Algiers, ALGERIA (email: hocine.bennour@g.enp.edu.dz)

Digital Object Identifier (DOI): 10.53907/enpesj.v4i1.195

produced by reforming natural gas with carbon capture and storage CCS. Blue hydrogen will remain dominant throughout the forecast period. Gradually however, green hydrogen produced in electrolysis plants using solar electricity and yellow hydrogen, produced by electrolysis from grid electricity, are expected to take off in the 2040s [2].

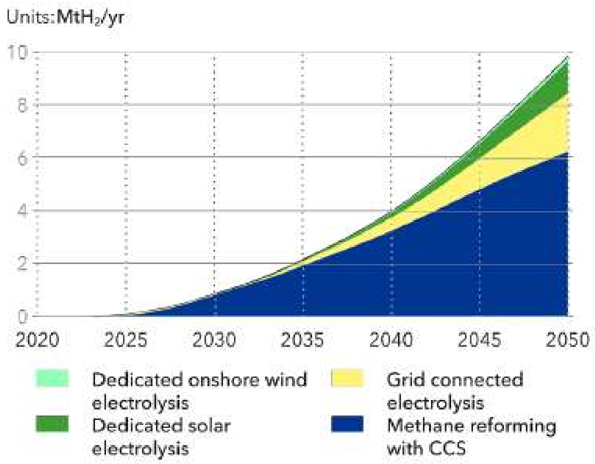

Fig.1: MENA Hydrogen production as energy carrier [2]

Indeed, the whole world is going through difficult economic times especially for those who have to import energy products. Algeria is an oil and gas exporting country and, in this respect, the recent increase in oil and gas prices should benefit its economy. It should namely accelerate its energy transition and help to win the double challenge of diverting its economy away from oil and gas while cushioning the social impact of the ongoing reforms and the ones to come.

II. ALGERIAN RENEWABLE ENERGY POTENTIAL

II. 1 SOLAR AND WIND ENERGY

Because of its geographical location, Algeria holds one of the highest solar potentials in the world, which is estimated at 13.9 TWh per year. The country receives annual sunshine exposure equivalent to 2,500 KWh/m2. Daily solar energy potential varies from 4.66 kWh/m2 in the north to 7.26 kWh/m2 in the south.

Algeria has also promising wind energy potential of about 35 TWh/year. Almost half of the country experience significant wind speed. The country's first wind farm is being built at Adrar with installed capacity of 10MW.

Despite this important renewable energy potential, renewable energy, production (in particular photovoltaic and wind power) still occupies a minor place in the production of primary energy [3]. With 23 solar and wind facilities all over the country, the total currently installed capacity barely amounts to 500 MW. Various barriers still stand in the path of renewable energy development. These barriers will be briefly mentioned in the last section.

II. 2 BIOENERGY POTENTIAL

Biomass resources include wood and wood wastes, agricultural crops and their waste byproducts, municipal solid wastes, animal wastes, and waste from food processing.
Worldwide, the majority of biomass energy is produced from wood and wood wastes, followed by municipal solid wastes, agricultural waste, and landfill gases. Biomass is the third largest renewable electricity-generating source. In this respect, it is worth questioning to what extent could bioenergy play a role in Algeria, knowing that the country is committed to reduce its greenhouse gas (GHG) emissions by 7% by 2020-2030. In addition to promoting sustainable agriculture, biomass growing, harvesting, storage and transportation, trading, and processing to end use for energy conversion purposes can enhance rural economic development, via the creation of additional jobs.
A recent study assessed the Algerian potential energy recovery from various wastes to ca.1700 GWh [4]. Based on this comprehensive study, the potential of biomass feedstocks in Algeria is summarized in Table 1.
As can be seen, urban wastes are the prominent fermentable resource. Considering all the investigated biomass feedstock resources, an electricity potential of ca. 1700 GWh can be reached from waste recovery that could meet the energy needs of over one million inhabitants [4]. This –theoretical - value represents less than 0.3% of the total energy consumption, so the biomass contribution to the energy mix seems quite negligible.

Table. I
BIOMASS FEEDSTOCK POTENTIAL FROM VARIOUS WASTES [4]

Biomass resources	Annual biogas potential	Power generation potential (GWh)
Urban wastes		
Organic fraction of household wastes	974 million of m^3	1646 (a)
Sewage from waste-water treatment plants	22.9 million of m^3	38.72 (a)
Industrial & agribusiness wastes		
Amurca from olive oil industry	10.5 million of m^3	17.74 (b)
Pomace from olive oil industry	---	215.50 (b)
Whey from dairy industry	2.35 million of m^3	3.97 (b)
Total	1009.76 million m^3	1706.43

Sources : (a) Ministère de l'Aménagement du Territoire et de l'Environnement (2013)
(b) FAO Statistics (2015).

One can argue that biomass potential is very limited in the Mediterranean region, which is characterized, by semi-arid climate conditions and where recurrent wildfires are continuing to threaten the already limited biomass resources. Nonetheless, the use of biomass for energy recovery is considered one of the priorities of the post-Kyoto development policies. Indeed, it represents an instrument to curb the climate changes and to reduce the environmental impacts that are linked to the use of fossil energy sources. This is why bioenergy development should target specific goals such as mitigating environmental issues.

III. BIOMASS FEEDSTOCKS RECOVERY

Throughout human history biomass in all its forms has been the most important source of all our basic needs (food, feed, fuel, feedstock, fiber and fertilizer). Forests have had a decisive influence on world civilizations, which flourished as long as forests and food producing areas backed up towns and cities. Today, biomass energy continues to be the main source of energy in many developing nations, particularly in its traditional forms, providing on average 35% of the energy needs of three-quarters of the world's population [5]. Despite the importance of bioenergy, there is surprisingly little reliable information on the consumption and supply of biomass. This serious lack of information is preventing policy makers and planners from formulating satisfactory sustainable energy policies. These multiple uses of biomass include not only energy but also food, fodder, building materials and more. Biomass is rarely, if ever, planted specifically for fuel: wood that is burned is often what is left over from some other process. Biomass energy should therefore always be looked at in the context of the other benefits that biomass provides, and never just from the point of view of a single sector. Having this in mind, we have listed the different problems and barriers that stand in the path of biomass energy valorization in Algeria.

III.1 Household wastes

The biodegradable organic fraction of wastes is recognized as a renewable energy source. The energy recovery of waste requires sorting operations upstream of the sector. A pilot project for the selective sorting of household waste at source was launched in Oran in 2015 as part of the framework of cooperation between Algeria and the World Organization R20. The role of the R20 "Regions of Climate Action" is to help governments implement low-carbon projects and to communicate best practices and policies in the area of renewable energy. This pilot project should therefore examine the possibilities of energy recovery from urban waste. Meanwhile less than 7% of household wastes are recycled for the recovery of metal and plastic according to the National Waste Agency (NWA). This is very low in view of the 4,000 businesses involved in the waste management sector. 13 million tons of household waste were generated in 2018, including 50% organic waste and 13% plastic. This figure is expected to exceed 20 million tons in 2035, according to a recent study carried out by the Ministry of the Environment. 34 million tons of waste of all categories are generated each year representing a potential market of nearly 90 billion Dinars [6]. To our knowledge, there is no data available on the energy recovery of household waste.

III.2 Farm and agricultural wastes

Sustainable farming is at the heart of all food security policies. Indeed, sustainable farm projects are flourishing all over the world. Achieving energy autonomy of farms is one of the conditions to achieve food security. Growers may use methods to promote soil health, minimize water use, and lower pollution levels on the farm and, more importantly, need reliable sources of energy. Hence, in order to secure the farm energy autonomy, biofuels need to be produced locally. It is also possible to convert all kinds of agricultural and animal wastes by methanation. A biogas unit can perfectly fit into the agricultural value chain and offer many environmental benefits. Indeed, digestate, a by-product of biogas, is a green manure that can be used advantageously in place of chemical fertilizers. Biogas can fuel a micro cogeneration unit, and the surplus of produced electricity can eventually be injected into the grid. However, major constraints and limitations prevent the deployment of methanation projects in Algeria where farm sizes are generally too small for cogeneration projects to be cost-effective. Of the 967,800 farms in all categories, 52.3 % have sizes under 5 hectares and only 1.9 % have sizes of at least 50 hectares [7]. Meanwhile, without government support mechanisms such as long-term investment guarantees and the introduction of Feed-in-Tariffs similar to those provided for solar and Wind, it is financially difficult to implement cogeneration or anaerobic digestion projects. Nevertheless, it is generally accepted that Algeria has the profile as well as the conditions to develop its agricultural sector including: land, fertilizers, ability to increase mechanized agriculture and to develop the industrial sector, natural resources to sustain mechanized agriculture, human resources and a need to generate employment.

III.3 Forest wastes

There is an increasing understanding that only bioenergy that is supplied and used in a sustainable manner has a place in a low carbon energy future [8]. The use of woody biomass for energy purposes is a controversial subject in Algeria which has only low forest resources. Algeria total forest area is relatively small 4 118 940 ha which represents around 16.47 % of the north region area [9]. As desertification is likely to intensify with climate change, Algeria is engaged in a vast reforestation project to counteract the creeping phenomena. According to the Forest General Direction, around 80,000 hectares have been planted since 2000 in the highland regions and in the southern and northern regions of the country. The National Reforestation Plan (NRP) was planned to cover 1.2 million hectares by 2020. At present, the forest heritage in Algeria represents 11% of the total land area . The NRP aims to increase this rate to 13% by 2029 [10]. Three million hectares of land suitable for forestry or subject to erosion or desertification are to be planted in order to achieve a rate of afforestation of 24% in the next twenty years. The NRP is an important project aimed at addressing desertification. But fire forests which destroy thousands of ha each year are seriously undermining this plan. Increased efforts are needed to combat forest fires and support forest law enforcement. The damages caused by the fires in summer 2017, 2021 and 2022 were on an exceptional scale, and occurred within a general context of escalation of this type of disaster.

Afforestation and reforestation projects can produce biomass that, once harvested, can be used for generation of heat and electricity. Associated with the NRP, the cultivation of short rotation crops on degraded land, would sequester carbon, regenerate degraded soils, empower local communities to develop sustainable agro-forestry practices and provide an alternate livelihood potential. However, all these objectives need to be supported and framed by sound policies including all stakeholders. Obviously, our forests are poorly managed and we all know that a forest, which is treated as a sanctuary, is a poorly maintained forest, in which trees struggle to grow and are more vulnerable to stresses such as fires. It is only to be hoped that the objectives of reforestation will be met in order to increase the plant cover, and to slow down the advancing desert in the perspective of an acceleration of global warming. Today, not all the indicators encourage energy recovery from woody biomass and even the sustainable management of our forests seems beyond our reach.

IV. The challenge of Food security

The links between energy and agriculture have been accentuated since the advent of oil. During the oil era, traditional agriculture has gradually become mechanized and is now very dependent on fossil fuels. With depletion of these nonrenewable resources, and escalating climate changes, food security is threatened on a global scale. According to the United Nations (UN) report, more than 836 million people in the world live in extreme poverty. Sustainable agriculture can offer a solution to increase production efficiency and meet the demand of the world's population [11]. According to FAO, agriculture and food supply chain are extremely dependent on fossil energy and contribute to 24% of the total global greenhouse gas (GHG) emissions. Figure 2 [12] shows the share of agriculture in global GHG emissions. These account for nearly one-third of annual GHG emissions [13]. Hence, sustainable agriculture practices and a shift to renewables can address both the climate change and the depleting fossil energy sources. Indeed, Global increases in population, increasing impacts of climate change, and threats to food, water and energy security have placed a renewed focus on the implementation of sustainability concepts. Solar energy is already widely used in agriculture as a substitute for conventional fossil fuels [14]. Agrivoltaic systems, in the form of photovoltaic (PV) modules installed on agricultural land, which optimally distribute sunlight to crops, maximize food and energy yields within reasonable limits have been already tested successfully in Japan [15].

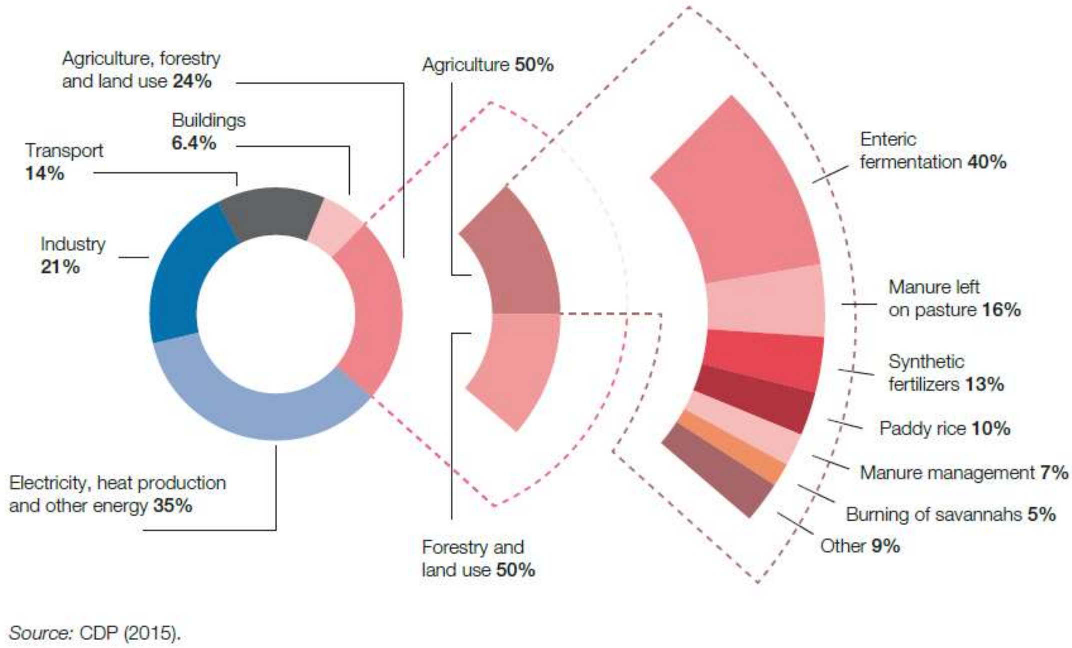

Fig.2: The share of agriculture in global GHG emissions [14]

Amjith and Bavanish [16] studied the potential of wind energy systems and biomass-based hybrid configurations with wind and their various design factors. They found that biomass-based hybrid energy systems could be a cost-effective and environmentally friendly alternative for off-grid rural and agricultural electrification. However, it is good to remember that the complexity of bioenergy value chains requires considerable information requirements on policy makers, when attempting to steer bioenergy use to achieve targeted goals [17]. Careful evaluation of policies is necessary before implementation. In Algeria, both arable land and water resources are limited rendering more challenging the food security objectives. Water stress is expected to be further exacerbated by climate change. Thus, more coordinated planning and action will be needed between the water and energy sectors to prevent a further worsening of the water deficit. Integrated thinking on energy and water is thus essential to mitigate future stresses [18]. There is no doubt that, from a food security prospect, solar energy will play a key role in water pumping, seawater desalination and wastewater, all of which require high-energy consumption. Indeed, the authorities are already relying on the desalination of seawater to alleviate this stress and many desalination plants are planned or under construction along the Algerian coastline. The main aim of these desalination plants is to safeguard drinking water supplies to various regions, which are severely hit by drought. However, as long as fossil energy continues to be used for this purpose, the sustainability of the process is at risk, and greenhouse gas emissions are obviously significant because desalination is energy-intensive. Water recycling should be seriously considered only for irrigation purposes. Agriculture is tightly linked with food security, and in this prospect, solar energy will play a key role for ensuring sustainability. Poor irrigation practices and mismanagement of inputs are also a concern in the agriculture sector. Indeed, the adoption of sustainable farming practices is also essential to meeting the challenge of food security. Today more than ever, energy security is at the heart of all issues. Algeria has set up an important legal arsenal and various attractive mechanisms for the promotion of renewable energies and energy efficiency at all levels. A detailed battery of legislative texts can be found in the GIZ report issued in July 2022 [19]. The fact remains that many legal texts have not been applied in the field. According to the results of a survey, cited in another report issued in 2020 [20], one of the main barriers in the energy market is the monopolistic regime, in which natural gas - as primary energy - has a price well below the international price and an uncompetitive cost of renewable energy. Other barriers were briefly discussed in a previous paper [18]

V. Conclusion

Global increases in population, increasing impacts of climate change, and threats to food, water and energy security have placed a renewed focus on the implementation of sustainability concepts. The use of biomass for energy recovery is considered one of the priorities of the post-Kyoto development policies. Indeed, it represents an instrument to curb the climate changes and to reduce the environmental impacts that are linked to the use of fossil energy sources. One can argue that biomass potential is very limited in the Mediterranean region, which is characterized, by semi-arid climate conditions and where recurrent wildfires are continuing to threaten the already limited biomass resources. The lack of relevant data concerning biomass potential itself, the reliance on fossil energy sources, and a poor market acceptance due to the heavily subsidized fossil energy products are also among the most significant barriers to bioenergy deployment. With the increasing demand for food and the advent of mechanization in agriculture, energy must be supplied at a higher level. With the depletion of fossil resources, the agricultural sector, with its wide variety of energy applications and resources, is expected to be one of the main users of renewable energy systems. The current situation of rising oil and gas prices offers real opportunities of ensuring an energy transition thanks to the development of photovoltaic solar energy. It is also time to seize this opportunity to initiate and/or accelerate the necessary reforms and ensure food security and a sustainable energy future. According to the APS, the state aims to achieve self-sufficiency, reduce imports, particularly of cereals and pulses, and expand the agricultural area from 8,000 hectares to 2.4 million hectares, particularly on highlands and in the southern regions. The new areas must be efficiently irrigated using renewable energies with the aim of achieving yields of around 70 quintals per hectare. According to the same source, SONELGAZ has already adopted a special farm linkage plan with a budget of more than 25 billion Algerian dinars aimed at accelerating agricultural development and increasing the country's agricultural production. Given the importance of this process, out of 45,878 farms, the number of connected farms reached 20,233, with an achievement rate of 44%. Thus the use of renewable energy, which was marginal until now, is expected to gradually increase as long as the agricultural sector is supported in its transition to solar and wind power by providing sources of financing supported by the State in the form of granting loans dedicated to this matter at a low interest rate and long repayment term. In the period 2020-2021, we saw the importance of government leadership in responding to the coronavirus crisis. Now this leadership is also needed to achieve both energy and economy transitions in our country.

References

[1] Bernard Lachal, Energy Transition, John Wiley & Sons; 2019

[2] DNV Energy Transition Outlook Middle East and North main report; 2022 available online at https://www.dnv.com/energy-transition-outlook/download.html#downloadform Accessed on 3 April 2023.

[3] Ministère de l'Energie et des Mines, Bilan énergétique National 2021, available on line at https://www.energy.gov.dz/Media/galerie/bilan_energetique_2021_63df78f2b775e.pdf. accessed 28 March 2023

[4] Akbi Amine, Meryem Saber, Majda Aziza, Noureddine Yassaa, Renewable and Sustainable Energy Reviews 72; 2017 pp 240–245.

[5] Frank Rosillo-Calle, Peter de Groot, Sarah L. Hemstock, Jeremy Woods - The Biomass Assessment Handbook_ Bioenergy for a Sustainable Environment-Earthscan Publications Ltd. (2008).

[6] Algérie Presse Service, La quantité des déchets ménagers en Algérie dépassera 20 Millions de Tonnes en 2035 available online at https://www.aps.dz/societe/118150-la-quantite-des-dechets-menagers-en-algerie-depassera-20-millions-de-tonnes-en-2035 accessed 3 April 2023

[7] RCM (Réseau Innovation Agro-systèmes Méditerranéen) available online at http://www.rcmed.org/index.php?id=139&tx_powermailfrontend_pi1[show]=8 Accessed June 22, 2020

[8] IEA, Technology Roadmap Delivering Sustainable Bioenergy; 2017, https://webstore.iea.org/technology-roadmap-delivering-sustainable-bioenergy Accessed March 12, 2020

[9] FOSA, Etude prospective du secteur forestier en Afrique, FOSA, Algérie, Rome, 2000, available online : http://www.fao.org/3/a-x6771f.pdf Accessed on November 8, 2019

[10] Plan National de Reboisement at http://dgf.org.dz/sites/default/files/synthese_plan_national_de_reboisement.pdf

[11] Ala A, Ridwan I. Food security and sustainable agriculture. IOP Conf Ser Earth Environ Sci. 2020 ; 486: 012110.

[12] Richards M, Arslan A, Cavatassi R, Rosenstock T. Climate change mitigation potential of IFAD investments. IFAD Research Series 35 [Internet]. IFAD, Rome. 2019. p. 34. Available from: https://www.ifad.org/documents/38714170/41066943/35_research.pdf/73e25d17-2d7b-b268-1edc-69c87d8d5668?t=1551957298000

[13] Gorjian S, Bousi E, Özdemir ÖE, Trommsdorff M, Kumar NM, Anand A, Kant K, Chopra SS. Progress and challenges of crop production and electricity generation in agrivoltaic systems using semi-transparent photovoltaic technology. Renew Sustain Energy Rev. 2022;158:112126

[14] Bordoloi S. Simulation And Analysis Of Green House Based Agri-Voltaic System Using Energy 3d Software. J Eng Technol. 2021;10:6–11.

[15] Riaz MH, Imran H, Alam H, Alam MA, Butt NZ. Crop-Specific Optimization of Bifacial PV Arrays for Agrivoltaic Food-Energy Production: The Light-Productivity-Factor Approach. IEEE J Photovoltaics. 2022;12:572–80.

[16] Amjith L, Bavanish B. A review on biomass and wind as renewable energy for sustainable environment. Chemosphere. 2022;293:133579.

[17] Purkus Alexandra, Concepts and Instruments for a Rational Bioenergy Policy: A New Institutional Economics Approach; Springer; 2016

[18] S. Haddoum, H. Bennour, T. Ahmed Zaid, Algerian Energy policy, perspectives, barriers and missed opportunities, Global Challenges; 2018, 1700134. https://doi.org/10.1002/gch2.201700134

[19] GIZ, Développement du cadre réglementaire et incitatif de l'efficacité énergétique en Algérie, July 2022, available online at : https://www.energypartnership-algeria.org/fileadmin/user_upload/algeria/Partenariat_Energetique_rapport_cadre_r%C3%A9glementaire.pdf accessed on April 2, 2023.

[20] MeetMED, Country Report on Energy Efficiency and Renewable Energy Investment Climate, 2020 available on line at : https://meetmed.org/wp-content/uploads/2022/03/Algeria_Country_Report.pdf accessed on April 2, 2023

Saliha Haddoum is a Lecturer at the Chemical Engineering Department at Ecole Nationale Polytechnique, Algiers. She has been involved in teaching and research at the Department of Chemical Engineering since 1980. She has particular expertise in physical chemistry and catalysis. She has made several presentations at national and international conferences, and has published many scientific papers in the field of materials and environmental sciences. She has also supervised many engineer and Master Students.

Hocine Bennour, born on November 20, 1958 in Chabet-El-Ameur (Boumerdes), is an assistant professor at the Mechanical Engineering Department Ecole Nationale Polytechnique, Algiers. He has been involved in teaching and research in thermodynamic cycles, Energy conversion and Turbo-machinery.

Toudert Ahmed Zaid, born on August 15, 1954 in Ain El Hammam (Tizi-Ouzou), is Professor at the Chemical Engineering Department Ecole Nationale Polytechnique, Algiers. He has an experience of 20 years in the field of surfactants and dispersed systems. He has authored or co-authored of more than thirty papers mainly in this research area.

Anaerobic digestion of municipal solid waste produced by the city of Algiers using life cycle assessment

Sadia Zibouche, Rabah Bouarab, and Mohammed Amouri

Abstract− This study analyses the life cycle assessment of anaerobic digestion process of municipal solid waste management (MSWM) produced by Algiers city. Some keys parameters of the processes are then modified to analyze the "hot spots" and perform a sensitivity analysis to identify their influence on the results. Data for the inventory came from actual city facilities, and background process information came from Eco invent version 3.1 of *SimaPro 8.1* software. The analyzed process contribution indicates that the global warming potential is affected by the anaerobic digestion because of the NO_x and CO emissions from the thermal processes of biogas burning and fuel oil combustion for digesters heating. Furthermore, plastics recycling is environmentally beneficial because of net savings. The energy valorization of biogas produces the least amount of environmental damage, eliminating 403.06 kg CO_2 eq/ton of waste, saving 18.2 E+09 MJ/ton of fossil fuels, and producing 2.8 E+08 kWhel/year, or 6% of the city's annual electricity consumption.

***Keywords*− Anaerobic digestion, municipal solid waste, life cycle assessment, energy recovery, recycling.**

NOMENCLATURE

AD	Anaerobic digestion.
LCA	Life cycle assessment.
MSWM	Municipal solid waste management.
OFMSW	Organic fraction of municipal solid waste.
CHP	Combined heat power.
OD	Ozone layer depletion.
GHG	Greenhouse gas.
TA	Terrestrial acidification.
HT	Human toxicity.
GWP	Global warming potential.
FD	Fossil depletion.

I. INTRODUCTION

The daily per capita production of MSW in the city of Algiers doubled between 1980 and 2018, rising from an average of 0.63 to 1.25 kg per day per inhabitant. Similarly, the quantity of MSW produced by the city of Algiers increased dramatically, reaching 1,237,874 tons in 2018. In exchange, the waste management and treatment policy has not changed. The same mode of management inherited from the colonial period (landfill) is maintained. This choice is inappropriate for Algerian garbage since it mostly consists of organic waste (60 percent by weight), which produces a lot of CH4 and leachates, which are sources of pollution [1]. Additionally, there is opposition to the planning of new landfill sites, and dump capacities are decreasing, particularly in metropolitan areas [2]. Anaerobic Digestion (AD) or composting systems are the best ways to treat waste with high organic fractions [1]. Besides, anaerobic digestion is a well-proven technology to process municipal solid waste rich in organic fraction (OFMSW) [3]. The study conducted by Zibouche et al. confirms that anaerobic digestion seems to be more sustainable treatment alternative in terms of total CO_2 and total SO_2 saved for Algerian waste [4]. The same results are confirmed by multiple studies in different regions of the world. According to Edward et al., compared to existing waste management methods, anaerobic digestion has less of an influence on acidification, minimal capacity to deplete fossil fuels, and a reduced potential to cause global warming [5]. In addition to its positive effects on the environment, reports suggest that the AD process is commercially viable and has the potential to generate significant revenue. In this context, several authors have focused on in-depth studies of anaerobic digestion systems. Moreover, other research teams continue to work on anaerobic digestion to overcome obstacles and promote commercialization. Researchers need to examine anaerobic digestion at a systems level, taking into account its technological, economic, and environmental benefits [6]. Avangelisti et al. have conducted a sensitivity analysis on anaerobic digestion parameters to confirm the robustness of the results. In this regard, four parameters have been investigated: the sequestration of digestate carbon, emissions from digestate consumption, efficiency of the CHP unit, and fugitive methane emissions from the AD plant [3]. The findings verify that the most important presumption relates to the amount and quality of energy generated by the biogas. The optimization of the electricity produced by the biogas-fed cogeneration unit and the establishment of the future energy scenario in which the plant will be integrated are two crucial factors that influence the design and implementation of future anaerobic digestion plants. On that respect, Hadzik et al. investigate the influence of waste composition on the anaerobic digestion process. The findings indicate that waste composition affects recycling, thermal treatment of residual waste, and biogas production potentials and nutrient enrichment.

Manuscript received February 15, 2024; revised June 28, 2024.

S. ZIBOUCHE, R. BOUARAB are with Laboratoire de Valorisation des Energies Fossiles, Chemical Engineering Department, Ecole Nationale Polytechnique, Algiers, Algeria. (sadia.zibouche@g.enp.edu.dz, rabah.bouarab@g.enp.edu.dz).

M. AMOURI is with Centre de Développement des Energies Renouvelables CDER, Bouzareah, Algies, Algeria (m.amouri@cder.dz)

Digital Object Identifier (DOI): 10.53907/enpesj.v4i1.256

The objective of this paper is to assess the anaerobic digestion of *MSW* by using life cycle assessment. This identifies the contribution of each subsystem on the investigated environmental impacts. Some processes key parameters are then modified to analyze the "hot spots" and perform a sensitivity analysis to determine their impact on the outcomes. In this context, life cycle assessment has been conducted for anaerobic digestion process composed of seven subsystems including site capital goods, sorting plant, waste pre-treatment, anaerobic digestion, leachate treatment unit, biogas valorization unit and transportation of construction and operating materials to the treatment unit, with an analysis of the influence of the subsystems on each of the five impacts studied. The intermediate categories (Midpoint) considered are; global warming potential (GWP), terrestrial acidification (TA), ozone layer depletion (OD), fossil depletion (FD) and human toxicity (HT).

II. MATERIAL AND METHOD

Case study

The nation's capital, Algiers City, will serve as the case study, because it is the city with the highest *MSW* generation. Indeed, it includes the most important concentrations of population, industries and large urban projects, the political and social institutions, the great economic and financial establishments.

The amount of *MSW* produced by Algiers city has increased dramatically between 1960 and 2018 to reach 1 237 874 tons of waste.

The management of wastes in Algiers district has long been limited to collection and transporting to dump sites. The two landfill units—HAMICI in the west, located at 36°39'29.99 "N, 2°49'14.33 "E, and CORSO unit in the east, located at 36°43'24.1 "N, 3°27'08.0 "E—are where the garbage is dumped.

Physical composition and chemical analysis

- The moisture (% M) is considered to 60% of the total volume of MSW.
- Of the waste that was taken into account for this study is made up of 15% other materials, 5% papers, 3% metals, 1% glassware, and 57% organic waste.
- With a 68% volatile matter content, 136 m3 of biogas are predicted to be produced for every ton of waste.
- The biogas produced is composed of 75% of CH_4, 21% of CO_2 and trace gases such as H_2S (59 ppm).
- The result of the study conducted by Nimaa et al. confirm that composts produced the urban solid residues in Algeria exhibit characteristics of organic amendments [7].

Anaerobic digestion unit

With reference to the fig. 1 schematic, below is a basic synopsis of the unit procedures. Pre-treatment, *AD*, biogas recovery unit, the digestate treatment unit, and the leachate treatment unit are the five primary subsystems that make up the *AD* unit under consideration.

Pre-treatment of MSW

Sorting procedures that can separate the waste into its organic and inorganic components are part of the pre-treatment. The organic fraction (about 50% of the original *MSW* weight) consists mainly of kitchen waste while plastics, wood, paper and cardboard, textiles that are not considered fermentable. This fraction represents 23% of the total composition. It is delivered to specific recycling facilities, which are usually located 30 km from *MSW* treatment plants.

Many studies have investigated the effect of recycling on different environmental impacts. When metals and plastics are sorted at material recovery plants before being converted to energy, the worldwide environmental impact is greatly increased [8].

Due to the high moisture content of the waste, in this case study, the paper and textiles are contaminated by wastewater from food waste and cannot be recovered or recycled [9].

The waste fraction retained for anaerobic digestion would be reduced in size to improve biodegradability. In this context, the data on the energy required for the grinding operations are taken from the study conducted by Fernandez-Nava et al [10]. The electricity consumption of the mixed waste sorting plant as well as the shredding operations is estimated at 58 kWh per ton of waste.

***AD* plant**

Reactors for anaerobic digestion provide significantly improved control over the process, faster production of methane and biodegradation, and nearly total methane capture. Since AD is a renewable energy source, it may increase energy supply security and contribute to a decrease in greenhouse gas (GHG) emissions. In contrast to certain other renewable energy sources like wind and solar, which are more intermittent, it is also helpful as a source of energy that can be used whenever needed [11]. There are two primary digesters and one secondary digester installed in the anaerobic digestion unit under consideration.

The digesters used in this investigation are situated at BERRAKI's wastewater treatment plant in the city's center at 36°41'42.9 "N 3°06'25.1 "E. The retained fraction undergoes grinding, shredding and screening operations to reduce its size and reach a dry matter concentration of 50%, thus approaching the anaerobic digestion conditions used in the unit in question. After 25 days of residence at 37 °C and pH of 7.1, the anaerobic digestion reaction occurs, eliminating 50% of the organic matter by weight. The large range of applications and the high water content of the waste led to the selection of this wet digestion method. The primary digesters are continuously fed waste with a 50% dry matter concentration. Each digester has a 12,000 m^3 capacity. The waste has to be heated to compensate for heat losses and the arrival of fresh waste. It enters the exchanger on the opposite side to the hot water (counter-current heat exchanger). The hot water enters the exchanger at a temperature between 50 and 70°C. While the waste enters to the exchanger at 37°C and exits at 40°C.

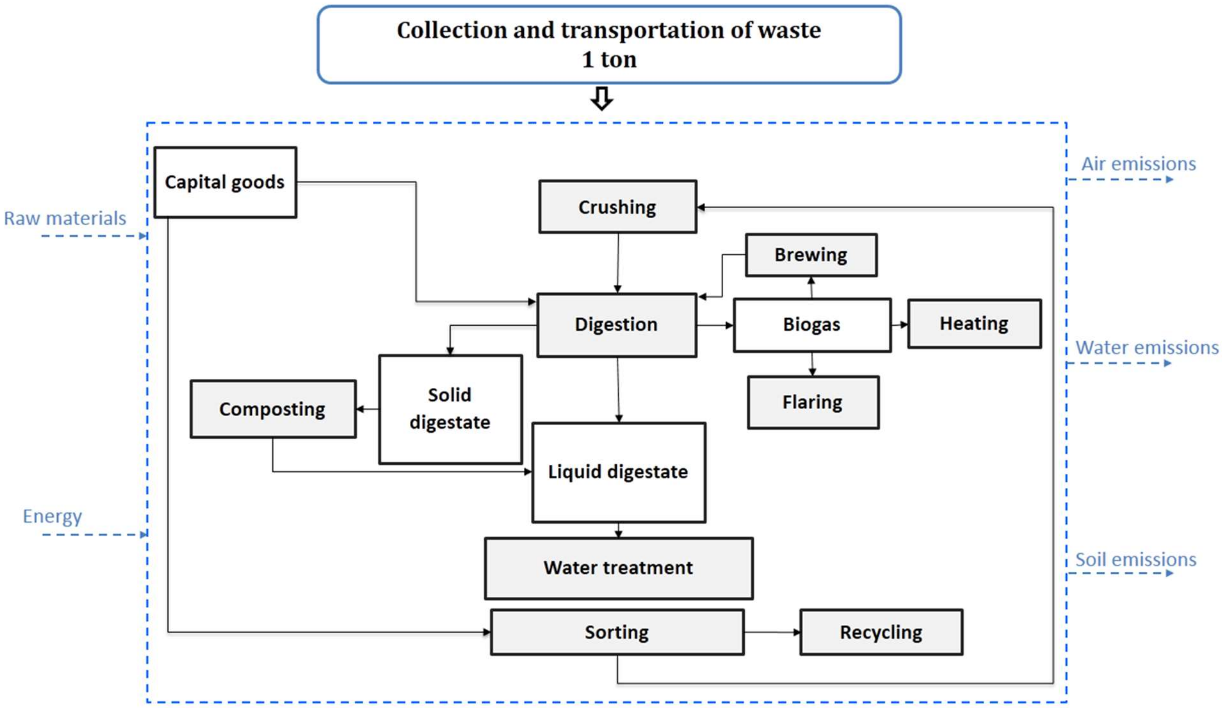

Fig. 1: Description of the unit processes of anaerobic digestion.

Use of biogas

The anaerobic digestion reaction produces 136 m^3 of biogas per ton of waste with composition of 75% of methane, corresponding to a net calorific value of 26 MJ/Nm^3. The biogas escapes upwards from the digesters and is stored in top of the digesters.

The compressor receives a portion of the biogas that is taken out of the digester's top. Once compressed, It is suppressed by the compressors and travels as bubbles at the bottom of the digesters to the sludge mixing rods. The biogas bubbles rise to the surface of the sludge, causing the sludge to move upwards. A water-cooling unit is associated with the compressors to prevent damage.

In addition, the biogas produced by anaerobic digestion is used to produce hot water for the process, using two boilers. When the gasometer level hits the high filling threshold of 35%, biogas is fed into the boiler burner. The burner uses fuel oil (diesel) if this level is below the 20% low threshold.

The gasometer is of flexible type with a double membrane, which has a storage capacity of 3000 m^3. These two membranes are made of a polyester complex and a PVC coating. The inner membrane is biogas-tight and has a high chemical resistance to biogas. The outer membrane has high mechanical strength and resistance to the outdoor climate. It is also biogas-tight enough to store biogas temporarily (for example, if the inner membrane breaks).

To prevent excessive biogas from leaking into the atmosphere, it is burned using a flare. When the gasometer's level is more than 80% of the overall level, it fires. The requirements for pre-treatment, the digesters' biogas mixing system, and digestate drying account for 3.24E-02 kWh of electricity usage.

Anaerobic digestion produces biogas, which is a sustainable and clean energy source that can be used to replace conventional energy sources that are producing ecological and environmental concerns while also depleting at a faster rate [12]. In most circumstances, without additional purification, it can be added to power gas engines (ideally in a combined heat and power (CHP) plant).

Furthermore, 4.42E+02 kWh of heat are produced, which meets the heat requirement needed to maintain the digester's temperature at 35 °C. The unit uses 3.73E+02 kWh of power generated, with the remaining energy being fed back into the public grid. The cogeneration unit's emissions from burning biogas are based on [13].

Use of digestate

In our study, a stage of digestate dewatering is considered. The compost is used as an organic fertilizer. The compost produced in Algeria has rates of N, P, K, C, organic matter, and a C/N ratio that satisfies the NFU 44 051 standard, according to a study by Nimaa et al. The elements metallic tracks have less content than the allowable limits. Furthermore, the outcomes of the phytotoxicity tests verify that the composts generated have the properties of organic amendments [13].

Leachate treatment unit

The quantity and characteristic of the MSWs and their leachates differ from one place to another [14]. The types of garbage in the landfill, as well as its residual moisture content, water infiltration, stage of degradation, and landfilling technology, are the primary factors influencing these variations in leachate composition.

The landfill site studied generates 200 m^3/day of leachate, of which:

- 80 m^3/day: treated at a membrane leachate of treatment plant.
- 120 m^3/day: treated at a reverse osmosis leachate of treatment plant.

Afterwards, the leachate's quality is presumed to meet the ISO standard standards for landfill pollution, after which it will be directly released into the city's sewer system. Table 1 lists the features of the leachate following treatment at the landfill under investigation [4].

Table. 1
Characteristics of the leachate after treatment

Parameters	Unit	Reverse osmosis	Membrane leachate treatment	Limit values	Standard of analysis
Temperature	°C	13	19.3	30	/
pH		6.99	6.44	6.5-8.5	/
MES	mg/l	9	10	35	ISO 11923:1197
Kjeldahl Nitrogen	mg/l	12	17	30	ISO 5663:1984
Total phosphorus	mg/l	0.39	4.9	10	ISO 6878:2004
Phenol index	mg/l	0.1	0.1	0.5	ISO 6439:1990
DBO5	mg/l	58	14	35	ISO 5815:1989 (F)
DCO	mg/l	110	380	120	ISO 6060:1989
Oils and fats	mg/l	2	2	20	Rodier method
total hydrocarbons	mg/l	5	5	15	AST MD 1664
Aluminium	mg/l	1	1	3	ISO 120120:1997
Cadmium	mg/l	0.03	0.03	0.5	ISO
Lead	mg/l	0.2	0.2	0.5	8288:1986
Copper	mg/l	0.1	0.1	0.1	
Nickel	mg/l	0.2	0.2	0.1	
Zinc	mg/l	0.03	0.03	2	
Manganese	mg/l	0.03	0.03	1	
Iron	mg/l	0.2	0.2	3	FD T90-112

1.1. Life cycle assessment

The life cycle assessment (LCA) methodology is used to evaluate various approaches to waste treatment. The four components of an LCA are as follows: (1) Goal and scope definition; (2) Life Cycle Inventory assumptions (LCI); (3) Life cycle impact assessment (LCIA); and (4) Interpretation, as outlined in ISO 14040: 2006 - Environmental management - Principles and methodology for LCA (ISO, 2006). The ensuing sections will provide an explanation and detailed guide to these steps.

1.1.1. Goal and scope definition

The objective is to evaluate and compare the environmental impacts of anaerobic digestion unit as management systems of solid waste of Algiers city and determine the critical parameters including the greatest influence on the environment impact and leads to the selection of the best system.

Recently the system of management of municipal waste in Algeria has been considered as a priority of the Ministry in charge of the environment. The findings of this study will raise decision-makers' knowledge, which may help to lessen future negative environmental effects.

Although the evaluation is intended to be conducted on the waste stream of the biggest city in Algeria, the final findings can be generalized to be reliable for the majority of cities across the country due to their comparable compositions of solid waste (MSW) [15].

1.1.2. Functional Unit

It is essential to establish the functional unit in order to compare the scenarios on an individual basis. One ton of waste was chosen as the functional unit for this study.

1.1.3. System boundary

To enable others to reproduce the work, each assumption will be stated as precisely as possible.

-The operations of construction, biogas emissions, leachate treatment and post closure are taken into account.

-The collection of waste and their transport to the treatment unit are not taken into account.

-The transportation of construction and operating materials to the treatment unit is taken into consideration.

- In this analysis, fugitive greenhouse gas emissions from the AD process are taken to be zero.

-The transportation of materials (steel, HDPE concrete, diesel, etc.) to the treatment units is considered. Calculations reveal a quantity of 1.09 tkm for the anaerobic digestion unit.

1.1.4. Data acquisition and assumptions

Based on real data, an inventory has been created. The life cycle inventory data was obtained from actual anaerobic digestion systems of BARRAKI sludge (36°41'43.85 "N, 3° 6'25.49 "E), while the background data came from scientific literature and the Eco-invent V3 database. Table 02 displays the system's primary input and output streams, normalized per ton of waste. This study takes into account data from several procedures, both direct and indirect.

1.1.5. Allocation method

In this paper, a system expansion of substitution strategy is applied to use power produced as a byproduct. The emissions created during waste treatment are removed from those produced by the "avoided" emissions produced by traditional energy generation. Credits are therefore given for substituting the same amount of power produced by burning fossil fuels.

1.1.6. Life cycle impact assessment

Selecting the appropriate software is crucial for determining and evaluating how waste management systems affect the environment, and the data it holds must be updated and validated on a regular basis. Knowing the effects of your actions in the first and second stages of the Life Cycle Assessment (LCA) can help you make informed choices about the databases and LCA methodologies to utilize [18]. The LCA approach needs to satisfy the study's objectives and requirements, although the process for choosing the latter is frequently disregarded [19].

Table. 2
Principal streams of input and output of anaerobic digestion

Energy and material	Unit	Value
Input flow		
Electricity	kWh	145
Diesel	kg	0.600
Fuel	kg	5.700
Steel	kg	0.018
Concrete	kg	6.120
Sand	kg	19.600
Gravel	kg	29.400
Water	kg	3.060
Reinforcing steel	kg	23.300
Cast iron	kg	0.009
Carbon Steel	kg	0.001
Galvanized steel	kg	2.05E-02
Ductile iron	kg	7.43E-03
coated polyester	kg	6.21E-03
Stainless steel	kg	7.53E-03
Aluminium alloys	kg	2.19E-04
Gravel	kg	29.4
Oil lubrication	kg	1.24E-04
Membrane Clean Osmacid-AC	kg	7.28E-04
Membrane Clean NE 10	kg	4.85E-05
Caustic soda (33%)	kg	4.52E-02
Phosphoric acid (50%)	L	2.43E-05
Sulphuric acid (96--98%)	L	1.31E-04
Sodium hydroxide 33 %	kg	3.40E-02
kleen Osmal	L	1.36E-03
Citric acid monohydrate	kg	1.94E-04
Output flow		
Air emissions		
CO	Nm^3	5.26E+01
N_2	Nm^3	5.44E+00
CO_2	Nm^3	6.35E+02
H_2S	ppm	8.02E-03
Water emissions		
Suspended matter	Kg	5.00E-04
Kjeldahl nitrogen	Kg	6.38E-04
Total phosphorus	Kg	2.07E-05
Phenol index	Kg	5.32E-06
DBO5	Kg	5.80E-02
DCO	Kg	1.10E-01
Oil and grease	Kg	1.06E-04
Total hydrocarbons	Kg	2.66E-04
Aluminium	Kg	5.32E-05
Cadmium	Kg	1.59E-06
Lead	Kg	1.06E-05
Copper	Kg	5.32E-06
Nickel	Kg	1.06E-05
Zinc	Kg	1.59E-06
Iron	kg	1.06E-05
Manganese	kg	1.59E-06

The software SimaPro@ was used to perform the modeling. There is no recommended impact assessment approach for use in the ISO 14040/14044 standard. The ReCiPe assessment approach is applied in this investigation because it combines the straightforward interpretation of ECO-99 results with the scientific rigor of CML2001, making it more intriguing and warranted for application. In addition, the ReCiPe approach takes into account 18 intermediate categories—eight more than the ECO-99—that are combined into the three primary categories of resource depletion, ecosystem quality, and human health. These categories represent domains in which policy and decision-making decisions are frequently made.

According to Yi et al., the midpoint analysis increases the comprehensiveness of impacts by including more endpoint effects [20]. Additionally, the endpoint approach—, which uses straightforward indicators—has been useful in summarizing the integration of interpretations. However, It has not been very successful in illuminating the harms associated with various environmental impact categories at various spatial scales. As a result, endpoints could be categorized into global, regional, and local scales to aid in their interpretation.

Although coverage of more impact categories represents a more detailed analysis, this study will consider the most important impacts. In the impact evaluation, 96% of the evaluated research covered the category of GWP, which is associated with the issue of climate change, according to the Iqbal review. Human toxicity potential (HTP) and the acidification and eutrophication of water resources were also examined in more than half of the studies [21]. Global warming potential (GWP), ozone layer depletion (OD), terrestrial acidification (TA), human toxicity (HT), and fossil depletion (FD) are the five impact categories taken into consideration in this study.

1.1.7. Sensitivity analysis

Sensitive analysis was done to identify uncertainties in the goal of observing the robustness and reliability of the anaerobic digestion process under study, as small adjustments to inputs and assumptions could cause fluctuations in LCA results, which would unintentionally cause confusion in decision-making [22]. Four parameters—the value of the biogas produced, the transportation of wastes, the composition of wastes and biogas, and fugitive emissions from the anaerobic digestion facility—were taken into consideration due to their significant contributions to the anaerobic digestion process. The range of variation of the input parameter for the sensitivity analysis is shown in Table 3.

Energy recovery

The identical *AD* unit established above is used here, but it is assumed that the biogas generates both heat and electricity through a combined heat and power unit.

In addition to the benefits to the economy, environment, and climate, renewable energy rules have fostered an increase in biogas production in the European Union, which reached 18 billion m^3 of methane (654 PJ) in 2015, accounting for half of the world's biogas production [23].

The electrical conversion efficiency of 38% and the thermal conversion efficiency of 45%, which are within the reported range of biogas power and heat generation employing engine technology, are the primary characteristics utilized to model CHP plants [24].

Table. 3
Sensitivity analysis key parameters

Parameter	Value
Wastes Transportation	Average transportation of 1 t of waste in the city of Algiers was estimated to be 25 km.
MSW composition and biogas production.	Waste composition data from a landfill site showed a 60% organic fraction, a difference from the 40% organic fraction average for Africa. Based on local statistics, the organic content of waste, which is 136 m^3/ton of garbage, determines the potential for biogas production. When 40% of the waste is organic, the value has been changed to 90.7 m^3/ton waste.
Biogas composition (%CH_4 and % CO_2 and others trace gas)	A value of 75% CH_4 is taken into account, which is supported by experimental findings from Saber et al. For sensitivity analysis, an average CH_4 content of 60% is utilized.
Fugitive emissions from anaerobic digestion facility	This research takes into account methane losses from the digestion process that range from 0% to 9%. According to published research, the highest loss from fugitive losses in digestive systems is predicted to be 9%.

Without the need for additional purification, the biogas produced by AD is a clean, sustainable energy source that may be used straight in gas engines—ideally in a combined heat and power (CHP) plant.
Additionally, 4.42E+02 kWh of heat are generated, which is sufficient to meet the heat demand needed to maintain the digester's temperature at 35 °C. While the 3.73E + 02 meet the unit's internal needs kWh of electricity produced, the remaining energy will be fed back into the public grid. Based on Fruergaard and Astrup's assessment, the cogeneration unit's emissions from burning biogas [13].

Wastes Transportation

In the baseline scenario, waste collection and transfer to treatment units are not considered. According to the review conducted by Laurent et al. the most often tested parameters were those for collection and transportation [25]. The sensitive analysis studies the influence of transportation of the waste to an average transportation distance of 25 km per ton of waste.

MSW composition and biogas production

The sixth most tested criteria were the waste and biogas composition. It is strongly advised that practitioners incorporate waste composition in sensitivity studies since the variability of the treated materials frequently appears to be a substantial source of uncertainty [25]. In this case study, waste composition was provided from landfill facility to be 60 % of organic fraction and the variation was reported to the African average of 40 % of organic fraction. Biogas production potential is based on organic fraction, which is 136 m^3/ton waste according to local data. This value has been varied to be 90.7 m^3/ton waste in the case of 40% of organic fraction.
Regarding biogas composition, a value of 75 % of CH_4 is taken into consideration, which is confirmed by experimental results obtained by saber et al. A value of 60 % of CH_4 is used for sensitivity analysis as an average content of methane.

Fugitive emissions from anaerobic digestion facility

Recent research indicates that a number of sources, such as flares, feedstock storage, gas storage units, pipelines, safety valves utilized during digestion, and digestate storage, can leak methane during the anaerobic digestion process [26]. It is very difficult to estimate these emissions due to their variability from one site to another [3]. Significant amounts of fugitive methane emissions may originate from biogas plants. In general, fugitive losses at waste biogas facilities and whole-site farms are projected to have a maximum loss of 9%. This study takes into account methane losses throughout the digestive process that range from 0% to 9%.

III. RESULTS AND DISCUSSION

The Fig. 2 illustrates the contribution of each process studied in the anaerobic digestion process. The categories including human toxicity and terrestrial acidification are affected negatively by steel and iron used in the biogas facility because of the huge industrial installations built mostly in steel or cast iron (heating system, gasometer, unit of compression, boilers, etc.).

The methane bromotrifluoro-Halon 1301 is the main cause of the ODP [28]. Because of the rising need for fuel to heat reactors, ODP load is affected negatively (3.63E-05 kg CFC-11 eq by the emissions due to the fuel oil used to feed the boiler to produce hot water. this negative influence can be avoided by optimizing the anaerobic digestion process by feeding the two boilers with the biogas produced.
The global warming potential is widely affected by the anaerobic digestion because of the NOx and CO emissions from the thermal processes of biogas flaring and fuel oil combustion for digesters heating. The recycling of HDPE after the sorting operation displayed the greatest value of saving in three impact categories including global warming potential, fossil depletion and acidification potential. Recycling plastics saves the environment since it allows for net savings of -1600 kg CO2/ton of waste when virgin plastic is substituted [29].

Sensitivity analysis

The figure 3 illustrates how each parameter's fluctuation contributed to the impacts studied.
-Biogas valorization in CHP unit
Biogas power generation has positive effects and reduces the impact due to the replacement and conservation of non-renewable energy in all damage categories. The valorization of biogas in CHP unit as defined in the sensitivity study, allows to obtain less environmental impacts. Since it allows to eliminate 403.06 kg of CO_2 eq. per waste, to save fossil fuels with a net avoidance of 18.2 E+09 MJ per waste and to produce 2.8 E+08 kWhel/year of electricity, which covers 6% of the electricity needs of the city.

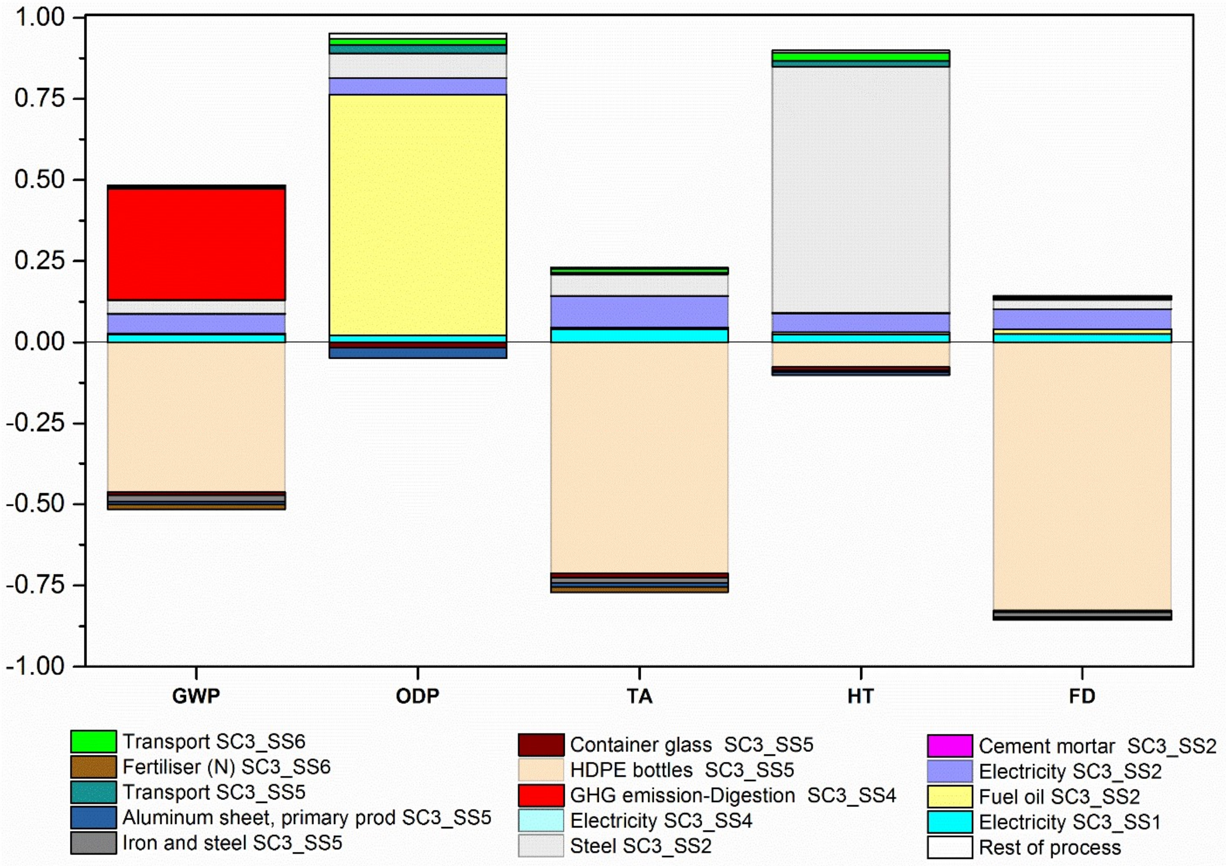

Fig .2: Contribution of each process in the anaerobic digestion process.

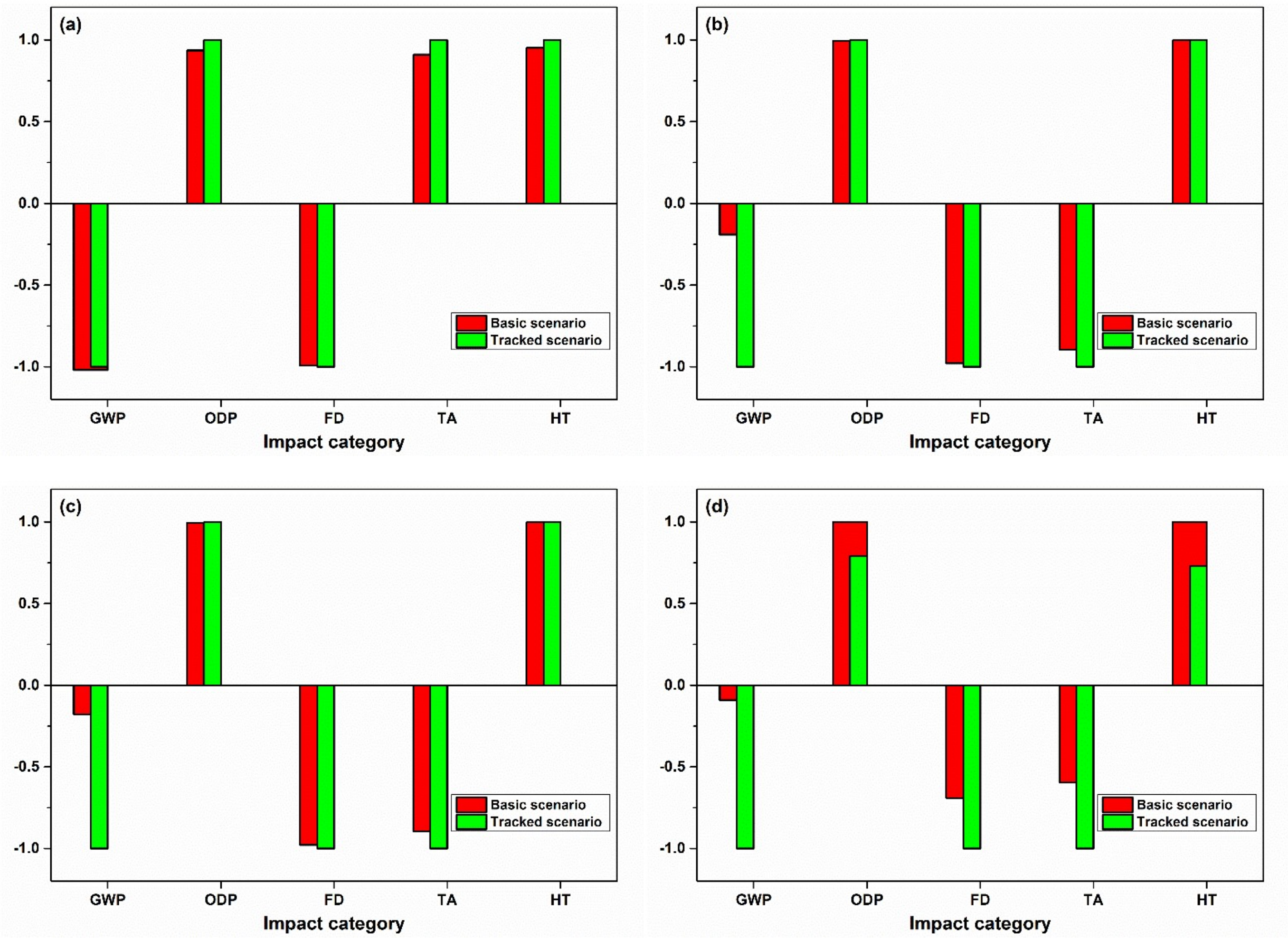

Fig. 3 Contribution of variation of each parameter in the studied impacts, (a) transport, (b) waste composition, (c) biogas composition and (d) energy valorization.

The emissions "avoided" by the conventional production of this energy are subtracted from the emissions generated by the waste treatment. As a result, credits are provided for substituting the equivalent quantity of power produced by burning fossil fuels. Fossil depletion refers to the use of fossil fuels, the results show that both anaerobic digestion scenarios do not contribute to the depletion of fossil fuels due to the valorization of the biogas produced. Significant environmental savings are obtained by energy recovery, according to Rana et al. [30], which explains the overall negative score obtained in the other two scenarios that show savings from fossil fuels. With a net avoidance of 453 kg oil equivalent per waste (18.2 E+09 MJ) from the valorized biogas scenario and 139 kg oil equivalent per waste (5.6 E+09 MJ) from cogeneration, the biggest savings are observed in this scenario.

Waste transportation

The most often evaluated parameters were those for collecting and transportation, though research typically concluded that their influence on the outcome was minimal [25]. Actually, there is raising concerns on environmental burden from waste collection and transportation indicating that more attention should be paid on this parameter [22].
The analyses show that the transport process does not imply a significant variation in the effects on the environment, with the exception of a slight increase in the terrestrial acidification and effects of ozone depletion due to greenhouse gas emissions.
Because of the efficient waste transportation to the treatment plant in the city of Algiers, it was discovered that the transportation process only contributes 2% of the total GWP for all scenarios examined.

Waste composition and biogas composition

The effects of changing the composition of the biogas yield results that are comparable to those of changing the waste composition. A decrease in the amount of organic matter in waste and a drop in the methane content of the biogas primarily suggest a decrease in the amount of energy generated in both cases. The anaerobic digestion system is significantly impacted by the greenhouse gas emissions released by biogas engines, as demonstrated by each process's contribution. For this reason, when compared to baseline assumptions, a decrease in the methane biogas content or the waste organic portion permits a reduction in the possible environmental effects of global warming.

Fugitive emissions

Based on this study, the GWP increases by more than 30 times when the methane losses of the digestion process are varied from 0% to 9%. This results in a contribution of 75.85 kg CO_2 eq/ton, instead of the avoided -36.70 kg CO_2 eq/ton of waste. This clearly shows the need of emission monitoring and management in biogas production, since fugitive losses have a major effect on the overall environmental performance of a biogas production system.

IV. CONCLUSION

This work aims to evaluate and analyses the environmental impacts of anaerobic digestion of MSW in the city of Algiers. The ozone depletion is primarily caused bmethane because there is a greater need for fuel to heat reactors. This detrimental effect can be prevented by maximizing the anaerobic digestion process to produce more biogas to the boiler. Because of the NOx and CO emissions from the thermal processes of biogas flaring and fuel oil burning for digester heating, anaerobic digestion has a significant impact on the global warming potential. However, HDPE recycling following sorting process demonstrated the highest value of savings in three impact areas, including the potential for global warming, acidification, and the depletion of fossil fuels. Sensitivity analysis reveals that biogas valorization stands out environmentally and helps to mitigate the effects of all the harm categories taken into consideration. It enables the production of 4.42E+02 kWh_{th}/ton of waste, meeting the necessary heat requirement. Utilizing the created biogas will enable the production of 2.8 E+08 kWh_{el}/year of electricity, which when injected to the public grid will satisfy the electricity requirements of 6% of the city's total population. In comparison to baseline assumptions, the results for the variance in the composition of waste and biogas indicate a decrease for energy produced. This allows lowering the potential environmental effects of global warming. The results of this study can be applied to other Algerian cities as well as cities around the world with comparable sociological and climatic circumstances. Evaluating and discussing the three pillars of sustainability requires integrating the findings with social (by social life cycle assessment) and economic (via life cycle costing) components.

REFERENCES

[1] Ramachandra TV, Bharath HA, Kulkarni G, Han SS (2018) Municipal solid waste: Generation, composition and GHG emissions in Bangalore, India. Renewable and Sustainable Energy Reviews 82:1122–1136. https://doi.org/10.1016/j.rser.2017.09.085

[2] Demetrious A, Crossin E (2019) Life cycle assessment of paper and plastic packaging waste in landfill, incineration, and gasification-pyrolysis. J Mater Cycles Waste Manag 21:850–860. https://doi.org/10.1007/s10163-019-00842-4

[3] Evangelisti S, Lettieri P, Borello D, Clift R (2014) Life cycle assessment of energy from waste via anaerobic digestion: A UK case study. Waste Management 34:226–237. https://doi.org/10.1016/j.wasman.2013.09.013

[4] Zibouche S, Amouri M, Bouarab R (2022) Life cycle assessment of different municipal solid waste management options: a case study of Algiers (Algeria). J Mater Cycles Waste Manag. https://doi.org/10.1007/s10163-022-01576-6

[5] Edwards J, Othman M, Crossin E, Burn S (2017) Anaerobic co-digestion of municipal food waste and sewage sludge: A comparative life cycle assessment in the context of a waste service provision. Bioresource Technology 223:237–249. https://doi.org/10.1016/j.biortech.2016.10.044

[6] Rajendran K, Murthy GS (2019) Techno-economic and life cycle assessments of anaerobic digestion – A review. Biocatalysis and Agricultural Biotechnology 20:101207. https://doi.org/10.1016/j.bcab.2019.101207

[7] Nimaa TD, Guyb M (2016) Sorting-Composting of Biodegradable Waste in the Municipality of Chief (Algeria): The Key Steps. Int J Waste Resour 6:. https://doi.org/10.4172/2252-5211.1000204

[8] Cremiato R, Mastellone ML, Tagliaferri C, et al (2018) Environmental impact of municipal solid waste management using Life Cycle Assessment: The effect of anaerobic digestion, materials recovery and secondary fuels production. Renewable Energy 124:180–188. https://doi.org/10.1016/j.renene.2017.06.033

[9] Zhuang Y, Wu S-W, Wang Y-L, et al (2008) Source separation of household waste: A case study in China. Waste Management 28:2022–2030. https://doi.org/10.1016/j.wasman.2007.08.012

[10] Fernández-Nava Y, del Río J, Rodríguez-Iglesias J, et al (2014) Life cycle assessment of different municipal solid waste management options: a case study of Asturias (Spain). Journal of Cleaner Production 81:178–189. https://doi.org/10.1016/j.jclepro.2014.06.008

[11] Whiting A, Azapagic A (2014) Life cycle environmental impacts of generating electricity and heat from biogas produced by anaerobic digestion. Energy 70:181–193. https://doi.org/10.1016/j.energy.2014.03.103

[12] Adekunle KF, Okolie JA (2015) A Review of Biochemical Process of Anaerobic Digestion. 8

[13] Fruergaard T, Astrup T (2011) Optimal utilization of waste-to-energy in an LCA perspective. Waste Management 31:572–582. https://doi.org/10.1016/j.wasman.2010.09.009
[14] Rong L, Zhang C, Jin D, Dai Z (2017) Assessment of the potential utilization of municipal solid waste from a closed irregular landfill. Journal of Cleaner Production 142:413–419. https://doi.org/10.1016/j.jclepro.2015.10.050
[15] Ripa M (2016) The relevance of site-specific data in Life Cycle Assessment (LCA). The case of the municipal solid waste management in the metropolitan city of Naples (Italy). 16
[16] Milutinović B, Stefanović G, Đekić PS, et al (2017) Environmental assessment of waste management scenarios with energy recovery using life cycle assessment and multi-criteria analysis. Energy 137:917–926. https://doi.org/10.1016/j.energy.2017.02.167
[17] Cherubini F, Bargigli S, Ulgiati S (2009) Life cycle assessment (LCA) of waste management strategies: Landfilling, sorting plant and incineration. Energy 34:2116–2123. https://doi.org/10.1016/j.energy.2008.08.023
[18] Kulczycka J, Lelek L, Lewandowska A, Zarebska J (2015) Life Cycle Assessment of Municipal Solid Waste Management – Comparison of Results Using Different LCA Models. Pol J Environ Stud 24:125–140. https://doi.org/10.15244/pjoes/26960
[19] Zhou Z, Tang Y, Chi Y, et al (2018) Waste-to-energy: A review of life cycle assessment and its extension methods. Waste Manag Res 36:3–16. https://doi.org/10.1177/0734242X17730137
[20] Yi S, Kurisu KH, Hanaki K (2011) Life cycle impact assessment and interpretation of municipal solid waste management scenarios based on the midpoint and endpoint approaches. Int J Life Cycle Assess 16:652–668. https://doi.org/10.1007/s11367-011-0297-3
[21] Iqbal A, Liu X, Chen G-H (2020) Municipal solid waste: Review of best practices in application of life cycle assessment and sustainable management techniques. Science of The Total Environment 729:138622. https://doi.org/10.1016/j.scitotenv.2020.138622
[22] Zhang J, Qin Q, Li G, Tseng C-H (2021) Sustainable municipal waste management strategies through life cycle assessment method: A review. Journal of Environmental Management 287:112238. https://doi.org/10.1016/j.jenvman.2021.112238
[23] Scarlat N (2018) Biogas: Developments and perspectives in Europe. Renewable Energy 16
[24] Kaparaju P, Rintala J (2013) Generation of heat and power from biogas for stationary applications: boilers, gas engines and turbines, combined heat and power (CHP) plants and fuel cells. In: The Biogas Handbook. Elsevier, pp 404–427
[25] Laurent A, Bakas I, Clavreul J, et al (2014) Review of LCA studies of solid waste management systems – Part I: Lessons learned and perspectives. Waste Management 34:573–588. https://doi.org/10.1016/j.wasman.2013.10.045
[26] Bakkaloglu S, Lowry D, Fisher RE, et al (2021) Quantification of methane emissions from UK biogas plants. Waste Management 124:82–93. https://doi.org/10.1016/j.wasman.2021.01.011
[27] Xu F, Li Y, Ge X, et al (2018) Anaerobic digestion of food waste – Challenges and opportunities. Bioresource Technology 247:1047–1058. https://doi.org/10.1016/j.biortech.2017.09.020
[28] Erses Yay AS (2015) Application of life cycle assessment (LCA) for municipal solid waste management: a case study of Sakarya. Journal of Cleaner Production 94:284–293. https://doi.org/10.1016/j.jclepro.2015.01.089
[29] Haupt M, Kägi T, Hellweg S (2018) Modular life cycle assessment of municipal solid waste management. Waste Management 79:815–827. https://doi.org/10.1016/j.wasman.2018.03.035
[30] Rana R, Ganguly R, Gupta AK (2019) Life-cycle assessment of municipal solid-waste management strategies in Tricity region of India. J Mater Cycles Waste Manag 21:606–623. https://doi.org/10.1007/s10163-018-00822-0

Sadia Zibouche is an engineer and holds a Master 2 in chemical engineering; she graduated from the Ecole Nationale Polytechnique, Algiers in 2015. Since 2017, she is a PhD student at the Ecole Nationale Polytechnique, Algiers. Her project focuses on the energetic valorization of household waste. She has published so far one article and participated in two international conferences and one national seminar.

Rabah Bouarab is Professor at the Chemical Engineering Department of Ecole Nationale Polytechnique, Algiers. He has an experience of 26 years in the dield of hydrogen production. He has authored or co-authored more than 40 papers mainly in this research area.

Mohammed Amouri was born in Chlef, Algeria in 1984. He received the Engineer Diploma degree from Ibn Khaldoun University, Tiaret, the Master and PhD degree from Ecole Nationale Polytechnique, Algiers, in 2012 and 2019 respectevly. He is currently a Researcher in Centre De Developpement Des Energies Renouvelables (CDER). His current research interests include the production of biodiesel, life cycle assessment and microalgae culture.